The implications of geometric frustration and orbital degeneracies on the evolution of magnetism in Na4Ir3O8 and α-NaMnO2

Author: Rebecca Lynn Dally

The implications of geometric frustration and orbital degeneracies on the evolution of magnetism in $Na_4Ir_3O_8$ and α-$NaMnO_2$

Rebecca Lynn Dally

A dissertation

submitted to the Faculty of

the department of Physics

in partial fulfillment

of the requirements for the degree of

Doctor of Philosophy

Boston College
Morrissey College of Arts and Sciences
Graduate School

July 2018

The implications of geometric frustration and orbital degeneracies on the evolution of magnetism in $Na_4Ir_3O_8$ and α-$NaMnO_2$

Rebecca Lynn Dally

Advisor: Stephen D. Wilson, PhD

Spin-orbit intertwined order gives rise to many novel phenomena with a broad phase space spanned by the competing energy scales within a system. This dissertation synthesized and studied two such systems demonstrating different manifestations of spin-orbit interactions, originating from orbital degeneracy effects, on geometrically frustrated magnetic lattices. Firstly, strong spin-orbit coupling in the hyperkagome lattice, $Na_4Ir_3O_8$, and secondly, the layered material, α-$NaMnO_2$, where single-ion anisotropy and a cooperative Jahn-Teller distortion drive magnetism to the quasi-1D limit.

The magnetic ground state of the $J_{eff} = 1/2$ spin-liquid candidate, $Na_4Ir_3O_8$, is explored via combined bulk magnetization, muon spin relaxation, and neutron scattering measurements. A short-range, frozen, state comprised of quasi-static moments develops below a characteristic temperature of T_F=6 K, revealing an inhomogeneous distribution of spins occupying the entirety of the sample volume. Quasi-static, short-range, spin correlations persist until at least 20 mK and differ substantially from the nominally dynamic response of a quantum spin liquid.

Much of this dissertation focuses on the second spin-orbit intertwined system, α-$NaMnO_2$, where a cooperative Jahn-Teller distortion of the MnO_6 octahedra arising from an orbital degeneracy in the Mn^{3+} cations directly affects the electronic (ferro-orbital) and magnetic (antiferromagnetic) order, which results in an intriguing study of low-dimensional magnetism. Intricacies of the structure, static magnetic order, and magnon dynamics are presented, which heavily relied on neutron scattering techniques. In particular, a longitudinally polarized bound magnon mode is characterized through the use of polarized neutron scattering.

Acknowledgments

Starting at the beginning, I'd like to thank the BC physics department for taking a chance and accepting me into the graduate program. I've always felt at home with the department largely due to the amazing staff and their support of the graduate students. I'd also like to thank the professors who not only showed dedication to their research, but also to teaching their courses and helping us see our fundamentals as more than just problem sets. I am deeply indebted to my fellow graduate students who were stuck in the first-year office with me way back in 2012. Everyone contributed to a helpful, and never competitive, atmosphere. The Quals study month was an enjoyable time, which I don't think most people can earnestly say, and I am doubtful that I would have passed if it weren't for our group study effort and countless moments of laughter.

I had almost no clue what I was doing when I first joined the Wilson lab, and often times, still don't. So I must thank my fellow lab mates for always taking the time to be a teacher when needed. My fellow old-timers in the lab, Tom Hogan, Ryan Need, Xiang Chen and Julian Schmehr, were especially wonderful collaborators and companions throughout the years. It has been a pleasure to see the group grow and diversify in research upon moving to UCSB, where I was welcomed with open arms. Thank you to the UCSB Materials Department for being a model of collaborative research.

I must also acknowledge all the support I've received from the beamline instrument scientists and staff at Argonne National Laboratory, Oak Ridge National Laboratory, Cornell High Energy Synchrotron Source, and especially the NIST Center for Neutron Research and Jeff Lynn for taking an interest in helping me succeed. I enjoyed the many hours I spent at the NCNR beamlines and admired the working atmosphere I observed, and so I very much look forward to getting to continue my research and education there full-time.

Apart from my professional life, I am lucky to be surrounded by a group of driven

and confident women who are always a source of motivation, inspiration, and support. I'm so proud to watch how your careers have grown, and I thank you for always rooting for mine. I have an enormously supportive family and a huge thank you must be given to my parents, who always allowed me to be curious and pursue the educational path that I saw fit. I'd like to especially thank my mom who, still, is always taking care of me.

Most importantly, I'd like to give my deepest thanks my adviser, Stephen. Thank you for teaching me how to be a good researcher, and being extremely patient along the way. You always make yourself available to your students and have so much dedication to seeing through to their success. I am so grateful to have been guided by such a brilliant and pleasant person.

This last year of my graduate work has been both my least and most productive. After a late-in-the-game diagnosis of Type I Diabetes, I've realized that living with this disease in 2018 is *relatively* easy thanks to the scientists and medical professionals who are working to advance quality of life treatments and find a cure. These dedicated researchers have been an inspiration for me to find greater meaning and insight into my own work and are responsible for my timely graduation.

Table of Contents

List of Tables

List of Figures

Chapter 1

Introduction

The subjects of this dissertation, $Na_4Ir_3O_8$ and α-$NaMnO_2$, are distinct in their magnetic grounds states, which are manifestations of their respective electronic configurations and lattice topologies. The differences partially stem from how the d orbitals are populated, thus modifying the spin-orbit contributions. The electrons of Ir^{4+} cations in $Na_4Ir_3O_8$ are directly affected by spin-orbit coupling and arrange into a total angular momentum state of $J_{eff} = \frac{1}{2}$, whereas the electrons of Mn^{3+} cations have quenched orbital angular momentum and settle into an $S = 2$ ground state, where spin-orbit coupling effects arise from second-order interaction terms. The electron configurations are on their own, unremarkable, as they are common for transition metals in the presence of cubic crystal fields, namely, MO_6 octahedra (M=transition metal). It is this, coupled with the manner in which the magnetic cations decorate their crystal structures, which presents two unique studies of magnetism.

Geometrically frustrated Ir^{4+} moments, coupled with edge-sharing octahedra and a theorized $J_{eff} = \frac{1}{2}$ ground state, satisfy the requirements for a spin-orbit driven liquid ground state in $Na_4Ir_3O_8$. However, the true ground state is determined by the relative strengths of spin-orbit coupling and isotropic and anisotropic exchange interactions. The conditions for the spin-liquid ground state are fragile, and it was found through bulk-magnetization measurements on polycrystalline samples that $Na_4Ir_3O_8$ undergoes a magnetic transition at 6 K, with hysteresis resembling that of an ice-like state. To demonstrate the delicate balance Ir^{5+} impurities have on the system, the metastable state of fully Na occupied $Na_4Ir_3O_8$ was exploited to synthesize the Na deficient $Na_3Ir_3O_8$, where susceptibility measurements showed this to behave like a paramagnet. Powder neutron diffraction showed no signs of long-range magnetic order, so muon spin relaxation was used to probe the local magnetic behavior to gain a fuller understanding of the nature of irreversibility in $Na_4Ir_3O_8$. The experiments confirmed the transition at 6 K in $Na_4Ir_3O_8$, but the data reflected a system in which quasi-static order accompanied by slow fluctuations of the moment dominated, down to at least 20 mK. The behavior parallels the configurationally degenerate phases with fluctuating order observed in spin-ice and related phases, where short-range correlations continue to fluctuate as temperature approaches 0 K.

The α-$NaMnO_2$ unit cell consists of alternating layers of edge-sharing MnO_6 octa-

hedra and Na ions, which stack along the c-axis in the monoclinic cell ($C2/m$). These robust MnO_6 layers provide a solid framework, such that Na ions can be deintercalated and intercalated into the space between with little degradation to the lattice upon electrochemical cycling, and much of the research on this system has focused on its properties as a battery cathode. A Jahn-Teller distortion results in the formation of an anisotropic triangular motif in the ab-plane, where nearest neighbor Mn atoms, along the b-axis, are much closer than next-nearest neighbor Mn atoms. Single-crystal growth via the floating-zone method–developed during the course of this dissertation–paved the way for new studies on the chemical and magnetic structure. The magnetic order was probed via time-of-flight neutron scattering, triple-axis neutron diffraction, neutron powder diffraction and bulk magnetic susceptibility. The path to commensurate, collinear antiferromagnetic order, driven by the easy-axis single-ion anisotropy of the Mn^{3+} moments, was found to be more complex than previously reported with polycrystalline samples. Above the quasi long-range ordered ground state, a coexisting short-range incommensurate order with a temperature dependent wavevector is observed, resulting from the frustration inherent to the triangular lattice.

Inelastic neutron scattering experiments show that the overall dimensionality of the system is quasi-1D, with exchange coupling between nearest neighbor Mn atoms close to that extracted from an experiment done on a polycrystalline sample of the parent compound. Single crystals, however, revealed the system to be more novel, counter to earlier work. The expected degenerate transverse modes from linear spin wave theory fit well to a Heisenberg model, which includes strong nearest and weak next-nearest neighbor exchange (J_1 and J_2, respectively), along with a single-ion anisotropy term, D. The gap value is ≈ 6 meV, however, another gapped mode is observed at ≈ 11 meV. This coherent and long-lived excitation was determined via polarized neutron scattering to be magnetic in origin with fluctuations along the moment direction, indicative of an amplitude mode, which also demonstrates 1D behavior. Scenarios such as a multimagnon and a Haldane state were ruled out based on the large gap value of the amplitude mode. The phenomenon is best described as a classical analogue to the amplitude modes in quantum systems, where crossover from the 1D to 3D ordered state comes with the onset of a static, staggered mean-field, which induces a symmetry breaking mechanism that stabi-

lizes coherent, and long-lived, excitations of the moments' magnitude. The α-$NaMnO_2$ lattice provides a route for an amplitude mode that hasn't been seen in a nominally classical antiferromagnet, suggesting that other systems with similar frameworks should be probed for amplitude modes.

The organization of this dissertation is as follows: the additional sections of this chapter compares and contrasts the electron configuration and manifestations of spin-orbit coupling between the magnetic cations in $Na_4Ir_3O_8$ and α-$NaMnO_2$. A discussion of how these intrinsic properties effects the magnetic exchange interactions follows. Ch. 2 reviews the basic neutron diffraction and scattering techniques used in this dissertation by covering the important cross-section equations, instrumentation and analysis techniques. Ch. 3 begins the presentation of data with the synthesis procedure and characterization for polycrystalline $Na_4Ir_3O_8$, and the sodium deficient variant, $Na_3Ir_3O_8$. The observation of a superstructure found in single-crystals of $Na_4Ir_3O_8$, grown by collaborators, is also presented. The results of the study on $Na_4Ir_3O_8$ concludes with Ch. 4, where μSR experiments probing the magnetic ground state are examined. Ch. 5 begins by detailing the floating-zone synthesis of α-$NaMnO_2$ and the subsequent structural characterization. Bulk and local probe studies on the magnetic ground state are presented in Ch. 6, and analysis of the neutron scattering experiments probing magnetic fluctuations are contained within Ch. 7.

1.1 Electron configurations of $Na_4Ir_3O_8$ and α-$NaMnO_2$

The electron configurations for $Na_4Ir_3O_8$ and α-$NaMnO_2$ are shown in Fig. 1.1. Fig. 1.1 (a) shows that the free Ir^{4+} and Mn^{3+} cations have their valence electrons residing in the 5-fold degenerate d orbitals (shown in Fig. 1.2 (a)). The d orbital wavefunctions are all eigenfunctions of the free-cation Hamiltonian, which means linear combinations are as well. One can find combinations such that the average orbital angular momentum, $\langle \mathbf{L} \rangle$, need not be zero. Some of the d orbitals are geometrically related by rotations. For example, the d_{xz}, d_{yz}, and d_{xy} orbitals can all be rotated into one another by 90° about some axis. The ability to move an electron from one orbital to another without costing energy means the electron will have $\langle \mathbf{L} \rangle \neq 0$. Due to the unquenched orbital angular

momentum, both the Ir^{4+} and Mn^{3+} free-cations have spin-orbit coupling contributions to the Hamiltonian. However, the contribution from Ir^{4+} will be much stronger than for Mn^{3+}, due to the larger nuclear Z (discussed further in Section 1.2).

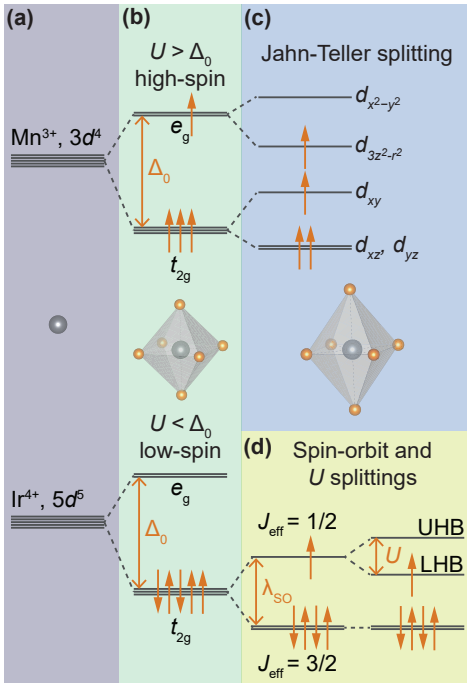

Figure 1.1: An overview of the driving energies which lead to the electron configurations for $Na_4Ir_3O_8$ and α-$NaMnO_2$. Panel (a) shows the 5 degenerate d-orbitals common to both Mn^{3+} and Ir^{4+}. Panel (b) shows that both systems, when in an octahedral crystal field undergo the same splitting, but resulting in different spin-states. The degeneracy of the electron in the e_g state for Mn^{3+} leads to a Jahn-Teller distortion shown in panel (c). An unquenched orbital angular momentum resulting in a large spin-orbit for Ir^{4+} leads to splitting of the t_{2g} orbitals and an additional energy coming from the Coulomb repulsion, U, reveals the insulating ground state in panel (d).

The situation between the two cations begins to change when the cation is placed in an octahedral environment of O^{2-} anions, where the outer shell electrons reside in the p orbitals, shown in Fig. 1.2 (b). The lobes of the p_z orbitals of the apical O^{2-} anions are pointed directly towards the lobes of the $d_{3z^2-r^2}$ orbital coming from the cation. Similarly, the p_x and p_y lobes point directly towards the lobes of the $d_{x^2-y^2}$ orbital. The remaining three d orbitals are rotated such that their lobes do not lie directly along an axis on which the p orbital lobes lie. This results in the energy splitting of the d orbitals shown in panel (b) of Fig. 1.1. Thus, it is from the distribution of electrostatic charges coming from the O^{2-} anions, and subsequent energy cost of electron density overlap, that cause the crystal-field splitting, Δ_0. Δ_0 is much larger for Ir^{4+} than for Mn^{3+}, because of the extended reach of $5d$ orbitals, which results in greater overlap with the

p orbitals. The d orbital wavefunctions, ψ^{m_l} ($l = 2$ is the orbital angular momentum for the d orbitals, which have the quantum number, $m_l = 0, \pm 1, \pm 2$), are no longer eigenfunctions of the Hamiltonian, which now includes the crystal-field potentials. They are now,

$$t_{2g}\begin{cases} d_{xy} & = \frac{1}{\sqrt{2}}\left(\psi^2 - \psi^{-2}\right) \propto -\frac{i}{\sqrt{2}}\left(\left|Y_2^2\right\rangle - \left|Y_2^{-2}\right\rangle\right) \\ d_{yz} & = \frac{1}{\sqrt{2}}\left(\psi^1 - \psi^{-1}\right) \propto \frac{i}{\sqrt{2}}\left(\left|Y_2^1\right\rangle + \left|Y_2^{-1}\right\rangle\right) \\ d_{xz} & = \frac{1}{\sqrt{2}}\left(\psi^1 + \psi^{-1}\right) \propto -\frac{1}{\sqrt{2}}\left(\left|Y_2^1\right\rangle - \left|Y_2^{-1}\right\rangle\right) \end{cases} \tag{1.1}$$

$$e_g\begin{cases} d_{x^2-y^2} & = \frac{1}{\sqrt{2}}\left(\psi^2 + \psi^{-2}\right) \propto \frac{1}{\sqrt{2}}\left(\left|Y_2^2\right\rangle + \left|Y_2^{-2}\right\rangle\right) \\ d_{3z^2-r^2} & = \psi^0 \propto \left|Y_2^0\right\rangle, \end{cases} \tag{1.2}$$

where and $Y_l^{m_l}$ are the spherical harmonics. The proportionality to the spherical harmonics, $Y_l^{m_l}$ comes from the fact that the radial functions have been left out (as they are the same for all the d wavefunctions within an energy level, n). Hund's rules specify that the electron configuration should maximize the total spin, S, unless that comes at too great of an energy cost. There is a balance between electron-electron repulsion from the p and d overlap versus the electron-electron repulsion of having two spins (of opposite spin, as to not violate the Pauli principle) in the same orbital on the same site, labeled U in Fig. 1.1 (b). For Mn^{3+}, it costs less energy to place an electron in the e_g state than to place it with another electron in one of the t_{2g} states because $\Delta_0 < U$. This results in the high-spin state, where $S = 2$; the opposite case holds for Ir^{4+}, where the low-spin state results in $S = 1/2$.

Determining if and how additional d orbital splitting occurs means being careful of the order in which energy scales present in the system are treated. For example, in the Ir^{4+} case, there is both spin-orbit coupling, λ_{SO}, and an on-site Coulomb repulsion, U, that still need to be taken into account. Because $\lambda_{SO} \sim U$ here, we must treat it first in order to get the correct electron configuration. Before discussing the additional splittings in $Na_4Ir_3O_8$, we will address the situation of α-$NaMnO_2$ in detail. The lone electron in the 2-fold degenerate e_g level leads to a splitting of the e_g level known as the

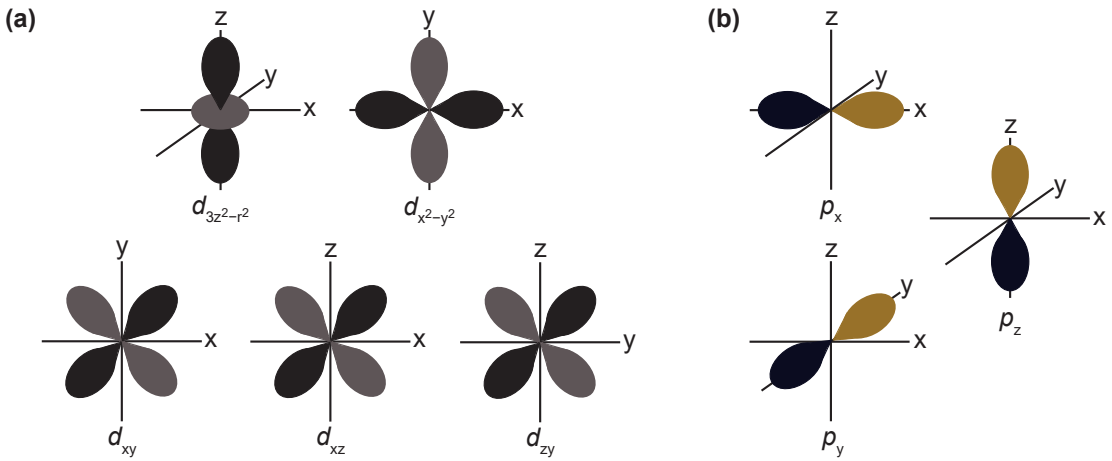

Figure 1.2: Panel (a) shows the d orbitals, where the outer shell electrons reside in Ir^{4+} and Mn^{3+} cations, while (b) shows the p orbitals, where the outer shell electrons reside in O^{2-} anions.

Jahn-Teller distortion, the result which is shown in Fig. 1.1 (c). The overall energy of the system can be lowered by deforming the octahedra with an elongation along the apical oxygens. The total change in energy for an orbital due to a Jahn-Teller distortion, ΔE_{JT}, is equal to $\pm A\epsilon + B\epsilon^2$, where ϵ is associated with the structural move away from thermal equilibrium, the first term is the change in energy caused by changing the amount of p-d overlap for the particular orbital, and the second term is the elastic gain in energy from the structural change (A and B are constants dependent on the orbital in question). The Mn^{3+} cations in α-$NaMnO_2$ are said to be Jahn-Teller active, and the density of these Jahn-Teller active cations leads to a collective distortion of all the MnO_6 octahedra in the crystal, called the cooperative Jahn-Teller effect. This also happens to lead to long-range ferro-orbital ordering of the $d_{3z^2-r^2}$ orbitals. The elongation of the octahedra leads to less overlap between the d orbitals with a z-component and the p_z orbitals of the O^{2-} anions, which leads to a lowering of energy for the d_{xz}, d_{yz}, and $d_{3z^2-r^2}$ orbitals, further reducing the degeneracy. The other consequence of the Jahn-Teller distortion is that the density of states (DOS) for the occupied spin-up t_{2g}-orbitals gets lowered and the occupied spin-up e_g orbital ($d_{3z^2-r^2}$) now sits below the Fermi energy. All the unoccupied spin-down d-orbitals plus the unoccupied spin-up $d_{x^2-y^2}$ orbital are above the Fermi energy due to the on-site Coulomb repulsion. The nature of the insulating phase is in question depending on which model is used to calculate the gap. In GGA calculations, reports agree on a semiconducting picture with a gap

of $\approx 1.3 - 1.4$ eV [1, 2, 3]. Refs. [2, 3] also used GGA+U calculations stating that the electron-electron correlations should be included in the model. In this picture, the DOS of the occupied spin-up d orbitals is pushed below p-orbitals, which are now closest to the Fermi energy. Now, the gap is defined mostly by p-d excitations leading to the conclusion that α-$NaMnO_2$ is a charge transfer insulator with a band gap of ≈ 3 eV.

With no Jahn-Teller distortion, the electron configuration after the crystal field splitting for the Ir^{4+} cations in $Na_4Ir_3O_8$ still has 3-fold degeneracy in the t_{2g} orbitals, and the orbital angular momentum is only partially quenched. The e_g energy levels are far separated from the t_{2g} levels, and electron configuration becomes analogous to a single-particle (the one hole) in a three-fold degenerate level, like the degenerate p_x, p_y, and p_z orbitals, which have an orbital angular momentum $l = 1$. Thus, we can say, the effective orbital angular momentum of the Ir^{4+} cation is $l_{eff} = 1$. With $l_{eff} = 1$ and $S = 1/2$, we can determine the total angular momentum, J, (and it's quantum number, $m_j = -J, -J+1, ..., J-1, J$) via Hund's third rule, which says the spin-orbit coupled states are then $J_{eff} = |L - S| = 1/2$ or $J_{eff} = |L - S| = 3/2$. Following Hund's third rule, the lower energy state will be $J_{eff} = |L - S| = 3/2$. This can be seen in Fig. 1.1 (d), and it becomes clear spin-orbit coupling will play a role in the physics of $Na_4Ir_3O_8$. There is also another splitting in Fig. 1.1 (d), which is small, but comes from the on-site Coulomb repulsion that prevents electron hopping between Ir atoms. This is important because without this electron-electron correlation consideration, simple band theory would say that $Na_4Ir_3O_8$ should be a metal; however, it has experimentally been shown to have increasing resistance down to low temperatures, which is consistent with the system being a Mott insulator, where the charge gap is of the d-d type and the DOS of the p-orbitals is at a lower energy than the DOS of the d-orbitals.

1.2 The spin-orbit contributions

Spin-orbit coupling manifests its effects in different ways between $Na_4Ir_3O_8$ and α-$NaMnO_2$, but plays a crucial role in explaining the magnetic properties of the two systems. The underlying cause of the differences is due to the contrast in orbital degeneracies between the two systems. In $Na_4Ir_3O_8$, orbital angular momentum is only

partially quenched, leading to spin-orbit coupling which contributes to the first order perturbation correction to the Hamiltonian. α-$NaMnO_2$ has quenched angular momentum due to the degeneracy lifting Jahn-Teller distortion, leading to spin-orbit contributions coming from the interaction between the mixing of occupied and unoccupied d orbitals, made possible by the surrounding crystal-field. Mathematically, this is represented by the second-order perturbation correction to the Hamiltonian of the spin-orbit coupling term. This phenomenon is a type of magnetocrystalline anisotropy known as single-ion anisotropy. The similarities and differences in the the electron configurations and spin-orbit coupling terms for each system directly contribute to the resulting spin Hamiltonian governing the magnetic ground states.

We will now expand on the implications that the electron configurations have on the spin-orbit coupling terms in the Hamiltonian. Much of this section was written following the discussions on spin-orbit coupling in Ref. [4]. The spin-orbit Hamiltonian is written as,

$$\hat{H}_{\mathrm{S-O}} = \lambda(R)\hat{\mathbf{L}} \cdot \hat{\mathbf{S}}, \tag{1.3}$$

where $\lambda(R)$ is a function only dependent on the radial part of the orbital wavefunctions, $\lambda(R) = \frac{e^2}{2m_e^2c^2}\frac{1}{R^3}$. $\hat{\mathbf{L}}$ and $\hat{\mathbf{S}}$ are the orbital and spin angular momentum operators, respectively. Eq. 1.3 is derived from the nonrelativistic limit of the Dirac equation with a Coulomb potential energy. Treating Eq. 1.3 as a perturbation, the first-order shift in energy due to spin-orbit coupling is,

$$\begin{aligned} E^{(1)}_{\mathrm{S-O}} &= \langle n, l, m_l, s, m_s | \, \lambda(R)\hat{\mathbf{L}} \cdot \hat{\mathbf{S}} \, | n, l, m_l, s, m_s \rangle \\ &= \lambda(R) \, \langle l, m_l, s, m_s | \, \hat{\mathbf{L}} \cdot \hat{\mathbf{S}} \, | l, m_l, s, m_s \rangle \\ &= \lambda(R) \, \langle l, s, J, m_j | \, \hat{\mathbf{L}} \cdot \hat{\mathbf{S}} \, | l, s, J, m_j \rangle \, , \end{aligned} \tag{1.4}$$

where from the first to the second line in Eq. 1.4, the radial part of wavefunction has been separated from the angular and spin part. The matrix elements can be calculated either in the $|l, m_l, s, m_s\rangle$ basis or the $|l, s, J, m_j\rangle$ basis (where going from one basis to

another can be achieved via calculations of the Clebsch-Gordan coefficients). Either way, the first-order perturbation calculates the average value of the observable, $\hat{\mathbf{L}} \cdot \hat{\mathbf{S}}$, with respect to the ground state, $|\varphi_0\rangle$. In the $|l, s, J, m_j\rangle$ basis, $\hat{\mathbf{L}}$ and $\hat{\mathbf{S}}$ commute, and we can rewrite Eq. 1.4 as,

$$E^{(1)}_{\mathrm{S-O}} = \lambda(R)\hat{\mathbf{S}} \cdot \langle\varphi_0| \hat{\mathbf{L}} |\varphi_0\rangle \,, \tag{1.5}$$

and we can see why a quenched orbital angular momentum state will yield zero for the first-order correction to the spin-orbit coupling energy shift. The result, given an unquenched state, such as in $Na_4Ir_3O_8$, is,

$$E^{(1)}_{\mathrm{S-O}} = \frac{m_e c^2 Z^4 \alpha^4}{4n^3 l(l+\frac{1}{2})(l+1)}. \tag{1.6}$$

The dependence on Z^4 in eqn. 1.6 makes clear why higher Z elements have a larger spin-orbit contribution, as alluded to at the beginning of the chapter for the Ir^{4+} versus Mn^{3+} free cations. An important consequence of spin orbit coupling to the analysis of data is that it changes the g-factor from that of a free-electron (spin-only) where $g = 2$.

At first glance, the degeneracy between the d_{xz} and the d_{yz} orbitals in α-$NaMnO_2$ may seem to meet the requirement for $\langle\mathbf{L}\rangle \neq 0$. However, one cannot simply rotate the spin-up electron from the d_{xz} (d_{yz}) to the d_{yz} (d_{xz}) orbital because there is already a spin-up electron occupying the orbital, and as mentioned, the spin-down d orbitals are above the Fermi energy. This is a case of quenched orbital angular momentum. It appears that spin-orbit coupling would not play a role in the Hamiltonian at this point, however, we will see that spin component, S, is coupled to the lattice (i.e. the crystal-field) via an interaction through the d orbitals. This interaction leads to magnetocrystalline anisotropy, and specifically for α-$NaMnO_2$, single-ion uniaxial anisotropy. The next-highest order correction to the energy for the spin-orbit Hamiltonian is given by second-order perturbation theory, where,

$$E^{(2)}_{\mathrm{S-O}} = -\sum_{k\neq 0} \frac{\left|\langle\varphi^0_0|\,\hat{H}_{\mathrm{S-O}}\,|\varphi^0_k\rangle\right|^2}{E^0_k - E^0_0}, \tag{1.7}$$

and φ_k is an unoccupied, excited, state in the ground state configuration. Here, we are mixing the occupied and unoccupied components of orbital angular momentum, which allows for the creation of non-zero orbital angular momentum states. Eq. 1.7 can be rewritten by expanding the square and $\hat{H}_{\mathrm{S-O}}$,

$$E^{(2)}_{\mathrm{S-O}} = -\,|\lambda|^2 \sum_{k\neq 0} \frac{\hat{S}_\mu \langle\varphi^0_0|\,\hat{L}_\mu\,|\varphi^0_k\rangle\,\hat{S}_\nu \langle\varphi^0_k|\,\hat{L}_\nu\,|\varphi^0_0\rangle}{E^0_k - E^0_0} \tag{1.8}$$

where μ and ν run over the Cartesian coordinates x, y, and z. An intuitive way to think about the origin of the uniaxial single-ion anisotropy in the MnO_6 octahedra of α-$NaMnO_2$ is to follow the argument in Ref. [5] by writing Eq. 1.7 in terms of spherical coordinates, such that,

$$\begin{aligned}\hat{H}_{\mathrm{S-O}} = {} & \lambda\hat{S}_{z'}\left(\hat{L}_z\cos\theta + \frac{1}{2}\hat{L}_+e^{-i\phi}\sin\theta + \frac{1}{2}\hat{L}_-e^{i\phi}\sin\theta\right) \\ & + \frac{\lambda}{2}\hat{S}_{+'}\left(-\hat{L}_z\sin\theta - \hat{L}_+e^{-i\phi}\sin^2\frac{\theta}{2} + \hat{L}_-e^{i\phi}\cos^2\frac{\theta}{2}\right) \\ & + \frac{\lambda}{2}\hat{S}_{-'}\left(-\hat{L}_z\sin\theta + \hat{L}_+e^{-i\phi}\cos^2\frac{\theta}{2} - \hat{L}_-e^{i\phi}\sin^2\frac{\theta}{2}\right),\end{aligned} \tag{1.9}$$

where the primed and unprimed labels denote that $\hat{S}$ and $\hat{L}$ have different coordinate axes. We can choose z to be along the $d_{3z^2-r^2}$ orbital (along the elongated Jahn-Teller distortion direction), z' to be local spins' preferred rotational axis, and ϕ and θ are the polar and azimuthal angles with respect to the (x, y, z) coordinate system, describing this direction. The first term in Eq. 1.9 is called the spin-conserving term because it mixes between unoccupied and occupied orbitals with the same spin direction. The second two terms are the spin non-conserving terms and will be significantly weaker. To see why, we can look at the denominator in Eq. 1.7: the smaller the energy difference between the occupied and unoccupied states, the larger the energy lowering will be. The spin-down states are far in energy from the spin-up states, and will contribute little to the term.

Focusing just on the spin-conserving term, and the spin-up states, we can look for the mixing of states with the smallest energy difference. This would be between the $d_{x^2-y^2} \uparrow$ and the $d_{3z^2-r^2} \uparrow$ orbitals. However, $\Delta m = 2$ which is not an allowed transition (via selection rules for the problem at hand). The next smallest energy difference is between $d_{x^2-y^2} \uparrow$ and $d_{xy} \uparrow$, where $\Delta m = 0$. This term will maximize the energy lowering when $\theta = 0$ in Eq. 1.9, which corresponds to the moment lying along z, which is along the $d_{3z^2-r^2}$ orbital (ϕ is invariant when $\theta = 0$). We can also see why there is no single-ion anisotropy term for $Na_4Ir_3O_8$, and in fact, there is no single-ion anisotropy for $S = 1/2$ systems (although debated). The ground state electron configuration is a Kramer's doublet, where the occupied and unoccupied states have no difference in energy. As we will see in Section 1.3, spin-orbit coupling will still contribute to a preferred orientation axis in other mechanisms besides single-ion anisotropy.

The single-ion anisotropy for each cation, i, in the system is included in the spin Hamiltonian as the term,

$$H^{\mathrm{SIA}} = A_i \left(\hat{S}_i^z\right)^2 = E_i \left(\| \, z\right) - E_i \left(\perp z\right), \tag{1.10}$$

where $E_i \left(\| \, z\right) - E_i \left(\perp z\right)$ is the energy difference between having the spin oriented along cation i's local z-axis versus perpendicular to it. $A_i < 0$ corresponds to easy-axis (uniaxial) anisotropy and $A_i > 0$ corresponds to easy-plane anisotropy. In the absence of easy-plane anisotropy, as is the case for α-$NaMnO_2$, Eq. 1.10 is typically written as $D\left(\hat{S}_i^z\right)^2$ (where this D should not be confused with the Dzyaloshinskii-Moriya interaction $\mathbf{D}$ discussed shortly).

1.3 Magnetic exchange and frustration

The total wave function for two electrons whose orbitals overlap must be antisymmetric, per the Pauli exclusion principle. The spatial and spin parts of the Hamiltonian can be separated such that $\Psi = \psi(\mathbf{r}_1, \mathbf{r}_2)\rho(\mathbf{S}_1, \mathbf{S}_2)$, meaning the spatial part of the wave function is asymmetric and the spin part is symmetric or vice versa. If $\psi(\mathbf{r}_1, \mathbf{r}_2) = \psi(\mathbf{r}_2, \mathbf{r}_1)$, then the spin part must be a singlet, because the $S = 0$ state is the only antisymmetric

option where $\rho(\mathbf{S}_1, \mathbf{S}_2) = -\rho(\mathbf{S}_2, \mathbf{S}_1)$. This means that the two electrons have antiparallel spins and have an antiferromagnetic exchange interaction. The symmetric triplet states, $S = 1$, are higher in energy with the underlying mechanism being Coulomb repulsion between the electrons from the two ions. The spin Hamiltonian for this system is,

$$H^{\text{spin}} = -\left(E_s - E_t\right)\mathbf{S}_1 \cdot \mathbf{S}_2 = -J\mathbf{S}_1 \cdot \mathbf{S}_2, \tag{1.11}$$

where J is a measure of the energy difference between the singlet state, E_s and the triplet state E_t. When $E_s < E_t$, antiparallel alignment of the spins is favored. The spatial part of the wavefunction is always symmetric for the two-electron problem (i.e. the H_2 molecule problem), but this is not always the case for electrons in a crystal lattice. However, this type of exchange, known as direct exchange, is usually not responsible for the long-range magnetic order in a crystal because it is often weak. Superexchange, where orbital overlap between two magnetic ions is mediated through a nonmagnetic ion is often much stronger. A set of rules, known as the Goodenough-Kanamori-Anderson (GKA) rules can be a good predictor of whether antiferromagnetic or ferromagnetic interactions will dominate [6] for certain 180° or 90° cation-anion-cation bonds. Both direct and superexchange can be modeled by Eq. 1.11, despite the different origins.

Due to significant overlap of the half-filled t_{2g} d_{xy} orbitals of Mn^{3+} nearest neighbors in α-$NaMnO_2$, antiferromagnetic direct exchange is actually the leading J term. The superexchange pathways for nearest neighbors and next-nearest neighbors is through 90° $Mn^{3+}-O^{2-}-Mn^{3+}$ bonds, which are known to be weak [7]. However, the next nearest neighbor superexchange pathways are what contributes to magnetic frustration, because two nearest neighbors share the same next-nearest neighbors with equal exchange interaction strength. Theoretically, this leads to an impasse when it comes to finding a unique magnetic ground state, because more than one degenerate ground state is possible. As discussed in Ch. 6, α-$NaMnO_2$ does find a ground state with ordering wavevector $\mathbf{k} = (1/2, 1/2, 0)$, but evidence of frustrastion persists well within the ordered state.

The exchange interactions in $Na_4Ir_3O_8$ are a bit more complicated than in α-$NaMnO_2$.

Like in α-$NaMnO_2$, the transition metal octahedra are edge sharing, and the superexchange pathways will have 90° geometry. However, Ref. [8] found predominately superexchange interactions to control the spin Hamiltonian as opposed to a direct exchange term. Only one of the superexchange interactions stems from an isotropic symmetry, which is a J term just discussed, and the others are from the anisotropic symmetry: the antisymmetric Dzyaloshinskii-Moriya (DM) interaction, D, and the symmetric exchange, Γ. Both D and Γ are obtained by extending the theory of superexchange to spin-orbit coupling [9, 10] and are on the order of $(\Delta g/g)\, J$ and $(\Delta g/g)^2\, J$, respectively, and Δg is the deviation from the free-electron g-factor. Two spins, each with spin-orbit coupling, can indirectly interact with one another through an intermediate nonmagnetic ion, and influence each others' spin orientations. The DM interaction for two spins, $\mathbf{S}_1$ and $\mathbf{S}_2$ is,

$$H^{\mathrm{DM}} = \mathbf{D}_{12} \cdot \mathbf{S}_1 \times \mathbf{S}_2. \tag{1.12}$$

Many times, there is no DM interaction in a system because the crystal symmetry forbids it. If the point bisecting the two magnetic ions, $\mathbf{S}_1$ and $\mathbf{S}_2$, is a center of inversion, then $\mathbf{D} = 0$. $Na_4Ir_3O_8$ has a non-centrosymmetric space group and meets this requirement for an allowed DM exchange interaction. The other requirement, which we can directly from Eq. 1.12, is that $\mathbf{S}_1$ and $\mathbf{S}_2$ cannot be parallel. The symmetric exchange, Γ, arises from the pseudodipolar interaction which originates from the coupling between the spin-orbit coupling and the crystal field [11]. This is similar to the mechanism behind single-ion anisotropy, except instead of the on-site mixing between spin-orbit effects and crystal field, the mixing is between the spin-orbit coupling of two spins and the surrounding crystal field.

Other studies also stress the importance of including a Kitaev-like term, K [12, 13]. The Kitaev model is for a honeycomb lattice with $S = 1/2$ bond dependent antiferromagnetic interactions, and so the extension of this model to the hyperkagome lattice is considered Kitaev-like. Theoretical studies have found a host of ground states for $Na_4Ir_3O_8$ depending on which exchange terms are included in the spin Hamiltonian,

and the relative strengths of the various interactions. Due to all Ir-Ir bonds being equal, the interactions introduce frustration into the system, with many ground states being highly degenerate, including the most degenerate, quantum spin liquid (QSL) state. Chs. 3 and 4 detail the findings of this dissertation on the magnetic ground state of $Na_4Ir_3O_8$.

References

[1] Velikokhatnyi, O., Chang, C.-C. & Kumta, P. Phase stability and electronic structure of $NaMnO_2$. *Journal of the Electrochemical Society* **150**, A1262–A1266 (2003).

[2] Zhang, G. R., Zou, L. J., Zeng, Z. & Lin, H. Q. Magnetic and electronic properties of α-$NaMnO_2$. *Journal of Applied Physics* **105**, 07E512 (2009).

[3] Jia, T. *et al.* Magnetic frustration in α-$NaMnO_2$ and $CuMnO_2$. *Journal of Applied Physics* **109**, 07E102 (2011).

[4] Cohen-Tannoudji, C., Diu, B. & Laloë, F. *Quantum Mechanics, Volume 2* (Wiley, New York, 1977).

[5] Albright, T. A., Burdett, J. K. & Whangbo, M.-H. *Orbital Interactions in Chemistry* (Wiley, Chicester, 2013), 2nd ed. edn.

[6] Goodenough, J. B. *Magnetism and the chemical bond.* Interscience monographs on chemistry. Inorganic chemistry section;v. 1 (Interscience Publishers, New York, 1963).

[7] Mostovoy, M. V. & Khomskii, D. I. Orbital Ordering in Frustrated Jahn-Teller Systems with 90° Exchange. *Phys. Rev. Lett.* **89**, 227203 (2002).

[8] Norman, M. R. & Micklitz, T. Electronic structure of hyper-kagome $Na_4Ir_3O_8$. *Phys. Rev. B* **81**, 024428 (2010).

[9] Moriya, T. Anisotropic Superexchange Interaction and Weak Ferromagnetism. *Phys. Rev.* **120**, 91–98 (1960).

[10] Dzyaloshinsky, I. A thermodynamic theory of "weak" ferromagnetism of antiferromagnetics. *Journal of Physics and Chemistry of Solids* **4**, 241 – 255 (1958).

[11] van Vleck, J. H. On the Anisotropy of Cubic Ferromagnetic Crystals. *Phys. Rev.* **52**, 1178–1198 (1937).

[12] Mizoguchi, T., Hwang, K., Lee, E. K.-H. & Kim, Y. B. Generic model for the hyperkagome iridate $Na_4Ir_3O_8$ in the local-moment regime. *Phys. Rev. B* **94**, 064416 (2016).

[13] Gupta, S. N. *et al.* Spin liquid like Raman signatures in the hyperkagome iridate $Na_4Ir_3O_8$. *Phys. Rev. B* **94**, 155153 (2016).

Chapter 2

Neutron Techniques

Neutrons played an integral role in understanding the properties of $Na_4Ir_3O_8$ and α-$NaMnO_2$. Multiple techniques were utilized to study the crystal and magnetic structures, as well as the magnon dynamics and interactions. The neutron has zero net charge and the scattering process from atoms is free of any Coulomb barrier, as opposed to x-ray or electron diffraction techniques. The lack of dependence on an atom's Z (number of electrons) means that the scattering length, b, from different elements can be drastically varied even between periodic table neighbors, making neutrons ideal for applications such as detecting light elements or determining site occupancies when more than one element can sit at a particular Wyckoff position. The neutron also has a magnetic moment, which can interact with unpaired electron spins in a sample and is the one of the main reasons neutrons are used for observing magnetic phenomena [1]. This chapter covers the pertinent formulas, techniques, and analyses needed to understand the data collected throughout the course of this dissertation. In addition to this chapter, Section B.1 gives a detailed explanation on the expression of fault defects in the scattered intensity from neutron data for α-$NaMnO_2$.

2.1 Neutron cross sections

One measures the double differential cross-section in a neutron scattering experiment. It is the number of neutrons scattered over a solid angle, Ω_f (picked by the detector position), from an initial momentum, $\mathbf{k}_i$, with a final energy between E_f and $E_f + dE_f$. This cross section is proportional to the scattering function, $S(\mathbf{Q}, \hbar\omega)$, which contains all the desired information about the sample under study. The independent variables, $\mathbf{Q} = \mathbf{k}_f - \mathbf{k}_i$ and $\hbar\omega = E_i - E_f$, are the scattering vector and energy transfer, respectively. The scattering function is derived by treating the neutron as a weak perturbation to the system due to the neutron-system interaction potentials. This means we can assume that the neutron will not change the states (eigenfunctions) of the system, but can cause transitions from an initial quantum state, λ_i, to a final quantum state, λ_f, and in this picture, Fermi's Golden Rule holds. $S(\mathbf{Q}, \hbar\omega)$ can be calculated for different interaction potentials, $V(\mathbf{r})$, between the neutron and the system. We will see that $V(\mathbf{r})$ can be the nuclear-neutron interaction and/or a magnetic interaction, but the general expression

is,

$$\left.\frac{d^2\sigma}{d\mathbf{\Omega}_f dE_f}\right|_{\mathbf{k}_i\to\mathbf{k}_f} = \frac{1}{N}\frac{k_f}{k_i}\left(\frac{m_n}{2\pi\hbar^2}\right)^2 \sum_{\lambda_i\sigma_i} p_{\lambda_i} p_{\sigma_i} \sum_{\lambda_f\sigma_f} \left|\langle \mathbf{k}_f\sigma_f\lambda_f| \, V(\mathbf{r}) \, |\mathbf{k}_i\sigma_i\lambda_i\rangle\right|^2 \delta\left(\hbar\omega + E_i - E_f\right), \tag{2.1}$$

where $\sum_{\lambda_i\sigma_i} p_{\lambda_i} p_{\sigma_i}$ is a weighting factor dependent on the probability of the system being in an initial state, λ_i, and the neutron being in an initial spin state, σ_i, m_n is the mass of the neutron, and N is the number of scattering centers. The incident and final states of the neutron are described by plane waves, where the solution to the scattered wave after encountering the potential involves a Green's function. The solution involves invoking the Born approximation, in which the scattered wave can be described by the initial, unperturbed state, $e^{i\mathbf{k}_i\cdot\mathbf{r}}$, plus a perturbed plane wave to the first order in V. In using this approximation, the equation becomes simplified because it describes only a single scattering process. Higher order terms, which represent multiple scattering processes, are not included. However, it should be noted that multiple scattering processes are common and are often obvious in inelastic neutron experiments. The benefit of the Born approximation is that the interaction matrix elements describing the transition from an incoming plane wave to the outgoing plane wave after encountering a potential can be independently evaluated from the system and spin state elements ($|\mathbf{k}_i\sigma_i\lambda_i\rangle \to |\mathbf{k}_i\rangle\,|\sigma_i\lambda_i\rangle$), and,

$$\langle \mathbf{k}_f| \, V \, |\mathbf{k}_i\rangle = V(\mathbf{Q}), \tag{2.2}$$

which is just the Fourier transform of $V(\mathbf{r})$. The next sections will cover the interaction potentials for nuclear and magnetic scattering.

2.1.1 The nuclear interaction

The total scattering cross section, $\sigma_{\text{scat}} = \int\int_{-\infty}^{E_0} \frac{d^2\sigma}{d\Omega_f dE_f} d\Omega_f dE_f$ (where E_0 is the maximum allowed neutron energy loss), is a sum of the coherent and incoherent cross sec-

tions, which contribute to the cooperative and non-cooperative phenomena in a material, respectively. In a collection of atoms/isotopes, where the lth atom/isotope has scattering length, b_l, the average coherent scattering length will be $\overline{b} = \sum_l c_l b_l$, where c_l is the frequency of occurrence. The coherent scattering only depends on the location of the elements within a system, and the average coherent cross section per atom is $\sigma_{coh} = 4\pi \left(\overline{b}\right)^2$. The random fluctuations in scattering length between sites leads to incoherent scattering, where the effective scattering length is $b_{\text{inc}} = \sqrt{\overline{b^2} - \overline{b}^2}$. We will only discuss elastic nuclear coherent scattering here, which measures the neutrons scattered cooperatively due to the physical positions of the atoms in a material. The potential for a neutron colliding with an atom at position $\mathbf{r}$ is a delta function, $V(\mathbf{r}) = \frac{2\pi\hbar^2}{m_n} b\, \delta(\mathbf{r})$. For a crystalline lattice, with atoms at sites, l, we can define the atomic density as $\rho(\mathbf{r}) = \frac{2\pi\hbar^2}{m_n} b \sum_l \delta(\mathbf{r} - \mathbf{r}_l)$. Transforming to reciprocal space, we have $\rho(\mathbf{Q}) = \frac{2\pi\hbar^2}{m_n} b \int \sum_l \delta(\mathbf{r} - \mathbf{r}_l) e^{i\mathbf{Q}\cdot\mathbf{r}} d\mathbf{r} = \frac{2\pi\hbar^2}{m_n} b \sum_l e^{i\mathbf{Q}\cdot\mathbf{r}_l}$, thus $V(\mathbf{Q})$ from Eq. 2.2 can be defined as $V(\mathbf{Q}) = \frac{2\pi\hbar^2}{m_n} b$. Ref. [2] showed that the scattering function could be written,

$$S(\mathbf{Q},\omega) = \frac{1}{2\pi\hbar N} \int_{-\infty}^{\infty} dt\; e^{-i\omega t} \left\langle \rho_{\mathbf{Q}}(0) \rho_{-\mathbf{Q}}(t) \right\rangle . \tag{2.3}$$

The scattering function in the form of Eq. 2.3 is the Fourier transform of the time-dependent pair-correlation function, $G(\mathbf{r}, t)$. The pair-correlation function describes the probability of finding an atomic density about position $\mathbf{r}$ at time t, given an atomic density about position $\mathbf{r} = 0$ at time $t = 0$, and is a measure of the density fluctuations within a system. In the absence of spatial correlations, the pair-correlation function would be zero, and there would be no coherent scattering. It is worth noting that in the incoherent scattering function, you are probing the Fourier transform of the self-correlation function, which is the time-averaged probability of finding the atomic density about position $\mathbf{r}$ at time t given the same atomic density about position $\mathbf{r} = 0$ at time $t = 0$.

By measuring with zero energy transfer, $E_i = E_f$, we can probe the Bragg scattering (phonons, which will not be discussed here, are also a type of nuclear coherent scattering, albeit, at finite energy transfers, and are the cooperative lattice excitations that result

from the neutron giving the system specific energies). This corresponds to a delta function at $\omega = 0$ in Eq. 2.3 as well as a delta function when $\mathbf{Q} = \mathbf{G}_{hkl}$, where $\mathbf{G}_{hkl} = h\mathbf{a}^* + k\mathbf{b}^* + l\mathbf{c}^*$, is the reciprocal lattice vector. The cross section for coherent elastic scattering is,

$$\left.\frac{d\sigma}{d\Omega}\right|_{coh}^{el} = N\frac{(2\pi)^3}{\upsilon_0}\left(\bar{b}\right)^2 e^{-2W}\sum_{\mathbf{G}_{hkl}}\delta\left(\mathbf{Q}-\mathbf{G}_{hkl}\right), \tag{2.4}$$

where $\bar{b}$ is the average coherent scattering length of the atom, υ_0 is the unit cell volume, and e^{-2W} is the Debye-Waller factor which is added to take into account small deviations of atoms from equilibrium. Eq. 2.4 is specific to a Bravais lattice, with one species of atom. For a crystal with more than a one-atom basis, the cross-section must sum over all atomic positions, $\mathbf{r}_l$, within a unit cell, and take into consideration the differences in $\bar{b}$ for different elements. The more general form of Eq. 2.4 is,

$$\left.\frac{d\sigma}{d\Omega}\right|_{coh}^{el} = N\frac{(2\pi)^3}{\upsilon_0}\sum_{\mathbf{G}_{hkl}}\delta\left(\mathbf{Q}-\mathbf{G}_{hkl}\right)\left|F_{\mathrm{N}}(\mathbf{G}_{hkl})\right|^2 \tag{2.5}$$

$$F_{\mathrm{N}}(\mathbf{G}_{hkl}) = \sum_l \bar{b}_l e^{i\mathbf{G}_{hkl}\cdot\mathbf{r}_l}e^{-W_l}, \tag{2.6}$$

where $F_{\mathrm{N}}(\mathbf{G}_{hkl})$ is called the static nuclear structure factor, and contains information about the the atoms within a unit cell. The intensity of a given Bragg peak is the square of $F_{\mathrm{N}}(\mathbf{G}_{hkl})$, multiplied by experiment- dependent factors. Rietveld refinement attempts to refine a calculated crystal model, which has intensities, F_{calc}, to fit experimental data intensities F_{obs} in order to find the atomic parameters.

2.1.2 The magnetic interaction

Halpern and Johnson first calculated the magnetic scattering cross-section [3] upon realizing that the neutron's moment should "*manifest itself*" when slow-scattering from paramagnetic materials. In fact, evidence of the neutron's moment is observed from scattering off of a wide variety of materials, not just paramagnetic, as shown by their calculation. The neutron has a spin, $\mathbf{s}$, with spin-state, $\boldsymbol{\sigma} = \frac{2\mathbf{s}}{\hbar}$, leading to a moment,

$\boldsymbol{\mu}_n = -\gamma\mu_N\boldsymbol{\sigma}$. The scattering formulas in the previous section ignored the spin of the neutron, but now they must be included. The neutron's moment will interact with the moments of unpaired electrons, $\boldsymbol{\mu_e} = -2\mu_B\mathbf{s}$, in a system via the potential,

$$\mathbf{V}(\mathbf{r}) = -\gamma\mu_N 2\mu_B\boldsymbol{\sigma}\cdot\left[\text{curl}\left(\frac{\mathbf{s}\times\hat{\mathbf{R}}}{R^2}\right) + \frac{1}{\hbar}\frac{\mathbf{p}\times\hat{\mathbf{R}}}{R^2}\right]. \tag{2.7}$$

The first term is the due to the dipole-dipole interaction between the two spins, and the second term is the interaction between the neutron spin and the electron's orbital motion coming from it's angular momentum, $\mathbf{p}\times\mathbf{R}$. As in the nuclear coherent scattering case, we use the Born approximation to find the $\langle\mathbf{k}_f|\,V\,|\mathbf{k}_i\rangle$ matrix elements. Ignoring the orbital contribution, which is usually small, the total coherent differential cross section due can be written,

$$\frac{d^2\sigma}{d\boldsymbol{\Omega}_f dE_f} = \frac{k_f}{k_i}\sum_{\lambda_i,\sigma_i} p_{\lambda_i}\sum_{\lambda_f,\sigma_f}\left|\langle\lambda_f|\sum_l e^{i\mathbf{Q}\cdot\mathbf{r}_l}U_l^{\sigma_i\sigma_f}\,|\lambda_i\rangle\right|^2\delta\left(\hbar\omega + E_i - E_f\right), \tag{2.8}$$

where,

$$U_l^{\sigma_i\sigma_f} = \langle\sigma_f|\,b_l - p_l\mathbf{M}_\perp\cdot\boldsymbol{\sigma}\,|\sigma_i\rangle\,, \tag{2.9}$$

and $U_l^{\sigma_i\sigma_f}$ is the atomic scattering amplitude, and $p = \frac{\gamma e^2}{2m_e c^2}gf(\mathbf{Q})$ (e is the electron charge, m_e is the electron mass, and c is the speed of light) is the magnetic amplitude. $f(\mathbf{Q})$ are ion specific form factors and are the Fourier transforms of the magnetization distribution of a magnetic atom. They have been analytically calculated and can be looked up in reference materials. The magnitude decreases approximately as Q^2, meaning the strongest magnetic scattering will be at low-Q. The term, $\mathbf{M}_\perp$, comes from the magnetic interaction matrix elements when evaluating $V(\mathbf{Q})$, and is,

$$\mathbf{M}_\perp = \hat{\mathbf{Q}}\times\left(\mathbf{M}\times\hat{\mathbf{Q}}\right) = \mathbf{M} - \hat{\mathbf{Q}}\left(\hat{\mathbf{Q}}\cdot\mathbf{M}\right), \tag{2.10}$$

and one can see that $\mathbf{M}_\perp$ is the component of the electron's spin moment, $\mathbf{M}$, projected onto the plane perpendicular to $\hat{\mathbf{Q}}$. Essentially, if the spin moment is parallel to $\mathbf{Q}$, there will be no scattered intensity. In the next section, we will evaluate the cross sections when we know the spin state of the neutron (polarized neutron scattering). For now, we will ignore it as well as the nuclear scattering, and present the double differential cross section for the magnetic scattering of unpolarized neutrons,

$$\frac{d^2\sigma}{d\mathbf{\Omega}_f dE_f} = \frac{N}{\hbar}\frac{k_f}{k_i}p^2 e^{-2W}\sum_{\alpha,\beta}\left(\delta_{\alpha\beta} - \hat{Q}_\alpha\hat{Q}_\beta\right)S^{\alpha\beta}\left(\mathbf{Q},\hbar\omega\right) \tag{2.11}$$

$$S^{\alpha\beta}\left(\mathbf{Q},\hbar\omega\right) = \frac{1}{2\pi}\int_{-\infty}^{\infty} dt e^{-i\hbar\omega t}\sum_l e^{i\mathbf{Q}\cdot\mathbf{r}_l}\left\langle M_0^\alpha(0)M_l^\beta(t)\right\rangle \tag{2.12}$$

where the factor, $\delta_{\alpha\beta} - \hat{Q}_\alpha\hat{Q}_\beta$, introduces the directional dependence on $\mathbf{Q}$ not seen in nuclear scattering.

From Eq. 2.12, we can see the scattering amplitude will be dependent on fluctuations in the system (like in nuclear coherent scattering), only now, they are magnetic fluctuations and are related to the magnetization correlation function, $G_{\alpha\beta}^{mag}(\mathbf{r},t)$. Eq. 2.12 can be separated into the static and fluctuating parts of the system [4],

$$S^{\alpha\beta}\left(\mathbf{Q},\hbar\omega\right) = S_{\langle M\rangle}^{\alpha\beta}\left(\mathbf{Q}\right)\delta(\hbar\omega) + S_{\langle mm\rangle}^{\alpha\beta}\left(\mathbf{Q},\hbar\omega\right), \tag{2.13}$$

where the subscripts $\langle M\rangle$ and $\langle mm\rangle$ are used to differentiate the two components. The first term comes from the static structure and is responsible for magnetic Bragg scattering and the second term, referred to as the dynamical correlation function, comes from fluctuations in the system and carries the inelastic spectral weight.

The coherent elastic scattering magnetic cross-section can be found by integrating the first term in Eq. 2.13 into Eq. 2.11,

$$\left.\frac{d\sigma}{d\Omega}\right|_{el}^{mag} = N_{mag}\frac{2\pi^3}{\upsilon_{mag}}\sum_{\mathbf{G}_{mag}}\delta\left(\mathbf{Q}-\mathbf{G}_{mag}\right)\left|\mathbf{F}_{mag}(\mathbf{G}_{mag})\right|^2, \tag{2.14}$$

where the subscript mag is used to specify that N_{mag}, υ_{mag} and $\mathbf{G}_{mag}$ are the number of magnetic unit cells, the volume of the magnetic unit cell, and the magnetic reciprocal space lattice vectors, respectively. $\mathbf{F}_{mag}(\mathbf{G}_{mag})$ is the static magnetic structure factor, and can be readily calculated if the magnetic structure is known. It is analogous to the static nuclear structure factor, and is,

$$\mathbf{F}_{mag}(\mathbf{G}_{mag}) = \sum_{l} p_l \mathbf{M}_{\perp,l} e^{i\mathbf{Q}_{mag}\cdot\mathbf{d}_l} e^{W_l}, \tag{2.15}$$

where now, the sum over l only runs over magnetic atoms in the unit cell.

The magnetic Bragg scattering is obviously elastic, but there is another type of scattering at zero energy transfer that appears in the dynamical correlation function for $S^{\alpha\beta}_{\langle mm\rangle}(\mathbf{Q},0)$. This is the quasi-elastic scattering and is responsible for the diffuse scattering observed in α-$NaMnO_2$. Diffuse scattering stems from correlations between moments causing the real-space relaxation of the moments about some mean value. This typically occurs in the vicinity of a phase transition or when short-range correlations are present (which can be due to frustration or disorder in a system). Above a critical ordering temperature, T_c, a system can be broken into regions across which there is a relatively even magnetization density. From region to region, the magnetization density is approximately constant, but the direction of magnetization will vary. The regions have a volume with dimensions proportional to ξ, which gets larger as T_c is approached, and diverges at T_c. At a given, fixed, temperature, the correlation function will have the form,

$$G^{mag}(\mathbf{r},t) \propto \frac{1}{|\mathbf{r}|} e^{-|\mathbf{r}|/\xi}. \tag{2.16}$$

Eq. 2.16 is for a three-dimensional system with the critical exponent $\eta = 0$ (a fair approximation when away from T_c). For a more in-depth discussion on critical exponents and the derivation of Eq. 2.16, see, for example, Ref. [5]. In a neutron scattering experiment, we measure the Fourier transform of Eq. 2.16, such that the scattering function will be proportional to,

$$S_{\langle mm\rangle}(\mathbf{Q},0) \propto \frac{1}{\kappa^2+Q^2}, \tag{2.17}$$

and $\kappa = 1/\xi$. This means critical scattering, as well as magnetic short range correlations, will have the form of a Lorenztian function in reciprocal space. As correlations become longer, Eq. 2.17 approaches a delta function, like for long-range order. The use of this relation is that the correlation length can be extracted to better understand the critical behavior or extent of interactions within a magnetic system.

The last part of $S^{\alpha\beta}(\mathbf{Q},\hbar\omega)$ to be discussed is $S^{\alpha\beta}_{\langle mm\rangle}(\mathbf{Q},\hbar\omega)$ with finite energy transfers ($\hbar\omega \neq 0$). This term describes the correlations of it's fluctuations around the equilibrium expectation value: $\mathbf{m_Q}(t) = \mathbf{M_Q}(t) - \langle \mathbf{M_Q}\rangle$ [4]. The dynamical correlation function obeys the detailed balance constraint, and is related to the imaginary part of the dynamical magnetic susceptibility via the fluctuation-dissipation theorem. These two results are derived from linear response theory and can be summarized in the following equations:

$$S^{\alpha\beta}_{\langle mm\rangle}(\mathbf{Q},\hbar\omega) = e^{-\hbar\omega/T} S^{\alpha\beta}_{\langle mm\rangle}(\mathbf{Q},-\hbar\omega) \tag{2.18}$$

$$\left(1-e^{-\hbar\omega/T}\right) S^{\alpha\beta}_{\langle mm\rangle}(\mathbf{Q},\hbar\omega) = \frac{1}{\pi}\chi''_{\alpha\beta}(\mathbf{Q},\omega) \tag{2.19}$$

where T is the system temperature in units of $\hbar\omega$. χ'' is the mean energy dissipation rate in a system in response to a field, which in this case, is the magnetization of the system.

Sum rules are an important result of the magnetic scattering function for analyzing neutron scattering data. The zero moment sum rule is obtained when Eq. 2.12 is integrated over all momentum in a Brillouin zone and energy. One obtains the total magnetic scattering available from a system. The result gives the relationship between the total scattered magnetic intensity and the spin value, regardless of if the system is

ordered or not,

$$\sum_{\alpha} \int \int_{-\infty}^{\infty} S^{\alpha\alpha}\left(\mathbf{Q}, \hbar\omega\right) \frac{V d^3\mathbf{Q}}{\left(2\pi\right)^3} d\hbar\omega = S\left(S+1\right). \tag{2.20}$$

Subsequent order moment sum rules can be calculated by taking the Fourier transform of the nth time derivative of the dynamical structure factor. The first-moment sum rule can be particularly useful for analyzing inelastic neutron scattering data in the single-mode approximation (SMA). The SMA describes a magnon where the excitation at a momentum $\mathbf{Q}$ is a delta function at a particular $\hbar\omega$. The first-moment sum rule is,

$$\int_{-\infty}^{\infty} S^{\alpha\alpha}\left(\mathbf{Q}, \hbar\omega\right) d\left(\hbar\omega\right) = \frac{1}{2N} \left\langle \left[\left[S_Q^{\alpha}, \mathbf{H} \right], S_{-Q}^{\alpha} \right] \right\rangle. \tag{2.21}$$

It should be noted that in this derivation from Ref. [6], the lattice is assumed to be centrosymmetric. Another feature of the scattering function is that different directional components contribute to the zero-order sum rule with different weights. Ref. [7] outlines how $S^{zz}(\mathbf{Q}, \hbar\omega)_{\text{elastic}}$, $S^{xx}(\mathbf{Q}, \hbar\omega) + S^{yy}(\mathbf{Q}, \hbar\omega)$ and $S^{zz}(\mathbf{Q}, \hbar\omega)_{\text{inelastic}}$ individually contribute to the total $S(S+1)$ spectral weight. This is touched upon in more detail in Ch. 7 because an $S^{zz}(\mathbf{Q}, \hbar\omega)_{\text{inelastic}}$ component (fluctuations along the ordered moment), which is not degenerate with the transverse inelastic $S^{xx}(\mathbf{Q}, \hbar\omega) + S^{yy}(\mathbf{Q}, \hbar\omega)$ component, is detected.

2.2 Neutron triple-axis spectrometer

2.2.1 Overview of important components

The triple-axis spectrometer allows one to probe a reciprocal space scattering plane with great precision in both momentum and energy. The three axes refer to the monochromator, the sample, and the analyzer. The monochromator axis determines the energy and direction of the incident beam, the sample axis determines how reciprocal lattice vector, $\mathbf{G}$, is oriented with respect to $\mathbf{Q}$, and the analyzer axis discriminates which energies and momentum get detected. A simple schematic is shown in Fig. 2.1. Collimations at

various points in the beam's path help to narrow the divergence of the beam. These are placed before the monochromator, before the sample, before the analyzer, and before the beam. The choice of collimation is usually a trade off between flux and resolution. Monochromators consist of a crystal oriented at a specific angle with respect to the white beam coming from the reactor that satisfies the Bragg condition for the desired energy to be reflected. For example, experiments done on BT7 at the NCNR used a PG(002) monochromator (where PG is pyrolytic graphite), where the d-spacing of the $(0, 0, 2)$ reflection is 3.35416 Å. Using Bragg's law, we can see the relationship between wavelength, Bragg angle, and d-spacing. BT7 has high-flux and relatively low $\lambda/2$ contamination (discussed shortly) at an energy of 14.7 meV. We can relate the desired energy to momentum,

$$E = \frac{\hbar^2 k^2}{2m_n}, \tag{2.22}$$

where m_n is the mass of the neutron and $\hbar$ is Planck's constant divided by 2π, and then momentum to wavelength,

$$k = \frac{2\pi}{\lambda}. \tag{2.23}$$

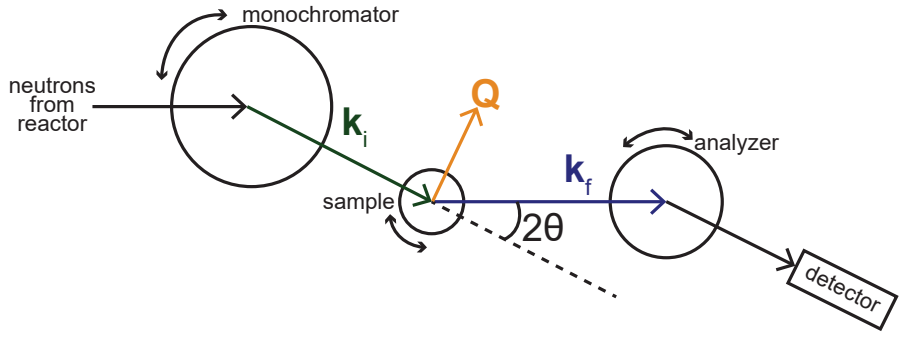

Figure 2.1: The basic components of a triple-axis spectrometer, as described in the text.

When the Bragg condition is met for a specific hkl of the crystal for wavelength λ_{hkl}, the Bragg condition for higher energy neutrons $\lambda_{2(hkl)} = \lambda_{(hkl)}/2$ is also met. This is because, here, $\mathbf{G}_{(002)} \parallel \mathbf{Q} \parallel \mathbf{G}_{(004)}$. This contamination would make anlaysis

of neutron data very difficult, so filters which essentially eliminate $\lambda/2$ contamination are placed before the monochromator and before the analyzer. Monochromators are typically curved to increase the focus and flux of the beam at the sample location. Collimators can tighten the divergence further, if desired. The triple-axis experiments in this thesis used Söller collimators to horizontally focus the beam. The collimator values are listed in arc minutes, and typical values can limit the beam divergence to between 0.1° and 1.5°. Lastly, the analyzer crystal before the detector works in much the same way as the monochromator crystal. The Bragg angle chooses the energy (which is the same as incident for elastic scattering) and can be focused or not focused when sent to the detector. The components of the triple-axis spectrometer discussed here are just a brief introduction to the complex instrument. Each instruments' specifics contribute to the overall resolution achieved at particular momentum and energy transfers and certain aspects of the instrument can be tailored to an experiments' needs. For more detailed information on monochromator and analyzer crystals, filters and collimators, see, for example, Ref. [1].

2.2.2 Resolution function

Analyzing triple-axis neutron data is as much about how many and where neutrons counts are detected as it is understanding the resolution function. A drawback of triple-axis scattering is that not including the resolution function of the particular instrument used can result in bad fits, and inaccurately reported parameters. The data collected from the spectrometer is a convolution of the resolution function, $\mathbf{R}(\mathbf{Q}-\mathbf{Q}_0, \omega-\omega_0)$, and the scattering function, $\mathbf{S}(\mathbf{Q},\omega)$, but luckily, the resolution function can often be well described by the Cooper-Nathans approximation [9]. The resolution function is peaked about the point at which one is probing in reciprocal space, $\mathbf{Q}$ and ω_0. Constant amplitude contours surround this point, forming nested ellipsoids throughout $(\mathbf{Q},\omega)$ space. The orientation, shape, and volume of the ellipsoids for given spectrometer geometry (i.e. collimations, handedness, monochromator/analyzer mosaic, etc.) depend only on the location being probed in reciprocal space.

For elastic scattering, knowing the resolution function makes it possible to extract sample mosaics and correlation lengths. For example, scattering from nuclear Bragg

peak will never have a full-width half-maximum (FWHM) narrower than the spectrometer resolution. Given a model cross section, the program ResLib [10] can convolute it with the resolution function and then fit one's data.

2.2.3 Polarized neutron scattering

The polarized neutrons used to for α-$NaMnO_2$ experiments were produced using cells filled with nuclear-spin polarized ^{3}He gas in conjunction with the triple-axis spectrometer, BT-7 at NCNR. The cross-section for a spin-up neutron passing through spin-polarized ^{3}He gas is very different than for a spin-down neutron, and thus, the attenuation for each will be drastically different, essentially, only letting one spin-state through [8]. Transmission will be greatest when the neutron spin-state is parallel with the ^{3}He polarization, denoted P_{He}. The transmission for neutrons with polarization parallel to P_{He} is denoted + and the transmission for neutrons antiparallel to P_{He} is denoted −. The two transmissions are,

$$T_{\pm} = T_E \exp\left[-\mathcal{O}\left(1 \mp P_{\mathrm{He}}\right)\right], \tag{2.24}$$

where T_E is the transmission of the glass cell, and $\mathcal{O} = 0.726 p\lambda l$, where λ is the neutron wavelength, p is the pressure in the cell, and l is the length of the cell. The polarization of the neutron beam, P_n, after passing through the ^{3}He cell will be,

$$P_n = \frac{T_+ - T_-}{T_+ + T_-} = \tanh\left(\mathcal{O} P_{\mathrm{He}}\right), \tag{2.25}$$

whereas the transmission of the polarized beam will be,

$$T_n = T_0 \cosh\left(\mathcal{O} P_{\mathrm{He}}\right), \tag{2.26}$$

and T_0 is the transmission of an unpolarized neutron beam passing through a ^{3}He cell with $P_{\mathrm{He}} = 0$. The flux of the neutron beam is greatly reduced during the polarization

process, as seen in Eq. 2.26, and the transmission gets worse with increasing P_n (ideally, one wants a high P_n and T_n).

The incident neutrons pass through a ^{3}He polarization after the monochrometer, where the polarization is maintained during the path to the sample via guide fields. The scattered neutrons pass through another polarizer just before the analyzer, meaning one can know the spin-state of the neutron before and after scattering. Control of the neutron spin-state is through the use of flippers. Flippers change the direction of the nuclear-spin state of the ^{3}He gas using the adiabatic fast passage nuclear magnetic resonance technique. Flipping the polarizers, in turn, changes which spin-state of the neutron gets transmitted. There are then four cross-sections that can be measured: $++$, $--$, $+-$, and $-+$. The $++$ and $--$ cross sections are called non spin-flip (NSF), and the $+-$ and $-+$ are called spin-flip (SF).

Before ignoring the spin state in the previous section, Eq. 2.9 was presented. Taking into account the possible combinations of spin states, $\sigma_i = +/-$ and $\sigma_f = +/-$, there are four $U^{\sigma_i\sigma_f}$ matrix elements:

$$\begin{aligned} U^{++} &= b - pM_{\perp z} \\ U^{--} &= b + pM_{\perp z} \\ U^{+-} &= -p\left(M_{\perp x} + iM_{\perp y}\right) \\ U^{-+} &= -p\left(M_{\perp x} - iM_{\perp y}\right) \end{aligned} \tag{2.27}$$

It is standard to define the z-axis to be parallel to the neutron polarization axis, $\mathbf{P}$. From Eqs. 2.27, one can see that nuclear scattering is always NSF, and magnetic scattering can be NSF or SF depending on the geometry at hand. In a standard polarized neutron triple-axis experiment, there are two geometries of $\mathbf{P}$ with respect to $\mathbf{Q}$: $\mathbf{P} \parallel \mathbf{Q}$ and $\mathbf{P} \perp \mathbf{Q}$. This means the z-axis changes with the direction of $\mathbf{P}$. The first configuration, $\mathbf{P} \parallel \mathbf{Q}$, is generally used to distinguish between nuclear and magnetic scattering. A peak that has a sudden onset at a particular temperature could, after all, be due to a structural change, so this configuration is usually the first experiment done to determine if there's any magnetic signal. The z component of $M_\perp$ will always be zero in this geometry and U^{++} and U^{--} will only have a nuclear contribution, if

one even exists at the particular **Q** being probed. The second configuration, **P**⊥**Q**, is generally used to determine the direction of the moment, however, one must be cautious when picking the scattering plane and momentum at which to measure. Because the neutrons are only sensitive to the component of **M** perpendicular to **Q**, the experimenter should choose a configuration which minimizes the component of **M** that projects onto **Q**. There exists a relationship between magnetic peak intensity in the different SF/NSF channels and the neutron polarization direction for collinear antiferromagnets,

$$\begin{aligned} I_{\text{mag}}^{++} &= I_{\text{mag}}^{--} = I_0 \cos^2\gamma \\ I_{\text{mag}}^{+-} &= I_{\text{mag}}^{-+} = I_0 \sin^2\gamma, \end{aligned} \tag{2.28}$$

which leads to the relationship,

$$\tan\gamma = \left(\frac{I_{\text{mag}}^{+-}}{I_{\text{mag}}^{++}}\right)^{1/2}, \tag{2.29}$$

where γ is the angle between $\mathbf{M}_\perp$ and $\hat{\mathbf{P}}$.

Because the neutron beam polarization process is not perfect (i.e. $P_{\text{He}} \neq 1$ and $P_n \neq 1$), efficiency corrections need to be made when analyzing data. This is typically done using the flipping ratio,

$$F = T_+/T_- = \exp\left(2\mathcal{O}P_{\text{He}}\right). \tag{2.30}$$

The flipping ratio will decrease with time, and must be calculated at various points throughout the use of a set of ^{3}He cells in order to do proper corrections. An easy way to calculate the flipping ratio, and the way it was done in this dissertation, is to scan over a nuclear Bragg peak in both a NSF and SF configuration. From the $U^{\sigma_i\sigma_f}$ amplitudes, we know all the nuclear intensity should be in the NSF channel and the flipping ratio ends up being $I_{nuc}^{++}/I_{nuc}^{+-}$ (or any combination of of $I_{nuc}^{\text{NSF}}/I_{nuc}^{\text{SF}}$).

The experimental setup for polarized elastic experiments on α-$NaMnO_2$ probing the magnetic zone center, $\mathbf{Q} = (0.5, 0.5, 0)$, is shown in Figs. 2.2 (a) and (b). The scattering

plane is $(H, K, 0)$, and the crystallographic c-axis is perpendicular to this plane, with α denoting the angle between the crystallographic c-axis and the moment vector, $\mathbf{M}$. Fig. 7.1 (c) shows the results of $(0.5, K, 0)$ scans through the magnetic zone center in the $\mathbf{Q}\perp\mathbf{P}$ configuration. After polarization correction and fitting, γ was found to be $23.4° \pm 0.4°$. In this geometry, there is a projection of the moment along $\mathbf{Q}$, but it is very small. Because of this, γ is not the same as α, and Fig. 2.3 shows a simulation of γ versus α. The simulation created a range of α angles, as well as the corresponding $\mathbf{M}$ vectors. It was assumed that there was no projection of $\mathbf{M}$ along the b-axis. $\mathbf{M}_\perp$ was calculated using the relation given in Eq. 2.10, with $\hat{\mathbf{Q}}$ being the unit vector along $\mathbf{Q} = (0.5, 0.5, 0)$. Then, γ was found using Eq. 2.29. The dashed black line in Fig. 2.3 is a reference $x = y$ line to show the deviation from a 1 : 1 correspondence that α and γ would have in this configuration if there were no projection of $\mathbf{M}$ along $\mathbf{Q}$. The inset

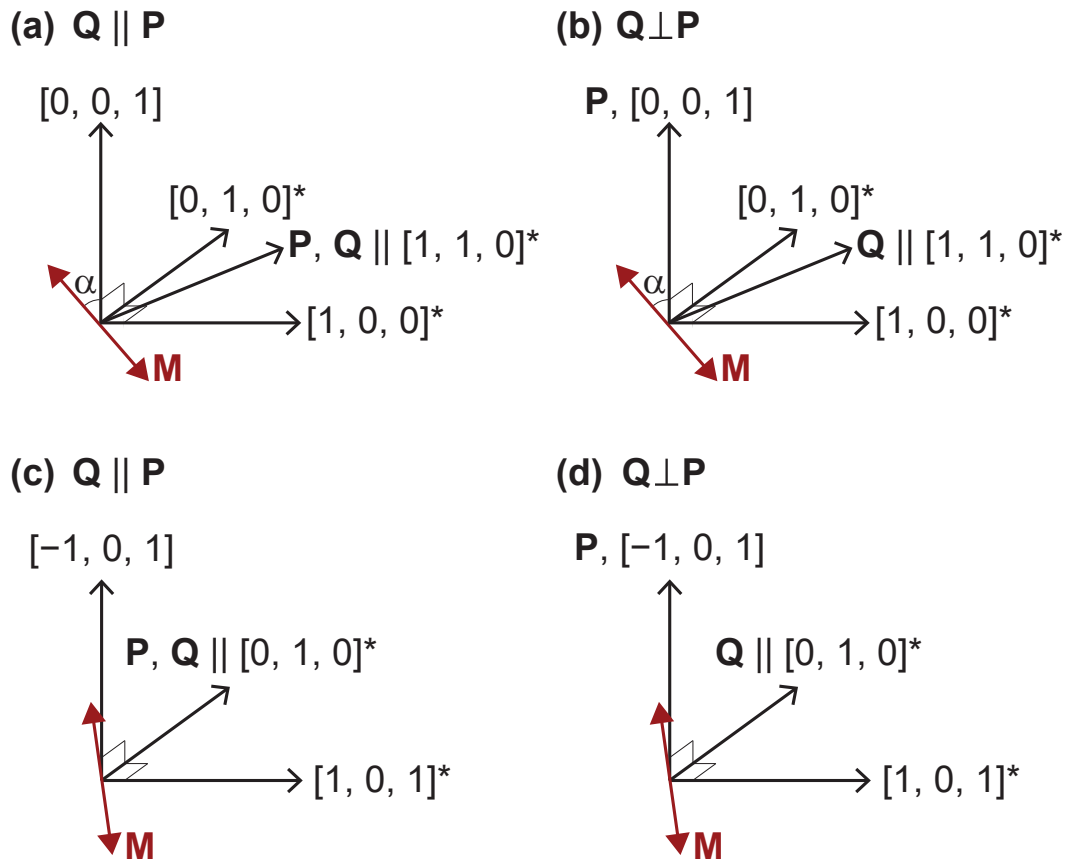

Figure 2.2: The different geometries used for polarized neutron scattering experiments on α-$NaMnO_2$. Panels (a) and (b) were used to probe the 3D magnetic zone center, $\mathbf{Q} = (0.5, 0.5, 0)$, and represent the $\mathbf{Q} \parallel \mathbf{P}$ and $\mathbf{Q}\perp\mathbf{P}$ configurations, respectively. Panels (c) and (d) were used to probe the magnon dynamics at the 1D magnetic zone center, $\mathbf{Q} = (0, 1.5, 0)$, and represent the $\mathbf{Q} \parallel \mathbf{P}$ and $\mathbf{Q}\perp\mathbf{P}$ configurations, respectively.

of Fig. 2.3 shows a zoomed in region of the main plot about the calculated γ from the data. The shaded region around the $\gamma = 23.4°$ line in blue represents the extent of the error bars. The value of α is shown as the green line (with the corresponding error represented by the surrounding shaded region) and was extracted to be $\alpha = 26.3° \pm 0.4°$.

Once the moment direction was confirmed to be approximately along the $[-1, 0, 1]$ direction, we could utilize the experimental setup shown in Figs. 2.2 (c) and (d) for inelastic experiments probing the quasi-1D magnetic zone center, $\mathbf{Q} = \left(0, \frac{3}{2}, 0\right)$. In this configuration, the moment is either entirely along the neutron polarization in the $\mathbf{Q} \perp \mathbf{P}$ configuration or entirely perpendicular to it in the $\mathbf{Q} \parallel \mathbf{P}$ configuration. In the polarized inelastic study, we were concerned with determining if an excitation was magnetic using the geometry in Fig. 2.2 (c), and then, after that determination, understanding the direction of the moments' fluctuations using the geometry in Fig. 2.2 (d). More detail on this experiment is given in Ch. 7, but the same relationships between scattering vector, polarization, and direction of moment that were just discussed for elastic polarized scattering apply.

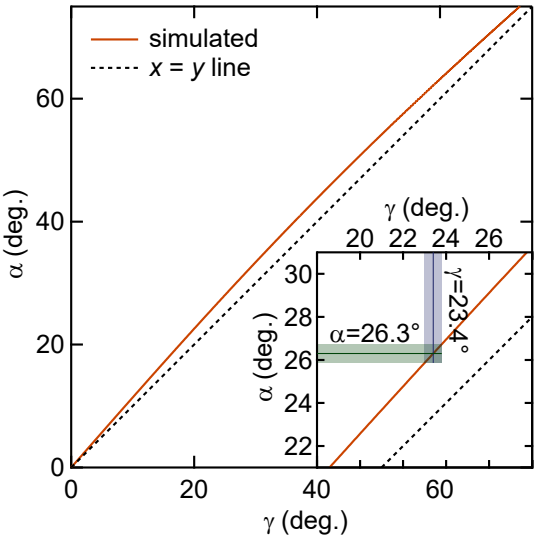

Figure 2.3: Simulation showing what an angle of α (the angle between the total spin moment and the neutron polarization) would give for γ (the angle between the component of spin which is projected onto the plane perpendicular to $\mathbf{Q}$ and the neutron polarization) in a polarized neutron scattering experiment on α-$NaMnO_2$, with the configuration shown in Fig. 2.2 (b). The dashed line is a straight $x = y$ reference to highlight the non-linear relationship between α and γ. The inset is zoomed in on the region where γ was found experimentally. The shaded regions indicate the error.

2.3 Neutron time-of-flight spectrometers

Neutron time-of-flight (TOF) instruments are capable of efficiently probing large areas of energy and momentum space. The basic operating principle is that a neutrons' kinetic energy transfer is determined by the time it takes to get between two known points through the DeBroglie relationship: $\lambda = h/mv$, where λ is the neutron wavelength, h is the Planck constant, m is the neutron mass, and v is the neutron velocity. Large banks of detectors are setup to to determine where the neutron is coming from, thus determining its momentum. Because TOF scattering relies on timing, a pulsed neutron source is needed to keep track of when neutrons reach the sample versus the detectors. If at a reactor source, a Fermi chopper (a disc with a slit in it) is spun at specific frequencies to create pulses of neutrons. At a spallation neutron source, the pulses are built-in to the neutron production.

The energy resolution, $\Delta E/E$, of triple-axis spectrometers gets worse with increasing energy; however, it is the opposite case for TOF instruments. An advantage of TOF instruments is that the scattered intensity can be normalized to an absolute scale. This is achieved by using a vanadium standard, which has such a small coherent cross-section, the scattering can be approximated as completely incoherent. First, by scattering off vanadium, individual detector efficiencies and the incident flux profile can be corrected, because vanadium should be causing equal, and isotropic, scattering of the incident beam. And second, by normalizing, the data can be converted to the absolute scale of barns per steradian. This is especially helpful when determining how the total spectral weight is divided (i.e. sum rules). TOF instruments can be classified into two general groups: direct geometry spectrometers and indirect geometry spectrometers.

A direct geometry spectrometer uses a monochromatic beam so that neutrons have a well-defined energy and momentum when they reach the sample. This is typically achieved with a series of neutron-absorbing Fermi choppers [11] which serve as velocity selectors. The frequency of the choppers can be changed, which corresponds to changing the incident energy, and the size of the slit determines the resolution. The smaller the slit, the better the resolution, but flux is sacrificed. The direct geometry spectrometer, SEQUOIA, was used to study the spin waves in single crystals of α-$NaMnO_2$ in Ch. 7. Indirect geometry spectrometers illuminate a sample with a white beam of neutrons and

the scattered neutrons are selected with analyzer crystals or choppers. Data from Ch. 6 utilized the TOF instrument, CORELLI, which is a diffraction instrument that uses an incident white beam and a series of complex optics for energy discrimination in order to reconstruct quasi-elastic signals, like those discussed in Section 2.1.2.

References

[1] Shirane, G., Shapiro, S. M. & Tranquada, J. M. *Neutron scattering with a triple-axis spectrometer : basic techniques* (Cambridge University Press, New York, 2002).

[2] Van Hove, L. Correlations in Space and Time and Born Approximation Scattering in Systems of Interacting Particles. *Phys. Rev.* **95**, 249–262 (1954).

[3] Halpern, O. & Johnson, M. H. On the Magnetic Scattering of Neutrons. *Phys. Rev.* **55**, 898–923 (1939).

[4] *Modern techniques for characterizing magnetic materials* (Kluwer Academic Publishers, Boston, 2005).

[5] Collins, M. F. *Magnetic critical scattering* (Oxford University Press, New York, 1989).

[6] Hohenberg, P. C. & Brinkman, W. F. Sum rules for the frequency spectrum of linear magnetic chains. *Phys. Rev. B* **10**, 128–131 (1974).

[7] Huberman, T. Two-magnon excitations observed by neutron scattering in the two-dimensional spin-5/2 Heisenberg antiferromagnet Rb_2MnF_4. *Phys. Rev. B* **72** (2005).

[8] Chen, W. C. *et al.* ^{3}He spin filter based polarized neutron capability at the NIST Center for Neutron Research. *Journal of Physics: Conference Series* **528**, 012014 (2014).

[9] Cooper, M. J. & Nathans, R. The resolution function in neutron diffractometry. I. The resolution function of a neutron diffractometer and its application to phonon measurements. *Acta Crystallogr.* **23** (1967).

[10] Zheludev, A. Reslib (eth zürich) (2009).

[11] Stone, M. B. *et al.* A comparison of four direct geometry time-of-flight spectrometers at the spallation neutron source. *Review of Scientific Instruments* **85**, 045113 (2014).

Chapter 3

$Na_4Ir_3O_8$ and $Na_3Ir_3O_8$ synthesis and characterization

The work presented in this chapter is the result of collaborations and authorship is shared. Previous publication of this data and analysis can be found in *Physical Review Letters*:

> Dally, R., Hogan, T., Amato, A., Luetkens, H., Bains, C., Rodriguez-Rivera, J., Graf, M. J. and Wilson., S. D. Short-Range Correlations in the Magnetic Ground State of $Na_4Ir_3O_8$. *Phys. Rev. Lett.* **113**, 247601 (2014).

The work from Section 3.5 was made possible by H. Zheng and J. F. Mitchell, who synthesized and provided single crystals for the REXS experiment. Details of the ingenious growth technique used, as well as additional data and characterization can be found in *Physical Review Materials*:

> Zheng, H., Zhang, J., Stoumpos, C. C., Ren, Y., Chen, Y.-S., Dally, R., Wilson, S. D., Islam, Z. and Mitchell, J. F. Controlled vapor crystal growth of $Na_4Ir_3O_8$: A three-dimensional quantum spin liquid candidate. *Phys. Rev. Materials* **2**, 043403 (2018).

3.1 Polycrystalline sample synthesis

Polycrystalline $Na_4Ir_3O_8$ (Na-438) was prepared in a manner similar to earlier reports [1, 2]. In creating $Na_4Ir_3O_8$, stoichiometric amounts of Na_2CO_3 (Alfa Aesar 99.99%) and IrO_2 (Alfa Aesar 99.98%) powders were ground and pressed into pellets, which were sintered at 750 °C for 20 hours. The pellets were then ground and repressed, and the new pellet was sintered at 1025 °C for 20 hours before being quenched in air. Samples were characterized using a Bruker XRD D2 Phaser, where phase purity of the powder was confirmed via x-ray diffraction measurements shown in Fig. 3.1 (a). The XRD refinement for Na-438 matched well to the crystal structure (Fig. 3.1 (c)) reported previously [3].

$Na_3Ir_3O_8$ (Na-338) was prepared by converting Na-438 into Na-338 via post-reaction chemical treatment. A 5:1 volume ratio of DI water and concentrated HCl (37%) was poured into a beaker with Na-438 and stirred. The proposed reaction is: ($2HCl + 2Na_4Ir_3O_8 \rightarrow 2Na_3Ir_3O_8 + 2NaCl + H_2$). After the reaction was completed, a large volume of DI water was added, and the solution was filtered using filter paper. NaCl was the only residue, other than $Na_{3+x}Ir_3O_8$, observed after filtration, and the $Na_{3+x}Ir_3O_8$ powder was found to be stable in air over a time period of months. The phase purity

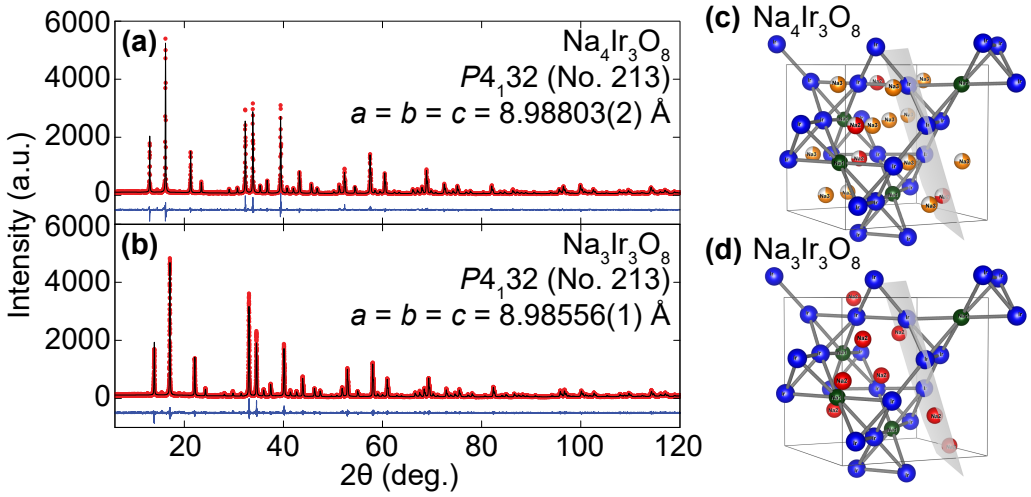

Figure 3.1: Room temperature X-ray diffraction measurements collected with a Cu-K_α source for (a) Na-438 and (b) Na-338. Panels (c) and (d) show the crystal structures of Na-438 and Na-338. Ir atoms are denoted as blue spheres, and Na(1), Na(2), and Na(3) sites are denoted by green, red and orange spheres respectively. Oxygen atoms are not plotted for clarity, and the (3,1,1) plane is highlighted.

was confirmed via x-ray diffraction measurements shown in Fig. 3.1 (b), which matched the previously reported crystal structure (shown in Fig. 3.1 (d)) [4]. The precise value of Na-content is difficult to definitively determine with lab x-rays; however Na-occupancies refined within error to nominal values, and susceptibility data were found to also be consistent with that of reported Na-338 [4]. For simplicity in this manuscript, we label the Na-reduced $Na_{3+x}Ir_3O_8$ product as Na-338.

3.2 $Na_4Ir_3O_8$ decomposition in atmosphere

3.2.1 XRD Measurements

We found that Na-438 gradually decomposes upon exposure to atmosphere into $Na_{3+x}Ir_3O_8$; hence care was taken to minimize its exposure to air and samples were manipulated in an inert atmosphere. This behavior is similar to the decomposition reported in another high alkali content iridate, Na_2IrO_3 [5]. The precise evolution of the structure of Na-438 once exposed to atmosphere is unknown, and we use the intentionally converted Na-338 as a reference for the electronic response of Na-deficient (ie. carrier doped) Na-438. As a measure of the structural evolution of Na-438 upon exposure to atmosphere, we performed periodic x-ray diffraction measurements on a powder sample left exposed in air. The results are plotted in Fig. 3.2 showing the evolution of Bragg intensities from those

of pristine Na-438 toward an altered end-point approaching a structure resembling that of Na-338. This particular batch of Na-438 powder exhibited a 4.8% molar fraction of Na_2IrO_3, which decomposed below measurement resolution upon exposure to air. Peak profiles did not broaden substantially upon exposure to atmosphere, consistent with the chemical conversion to a phase similar to Na-338.

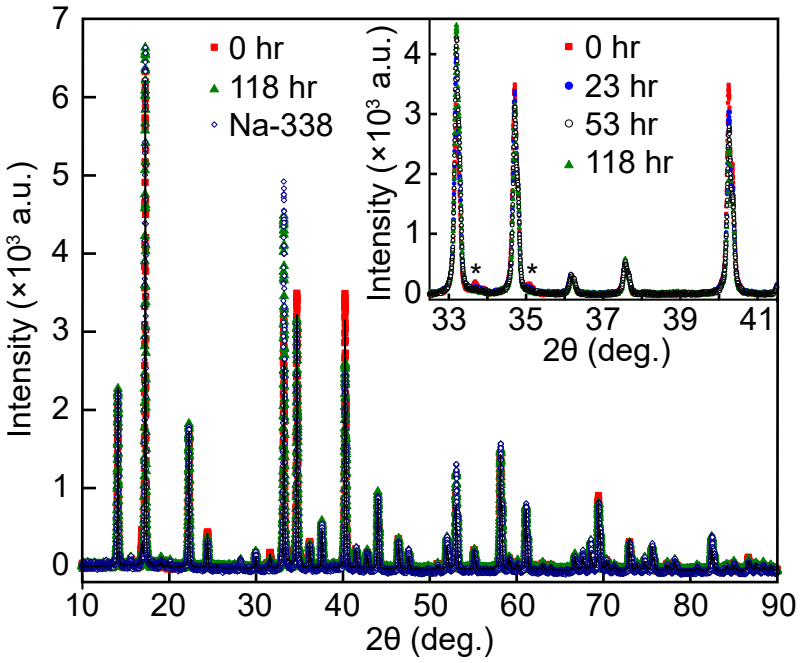

Figure 3.2: X-ray diffraction measurements showing the evolution of the Na-438's structure with exposure to atmosphere. As-grown powder is denoted by red squares and data for powder exposed for 118 hours are plotted as green triangles. Chemically converted Na-338 is shown for reference (open diamonds) and the solid black line is the structural refinement for pristine Na-438. Inset shows the time evolution of the Bragg peaks for powders exposed for variable amounts of time. Asterisks in the inset denote a small amount of Na_2IrO_3 impurity phase and its decomposition over time.

3.2.2 Irreversibility measurements

Magnetization measurements were performed in a Quantum Design MPMS3 magnetometer, and the susceptibility measurements for both Na-438 and Na-338 are plotted in Fig. 3.3. A Curie-Weiss fit for Na-438 (75 K$< T <$ 300 K), shown in the inset of Fig. 3.3 (b) yielded a Θ_{CW} = 555 K and an effective local moment of 2.10 μ_B. The local moment is larger than the maximum moment expected for a simple $S = \frac{1}{2}$ system, consistent with the larger values from earlier reports [1, 2]. We stress here that this is an effective fit, and the high temperatures required for a quantitative fit are inaccessible due sample decomposition. Below the breakdown of Curie-Weiss behavior, a cusp

appears peaked at $T_F = 6$ K in the zero-field cooled (ZFC) susceptibility. This peak coincides with the onset of irreversibility when compared with field-cooled (FC) data, and field sweeps at 1.8 K reveal the onset of a frozen state with a finite coercive field (Fig. 3.3 (a) inset). Once powder from this same batch is converted into Na-338, the nominal doping of $\frac{1}{3}$ of Ir-sites to Ir^{5+} causes this cusp to disappear.

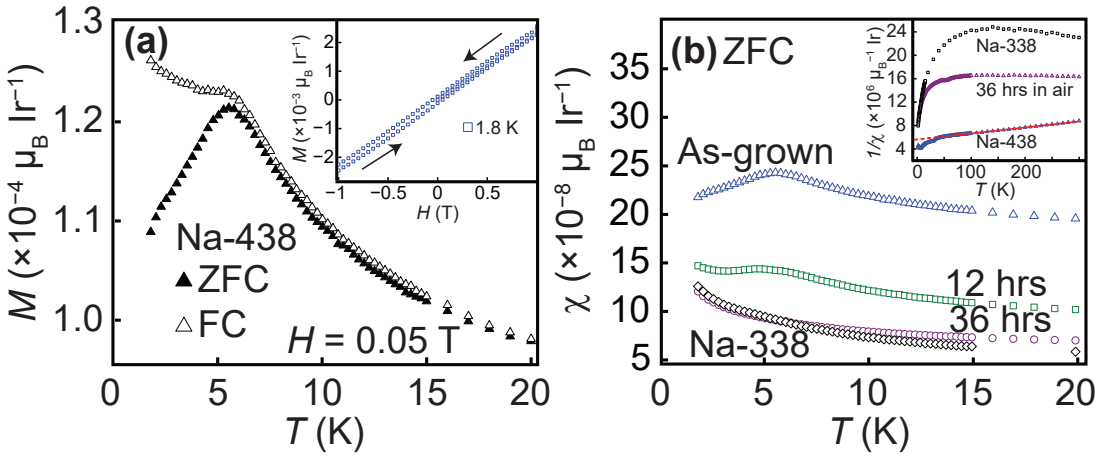

Figure 3.3: (a) Bulk magnetization collected for Na-438 under both FC (closed symbols) and ZFC (open symbols). The inset shows the magnetization, M, versus applied field H both above and below T_F. (b) ZFC static spin susceptibility plotted for as-grown Na-438 (blue triangles) as well as Na-438 left in air for 12 hours (green squares), 36 hours (purple circles), and converted Na-338 (black diamonds). Inset shows $\chi^{-1}(T)$ for as-grown Na-438, 36 hour exposed Na-438, and Na-338. Line is Curie-Weiss fit.

The frozen state below 6 K in Na-438 is fragile and gradually diminishes upon exposure to air as shown in Fig. 3.3 (b), and the structural conversion can be tracked via x-ray measurements shown in Fig. 3.2. We note here that high-temperature $M(T)$ data of Na-338 exhibits a positive slope [4], and hence any admixture of Na-338 within Na-438 will increase the apparent value for Θ_{CW} (Fig. 3.3 (b) inset). This may explain the variability in previous susceptibility measurements [1, 2]. Fig. 3.3 (b) illustrates the disappearance of the cusp in the static susceptibility as a function of exposure to atmosphere. Fig. 3.4 shows the corresponding disappearance of the irreversibility by plotting the field-cooled (FC) minus zero-field cooled susceptibility of Na-438 powder exposed to atmosphere. As the sample is continuously exposed to atmosphere and Ir-sites are doped via the removal of Na from the matrix, the irreversible behavior below 6 K gradually diminishes. This further supports the collapse of the T_F phase as the sample degrades.

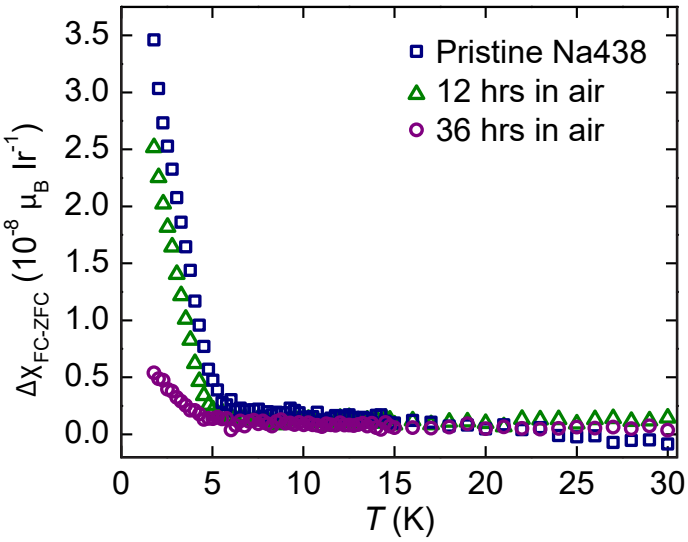

Figure 3.4: Field-cooled (FC) minus zero-field cooled (ZFC) static spin susceptibility, $\Delta\chi_{\mathrm{FC-ZFC}}$, of Na-438 as a function of exposure time to atmosphere.

3.3 Neutron diffraction data on MACS

To further probe spin correlations in $Na_4Ir_3O_8$, we performed neutron scattering measurements on polycrystalline samples at the MACS spectrometer at the NIST Center for Neutron Research. A double focusing pyrolitic graphite (PG) monochromator was used as well as a PG analyzer with fixed final energy of 3.7 meV. A BeO filter was used before the analyzer. Data from both energy integrated diffraction detectors and energy analyzed, elastic, detectors were collected. We anticipate the magnetic scattering to be very weak in this powder due to the small Ir-moment and short-range order; hence MACS was chosen due to its high-flux, large detector coverage, and the ability to reduce background via the use of an analyzer. 8 g of Na-438 powder was loaded into a flat-plate sample holder in order to minimize neutron absorption, and the sample was loaded inside of a gas-flow He cryostat. The resulting energy integrated diffraction data are plotted 2 K and 50 K are plotted in Fig. 3.5 (a).

Within resolution, the scattering at 2 K and 50 K appears unchanged in the energy integrated diffraction channel (the large powder lines at ≈ 3.25 Å^{-1} and ≈ 2.85 Å^{-1} are due to the sample holder). Energy analyzed, $\Delta E = 0$, scattering also shows no sign of correlated spin order emerging between 50 K and 2 K (Fig. 3.5 (b)). This does not however preclude a small moment ($\mu_{\mathrm{AF}} < 0.5\mu_B$), short-range ordered magnetic phase in this system. Small moments and short-range magnetic order are traditionally difficult

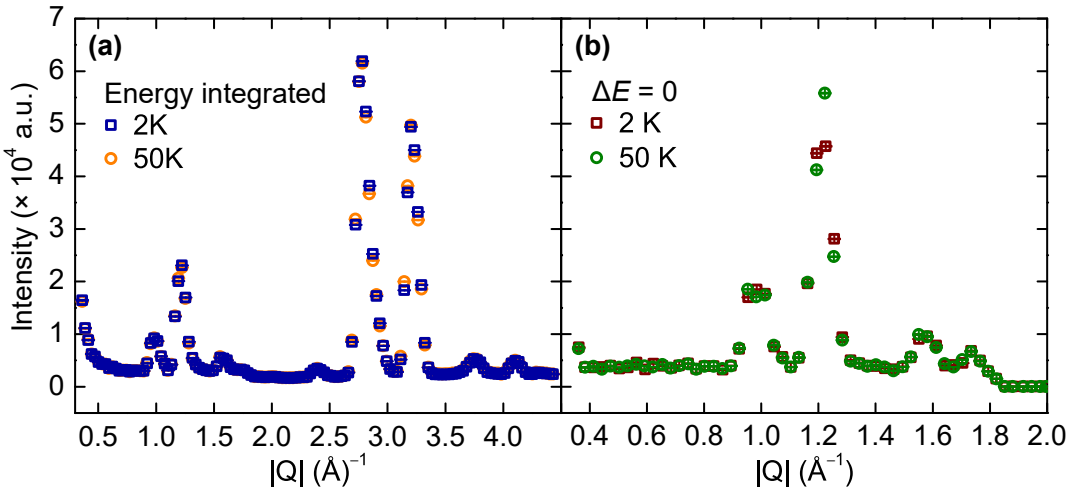

Figure 3.5: (a) Powder neutron diffraction data of Na-438 collected with the energy integrated diffraction detectors on the MACS spectrometer both below ($T = 2$ K) and above ($T = 50$ K) T_F, and (b) the same data but collected with the energy analyzed detectors ($\Delta E = 0$).

to resolve in simple powder diffraction measurements, and the large neutron absorption cross section of iridium adds an additional complication that limits experimental resolution. Future single crystal measurements using neutrons or resonant x-ray scattering will be required to fully explore the momentum dependence of the frozen-order.

3.4 Single-crystal resonant elastic x-ray scattering measurements

This work was done in conjunction with collaborators who provided single crystals of $Na_4Ir_3O_8$. Their synthesis methods and sample characterization can be found in Ref. [6], along with this section's resonant elastic x-ray scattering data. Typically, neutrons are superior when probing for magnetic order, but barriers such as small crystal size and absorption can make resonant x-ray scattering (REXS) a better choice, as is the case with the $Na_4Ir_3O_8$ single-crystals. The findings from the previous section indicate that there is no long-range order down to $T = 2$ K, but the powder-averaged data, small moment, and absorption of neutrons due to Ir could have been limiting factors. Additionally, the cusp in susceptibility indicates some order, and REXS can probe short-range correlations.

3.5 Superstructure

The data were taken on the high-resolution beamline, 6-ID-B, at the Advanced Photon Source at Argonne National Laboratory. REXS can probe orbital ordering as well as magnetic scattering, and because of the high flux at the synchrotron, can also see weak Bragg scattering that isn't obvious in powder x-ray diffraction. Surprisingly, what was found, were weak, but coherent, superlattice peaks at $\left(\frac{1}{3},\frac{1}{3},\frac{1}{3}\right)$-type positions, which were structural in origin. Fig. 3.6 shows mesh plots of typical $\left(\frac{1}{3},\frac{1}{3},\frac{1}{3}\right)$-type peaks, which are satellites of the $(6,6,1)$ zone-center ($L = 1\frac{1}{3}$ for both scans). These data were taken at $T = 1.8$ K in the $\sigma - \sigma$ channel, and below the absorption edge at 11.2 keV to minimize heating effects and maximize signal. A typical scan along H in both the $\sigma - \sigma$ and $\sigma - \pi$ channels at the Ir L_3-edge in Fig. 3.7 (a) demonstrates that the peak is structural in origin, as it is only in the $\sigma - \sigma$ channel. As a last check to make sure there is no resonant enhancement of the superstructure peaks, an energy scan about the Ir L_3-edge was performed at $\mathbf{Q} = \left(6\frac{1}{3}, 6\frac{1}{3}, 1\frac{1}{3}\right)$, and is shown in Fig. 3.7 (b). Only absorption effects, typical of Ir, can be seen.

It is thought that the superstructure originates from Na ordering within the lattice. The first reported structure from powder x-ray diffraction demonstrated disorder among the two Na sites. Powder diffraction does a good job at averaging over disorder, which is why the superstructure could not be detected.

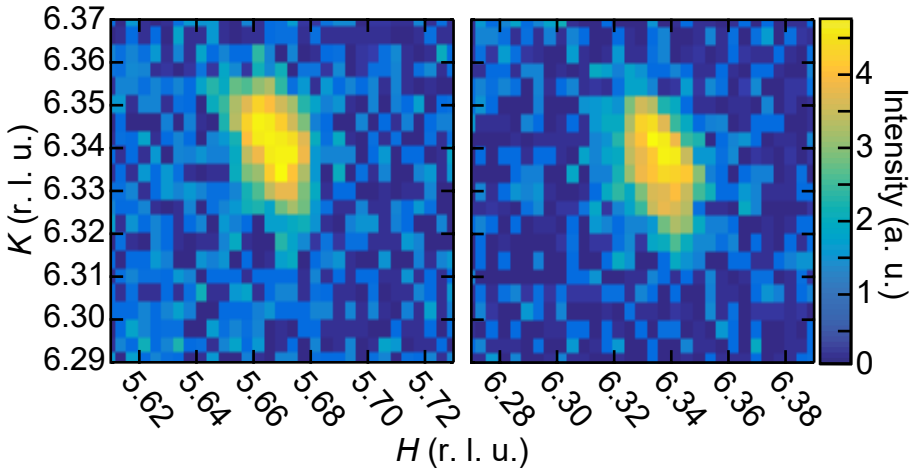

Figure 3.6: A representative (H, K) map of scattering at $T = 1.8$ K about the $\left(\frac{1}{3},\frac{1}{3},\frac{1}{3}\right)$ satellite peaks at the $(6,6,1)$ zone center. The L value is $1\frac{1}{3}$.

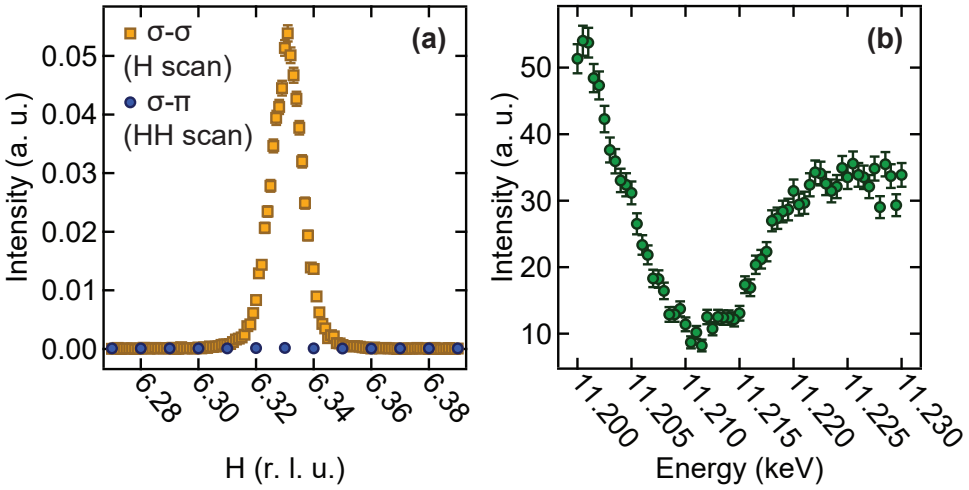

Figure 3.7: (a) H scan through the $\left(6\frac{1}{3}, 6\frac{1}{3}, 1\frac{1}{3}\right)$ satellite in both the $\sigma - \sigma$ and $\sigma - \pi$ scattering channels at $T = 1.8$ K. (b) Energy scan at $T = 1.8$ K conducted while sitting at $\mathbf{Q} = \left(6\frac{1}{3}, 6\frac{1}{3}, 1\frac{1}{3}\right)$.

Acknowledgments

We would like to thank Sean Giblin and Ram Seshadri for preliminary SQUID measurements. This work was supported in part by NSF CAREER award DMR-1056625 (S.D.W.). This work utilized facilities supported in part under NSF award DMR-0944772 and SQUID measurements were supported in part by grant DMR-1337567.

References

[1] Okamoto, Y., Nohara, M., Aruga-Katori, H. & Takagi, H. Spin-Liquid State in the $S = 1/2$ Hyperkagome Antiferromagnet $Na_4Ir_3O_8$. *Phys. Rev. Lett.* **99**, 137207 (2007).

[2] Singh, Y., Tokiwa, Y., Dong, J. & Gegenwart, P. Spin liquid close to a quantum critical point in $Na_4Ir_3O_8$. *Phys. Rev. B* **88**, 220413 (2013).

[3] Okamoto, Y., Nohara, M., Aruga-Katori, H. & Takagi, H. Spin-Liquid State in the $S = 1/2$ Hyperkagome Antiferromagnet $Na_4Ir_3O_8$. *Phys. Rev. Lett.* **99**, 137207 (2007).

[4] Takayama, Tomohiro and Yaresko, Alexander and Matsumoto, Akiyo and Nuss, Jürgen and Ishii, Kenji and Yoshida, Masahiro and Mizuki, Junichiro and Takagi, Hidenori. Spin-orbit coupling induced semi-metallic state in the 1/3 hole-doped hyper-kagome $Na_3Ir_3O_8$. *Scientific Reports* **4**, 6818 (2014).

[5] Krizan, J., Roudebush, J., Fox, G. & Cava, R. The chemical instability of Na_2IrO_3 in air. *Materials Research Bulletin* **52**, 162 – 166 (2014).

[6] Zheng, H. *et al.* Controlled vapor crystal growth of $Na_4Ir_3O_8$: A three-dimensional quantum spin liquid candidate. *Phys. Rev. Materials* **2**, 043403 (2018).

Chapter 4

The magnetic ground state of $Na_4Ir_3O_8$

The work presented in this chapter is the result of collaborations and authorship is shared. In particular, M.J. Graf was invaluable in collecting and analyzing the μSR data. Previous publication of this data and analysis can be found in *Physical Review Letters*:

> Dally, R., Hogan, T., Amato, A., Luetkens, H., Bains, C., Rodriguez-Rivera, J., Graf, M. J. and Wilson., S. D. Short-Range Correlations in the Magnetic Ground State of $Na_4Ir_3O_8$. *Phys. Rev. Lett.* **113**, 247601 (2014).

4.1 Introduction

Models of spin-orbit entangled $J_{eff} = 1/2$ electrons on edge-sharing octahedra have shown that the symmetric portions of the magnetic Heisenberg exchange coupling may cancel [1, 2, 3]. This opens the possibility for an antisymmetric, bond-dependent magnetic exchange that can be mapped into a Hamiltonian with a spin liquid ground state [4, 2]. In two-dimensions, the honeycomb lattice of $(Li,Na)_2IrO_3$ has been proposed to be close to this spin liquid regime [5, 6], and in three-dimensions the leading candidate for realizing this new spin-orbit driven spin liquid is the hyperkagome lattice of Ir moments in $Na_4Ir_3O_8$ (Na-438) [7].

While the geometric frustration of Ir moments on the hyperkagome lattice, the theorized $J_{eff} = 1/2$ ground state, and the edge-sharing octahedra in Na-438 comprise the theoretical requirements for stabilizing a spin liquid phase, a range of ordered magnetic ground states may instead stabilize depending on the relative strengths of competing exchange parameters as well as the relevance of Dzyaloshinskii-Moriya (DM) interactions [3]. As a result, a number of ordered states have also been proposed, ranging from fluctuation-driven nematic order [8] to a variety of antiferromagnetic states [3, 2]. Which magnetic ground state in Na-438 is realized, however, remains experimentally unresolved.

A high degree of magnetic frustration in Na-438 was initially suggested via the measurement of a large Curie-Weiss temperature $\Theta_{CW} \approx 680$ K and the absence of spin freezing above 6 K [7]. Magnetic heat capacity data, while revealing an anomalous peak near 30 K, similarly have shown no signature of ordering down to 0.5 K along with a linear term in the low temperature $C_{mag}(T)$—suggestive of gapless spin excitations in the

ground state [7, 6]. Furthermore, measurements of the magnetic Grüneisen parameter have hinted at a nearby quantum critical point [9]. While these studies have suggested an exotic spin liquid in the $J_{eff} = 1/2$ hyperkagome lattice, direct experimental probes of magnetic correlations in this material are notably absent. Thus the key question remains: In the ground state, do spins remain predominantly dynamic as expected for a spin liquid, or do spins ultimately freeze into static/quasi-static correlations?

Here we use muon spin relaxation (μSR) in conjunction with the results of the Ch. 3 to resolve that the hyperkagome lattice transitions into a quasi-static state frozen below 6 K with slow dynamics persisting down to 20 mK. Our μSR data reveal that an irreversibility in the static spin susceptibility below 6 K arises from the bulk of the spins in the system freezing and not a dilute impurity effect. The resulting magnetic ground state differs qualitatively from that expected of an intrinsically dynamic quantum ground state such as a quantum spin liquid, and, instead, moments freeze into a configuration of densely packed spins with short-range correlations confined to the length scale of one unit cell. Our combined results point toward an unusual ground state realized by J_{eff}=1/2 spins on a hyperkagome lattice with long-timescale, persistent fluctuations that coexist with spin freezing and resemble those observed in quantum spin ice and related materials. The recovered spin entropy in this material [9] can therefore be attributed to the onset of a short-range ordered magnetic ground state.

4.2 Muon spin relaxation experiment on $Na_4Ir_3O_8$

Zero field and longitudinal field μSR measurements were made at the Paul Scherrer Institute in a gas-flow cryostat over the range 1.6 K $< T <$ 13 K and in a dilution refrigerator over the range 20 mK $< T <$ 1.3 K. Data were analyzed using Musrfit software [10]; for a general review of the μSR technique, see Refs. [11], [12], and Appendix A.

In order to determine the origin of the irreversibility observed below 6 K in Na-438, we performed μSR measurements. μSR is volumetric probe capable of differentiating between local spin freezing from dilute impurities and a global transition of spins into a state with quasi-static order. Fig. 4.1 (a) shows the zero-field depolarization curves between $T = 12.7$ K and $T = 1.6$ K. The 12.7 K curve shows a very slow depolarization,

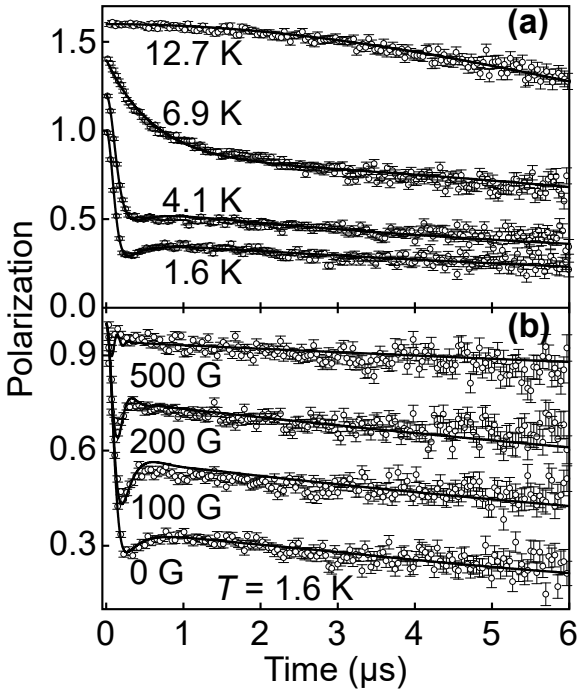

Figure 4.1: (a) Time dependence of the muon polarization at several temperatures (open symbols), along with the fits (solid lines), as described in the text. The curves are offset by equal increments of 0.2 for clarity (b) Muon depolarization at 1.6 K as a function of time at several longitudinal field values. Open symbols are the data, and the solid lines are fits described in the text. The error bars indicate one standard deviation.

typical of muon depolarization via small nuclear moments of fixed size and random orientation. This can be fit by the Gaussian Kubo-Toyabe depolarization function [13],

$$G_{GKT}(t) = \frac{2}{3}(1 - \Delta_N^2 t^2)e^{\frac{-\Delta_N^2 t^2}{2}} + \frac{1}{3} \tag{4.1}$$

where Δ_N is proportional to the root-mean-square of the local field distribution (assumed to be Gaussian) due to the nuclei at the muon stopping site, $\Delta_N = \gamma_\mu \langle B_{loc} \rangle_{rms}$, and γ_μ is the muon gyromagnetic ratio. The "$\frac{1}{3}$ tail" in Eq. 4.1 is a defining characteristic of depolarization by random local fields that are static on the muon timescale. From our fits at 12.7 K , we find $\Delta_N = 0.102(1)\ \mu s^{-1}$, a value consistent with depolarization by nuclear moments.

Below 10 K the depolarization takes on an exponential form, and the rate increases sharply with decreasing temperature. As the sample is cooled below 6.5 K, where the maximum in the static susceptibility is observed, we fit the depolarization with the phenomenological Gaussian-broadened Gaussian (GbG) function, $G_{GbG}(t)$, modified

with a slow exponential decay [14, 15, 13]. The form for the polarization is:

$$G(t) = (1-f)G_{GbG}(t)e^{-\lambda t} + fe^{-\lambda_{338}t} \tag{4.2}$$

and

$$G_{GbG}(t) = \frac{2}{3}\left(\frac{1+R^2}{\alpha}\right)^{\frac{3}{2}}\left(1-\frac{\Delta_W^2 t^2}{\alpha}\right)e^{\frac{-\Delta_W^2 t^2}{2\alpha}} + \frac{1}{3} \tag{4.3}$$

Here, $\alpha = 1 + R^2 + R^2\Delta_W^2 t^2$, $\Delta_W^2 = (W^2 + \Delta_0^2)^{\frac{1}{2}}$, and $R = W/\Delta_0$. This GbG form is simply a variation on the Gaussian Kubo-Toyabe function where the single local field distribution due to densely packed electronic moments is replaced by a Gaussian distribution of distributions with a mean value Δ_0 and width W. The form is known to describe systems where the muon depolarization is driven by disordered static magnetic moments with short-ranged correlations, e.g., the spin ice candidate $Yb_2Ti_2O_7$ [16] and the doped skutterudite $PrOs_4Sb_{12}$ [17]. A similar form of relaxation for muons in the presence of short-range order was recently derived analytically using statistical methods, providing a firm theoretical foundation for this association [18].

We allowed for a refined volume fraction of a Na-338 impurity phase, f, which is characterized by slow exponential damping with a nearly temperature independent rate λ_{338}. This additional damping term λ_{338} was independently measured (see Section 4.3.5), and the temperature independent fraction f was determined from the fits to the data at 1.6 K. The resulting fraction of impurity Na-338 phase within the nominally Na-438 powder was fit to be 6.6%, which likely arose from incidental exposure of the sample to atmosphere during transport. The remaining 93.4% of the sample volume below 6 K is well described by the GbG formalism, confirming that the entirety of the sample transitions into a quasi-static state.

In Fig. 4.2, we show the temperature variation of Δ_0, R, and λ. The sudden increase in Δ_0 and drop in R coincide with the peak in the magnetic susceptibility. We note here that the mismatch in the data between 1.3 and 1.6 K is due to the presence of a large background component in the data taken in the dilution refrigerator due to the silver sample holder (see Section 4.3.3). Both Δ_0 and λ parameters approach constant values upon cooling in contrast to the behavior of a canonical spin glass. Based on the

more accurate data taken in the gas flow cryostat, we take the low temperature values of Δ_0, R, and λ to be approximately 6.0 MHz, 0.4 and 0.1 μs^{-1}, respectively. From this value of Δ_0 we extract a characteristic field $\langle B \rangle_{rms} = \Delta_0/\gamma_\mu = 70$ G. The muon stopping site is unknown, but assuming that the muon experiences a dipolar field due to an Ir^{4+} magnetic moment located about half a unit cell away ($a = 8.988$ Å), we roughly estimate $\mu_{Ir} \approx 0.5\ \mu_B$, reasonable for the $J_{eff} = \frac{1}{2}$ state.

As an additional check of the quasi-static nature of the moments in Na-438, we also carried out measurements mapping the effect of a longitudinal magnetic field on the muon depolarization at $T = 1.6$ K. The data plotted in Fig. 4.1 (b) show that the $\frac{1}{3}$ tail at long timescales begins to be removed in an applied field of $H \gtrsim \langle B \rangle_{rms}$ and is completely suppressed under ≈ 500 G. This is an independent confirmation of the quasi-static nature of the depolarization and highlights the qualitative departure of the spin response from the dynamical, nearly field-independent, depolarization behavior expected for a spin liquid that only partially freezes below T_F [19].

We approximated the longitudinal field dependence of the GbG function by a finite sum of GKT functions shown in Fig. 4.1 (b) that each include fluctuations and an applied longitudinal field [11, 12]. Fits to this form under zero field yielded λ, Δ_0, and R values consistent with those of zero-field GbG fits. Changing the magnetic field values while keeping these parameters fixed yields good agreement with the data under applied fields, and validates our conclusion that the muon depolarization is caused by a quasi-static magnetic field distribution dressed with slow fluctuations.

Monte Carlo simulations [15] have shown that the ratio $R = W/\Delta_0$ is inversely proportional to the magnetic correlation length. In Na-438, the saturated region below T_F shows a fit $R = 0.4$, implying correlations that extend only over several nearest neighbor distances. Freezing of moments into a quasi-static state below 6 K can preclude the formation of a purely dynamical quantum spin-liquid ground state in Na-438. Instead, quasi-static moments coexist with long-timescale spin fluctuations, roughly mirroring the coexisting dynamic and freezing behavior reported in geometrically frustrated magnets such as $S = 1$ $NiGa_2S_4$ [20] and $S = \frac{1}{2}$ $Cu_3Ba(VO_5H)_2$ [21]. The degree of coexistence in this intermediate regime depends on the details of each system varying from predominantly static moments in Na-438 to the predominantly dynamic liquid

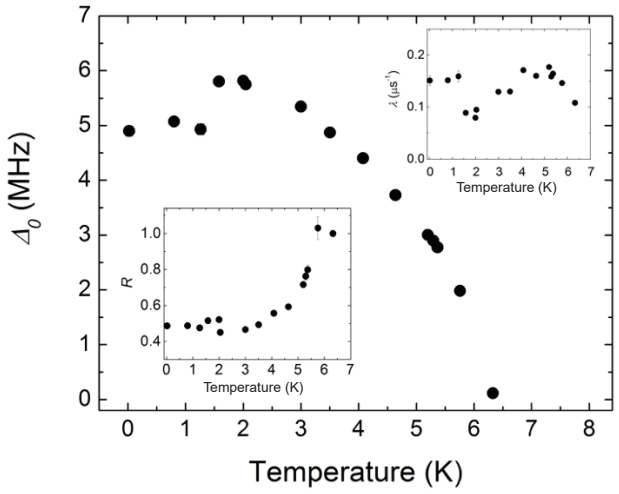

Figure 4.2: The mean value of the Gaussian-broadened Gaussian distribution (Eq. 4.3) as a function of temperature. Upper inset: Variation of the relaxation rate with temperature; discontinuity near 1.4K is due to a change in the sample environment described in the text. Lower inset: the temperature dependence of the ratio of width of distributions to the distribution mean. The error bars indicate one standard deviation of the fit parameters.

state in $Cu_3Ba(VO_5H)_2$; however it appears to be a generic feature of a proximate, highly degenerate, quantum ground state.

It is worth noting that systems far from frustration and well into an ordered regime may also show inhomogeneous short-range order and persistent fluctuations coexisting with conventional static order [22, 23]. The small $\frac{T_F}{\Theta_{CW}}$ ratio in Na-438 however suggests that the dichotomy between quasi-static order and persistent fluctuations is driven via interactions characteristic of frustration. This combined with the anomalous thermodynamic properties of Na-438 [9, 7] parallels the configurationally degenerate phases with fluctuating order (CDFO) observed in spin-ice and related phases [24, 16, 25] which possess short-range correlations that continue to fluctuate as $T \to 0$.

Theoretical studies have shown that an unfrustrated classical ground state should stabilize in Na-438 in the limit of strong spin-orbit interactions and direct Ir-O-Ir superexchange; however for direct Ir-Ir exchange, quantum fluctuations may remain relevant depending on the details of DM effects [3]. A Kitaev-Heisenberg model of $Na_4Ir_3O_8$ has similarly predicted an array of classically ordered phases with select regions of parameter space allowing for quantum disordered ground states [2]. A nematic order parameter, driven by fluctuations, has also been predicted to stabilize in Na-438 via an order-by-disorder mechanism [8]. Determining precisely which of these spin configura-

tions freezes requires a momentum resolved probe such as neutron scattering. Our initial neutron scattering data from Ch. 3 reveal no sign of magnetic correlations—implying a small ordered moment difficult to resolve in powder measurements. Future measurements on single crystals will be required to fully characterize the frozen state; however our data does allow models predicting the component field distribution felt by the muon to be tested using the approach of Yaouanc et al. [18].

Our observations are consistent with the formation of a CDFO phase in Na-438; however the freezing transition at 6 K is curiously absent from previously reported heat capacity data. Instead heat capacity reveals only a broad peak at 30 K that is also only weakly field dependent, presenting a theoretical challenge in reconciling the details of spin freezing and the higher temperature entropy release in this material. At lower temperatures, however, our data show that the magnetic entropy observed arises not from spins possessing purely dynamic, liquid-like, correlations in the quantum ground state but rather from frozen spins likely belonging to a growing class of CDFO phases that exhibit long-timescale damping coexisting within a short-range ordered, quasi-static spin state.

4.3 Muon spin relaxation experimental details

4.3.1 Sample mounting

For our μSR measurements at the Paul-Scherrer Institute, samples in the form of a course powder were contained in thin Mylar tape packets in the gas-flow cryostat. For measurements in the dilution refrigerator, the Na-438 and Na-338 powders were packed in thin silver foil and held on a silver plate. Samples were held at the base temperature for more than 10 hours to ensure that they were in thermal equilibrium with the refrigerator, with periodic measurements taken to confirm that the data did not vary with time and that equilibrium had been reached. As an additional confirmation, a different sample of Na-438 powder was mounted directly on a silver plate with very thin varnish; comparable long-time relaxation values on the order of $\lambda \approx 0.2\mu s^{-1}$ at 25 mK were obtained using this method.

4.3.2 Determination of the asymmetry

For the gas flow cryostat, the total asymmetry was measured at high temperatures ($T > 100$ K) in a small transverse field and the sum $A_0 + A_{BG}$ was fixed at that value for the low temperature fits. For the data taken in the dilution refrigerator, the total asymmetry was measured in small transverse fields at low temperatures on an empty silver sample holder.

4.3.3 Background term for Ag silver sample mount

For data collected within the dilution refrigerator, a silver sample holder was used and a background term was added to the muon $P(t)$ fit shown in Eq. 4.2. The background term $P_{BG}(t) = A_{BG}e^{-\lambda_{BG}t}$ was added to $P(t)$ where A_{BG} captures the depolarization associated with the silver sample holder used in the dilution refrigerator ($A_{BG} = 0$ for data taken in the gas flow cryostat). Weak transverse field measurements showed that $A_{BG}/(A_0 + A_{BG}) = 0.17(1)$. It was found that small variations in the actual value of A_{BG} may cause significant changes in the values of the fit parameters. This is the likely cause for the discontinuity in the depolarization rate λ and Δ_0 observed in transitioning from data collected in the gas-flow cryostat to the dilution fridge.

4.3.4 Longitudinal field model for the Gaussian-broadened Gaussian function

As no theoretical expression exists for the longitudinal field variation of the GbG depolarization function, we developed an approximate model to fit our longitudinal field data. The distribution of Gaussian distributions was replaced by a sum of 13 individual GKT functions, each of which includes the effects of a single fluctuation (or muon hopping) rate n and the presence of a longitudinal magnetic field. The Δ_{GKT} were set at equally spaced values centered on Δ_0, ranging from $\Delta_0 - 1.5W$ to $\Delta_0 + 1.5W$, while the relative amplitudes were weighted by a Gaussian distribution of width W about the mean Δ_0. For the plots presented in Fig. 4.1 (b), the asymmetry was left as a fitting parameter to account for the small field dependence of the relative detector sensitivities; the fractional reduction in the asymmetry relative to the zero field data was zero for the 100 G data, -0.028 for the 200 G data, and -0.040 for the 500 G data.

4.3.5 Muon depolarization in Na-338

We have also studied Na-338 via μSR. In Fig. 4.3 we show the zero-field depolarization at two temperatures. The depolarization has a slow exponential relaxation due to the majority phase Na-338 and a small contribution due to relaxation of muons in the Na-438 impurity phase present in the sample, as described in Section 4.2. The data are well-described by the depolarization function,

$$P(t) = (1-g)e^{-\lambda_{338}t} + gP_{438}(t), \tag{4.4}$$

where g is the volume fraction of Na-438, and $P_{438}(t)$ is the Na-438 depolarization function, given by either Eq. 4.1 or Eq. 4.2, depending on the temperature. The fits are shown in Fig. 4.3. We find that $g = 0.177(4)$ along with values for the Na-438 parameters that are consistent with those presented in Section 4.2. This larger unconverted volume fraction of Na-438 in the nominally Na-338 sample arose from the larger volume of powder we used for μSR measurements and likely an incomplete conversion of one of the component batches.

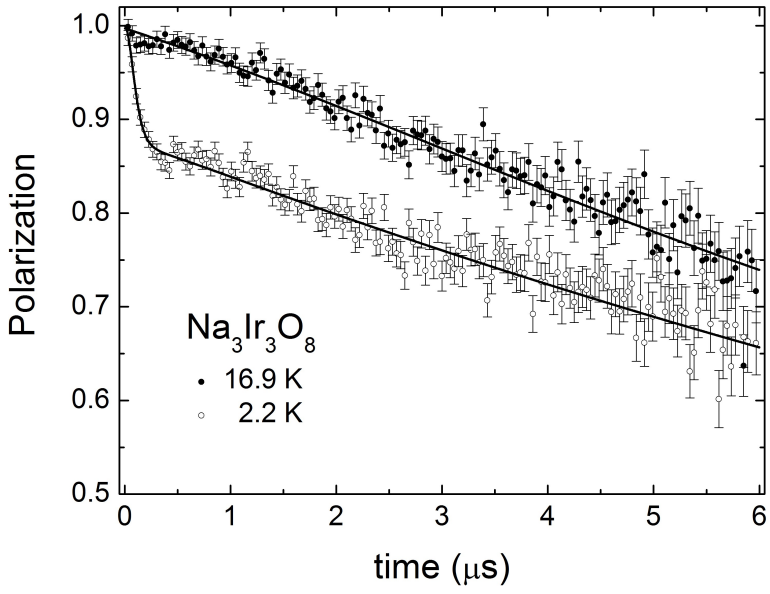

Figure 4.3: Zero-field muon depolarization versus time at two temperatures for Na-338. The solid lines are fitting curves, as described in the text.

The muon relaxation time in the Na-338 volume fraction is found to be nearly con-

stant below 17 K, with $\lambda_{338} \approx 0.06(1)\ \mu s^{-1}$. Although the exponential relaxation is suggestive of dynamical depolarization, longitudinal field studies show that an applied field of 50 G is sufficient to fully suppress relaxation in Na-338 (Fig. 4.4), indicating that the muon depolarization is due to weak static magnetic moments; the depolarization due to the Na-438 volume fraction is essentially unchanged by the applied field. Increasing the longitudinal field to 500 G, however, completely suppresses all relaxation in the sample.

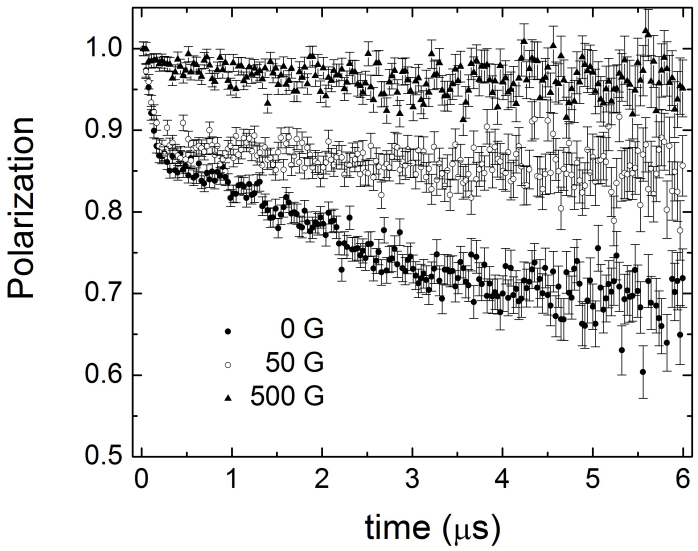

Figure 4.4: Muon depolarization versus time at $T = 1.6$ K in longitudinal magnetic fields for Na-338.

Acknowledgments

This work was supported in part by NSF CAREER award DMR-1056625 (S.D.W.). Muon experiments were performed at the Swiss Muon Source at the Paul Scherrer Institute (Switzerland). This work utilized facilities supported in part under NSF award DMR-0944772 and SQUID measurements were supported in part by grant DMR-1337567.

References

[1] Jackeli, G. & Khaliullin, G. Mott insulators in the strong spin-orbit coupling limit: From heisenberg to a quantum compass and kitaev models. *Phys. Rev. Lett.* **102**, 017205 (2009).

[2] Kimchi, I. & Vishwanath, A. Kitaev-heisenberg models for iridates on the triangular, hyperkagome, kagome, fcc, and pyrochlore lattices. *Phys. Rev. B* **89**, 014414 (2014).

[3] Chen, G. & Balents, L. Spin-orbit effects in $Na_4Ir_3O_8$: A hyper-kagome lattice antiferromagnet. *Phys. Rev. B* **78**, 094403 (2008).

[4] Kitaev, A. Anyons in an exactly solved model and beyond. *Annals of Physics* **321**, 2 – 111 (2006). January Special Issue.

[5] Chaloupka, Jiří and Jackeli, George and Khaliullin, Giniyat. Zigzag Magnetic Order in the Iridium Oxide Na_2IrO_3. *Phys. Rev. Lett.* **110**, 097204 (2013).

[6] Singh, Y. & Gegenwart, P. Antiferromagnetic Mott insulating state in single crystals of the honeycomb lattice material Na_2IrO_3. *Phys. Rev. B* **82**, 064412 (2010).

[7] Okamoto, Y., Nohara, M., Aruga-Katori, H. & Takagi, H. Spin-Liquid State in the $S = 1/2$ Hyperkagome Antiferromagnet $Na_4Ir_3O_8$. *Phys. Rev. Lett.* **99**, 137207 (2007).

[8] Hopkinson, J. M., Isakov, S. V., Kee, H.-Y. & Kim, Y. B. Classical antiferromagnet on a hyperkagome lattice. *Phys. Rev. Lett.* **99**, 037201 (2007).

[9] Singh, Y., Tokiwa, Y., Dong, J. & Gegenwart, P. Spin liquid close to a quantum critical point in $Na_4Ir_3O_8$. *Phys. Rev. B* **88**, 220413 (2013).

[10] Suter, A. & Wojek, B. Musrfit: A Free Platform-Independent Framework for μSR Data Analysis. *Physics Procedia* **30**, 69 – 73 (2012). 12th International Conference on Muon Spin Rotation, Relaxation and Resonance (μSR2011).

[11] Amato, A. Heavy-fermion systems studied by μSR technique. *Rev. Mod. Phys.* **69**, 1119–1180 (1997).

[12] Blundell, S. J. Spin-polarized muons in condensed matter physics. *Contemporary Physics* **40**, 175–192 (1999).

[13] Le Yaouanc, A. A. *Muon spin rotation, relaxation, and resonance : applications to condensed matter*. International series of monographs on physics (Oxford, England) ; 147 (Oxford University Press, Oxford ; New York, 2011).

[14] Noakes, D. R. & Kalvius, G. M. Anomalous zero-field muon spin relaxation in highly disordered magnets. *Phys. Rev. B* **56**, 2352–2355 (1997).

[15] Noakes, D. R. A correlation length measured by zero-field muon spin relaxation in disordered magnets. *Journal of Physics: Condensed Matter* **11**, 1589 (1999).

[16] Hodges, J. A. and Bonville, P. and Forget, A. and Yaouanc, A. and Dalmas de Réotier, P. and André, G. and Rams, M. and Królas, K. and Ritter, C. and Gubbens, P. C. M. and Kaiser, C. T. and King, P. J. C. and Baines, C. First-Order Transition in the Spin Dynamics of Geometrically Frustrated $Yb_2Ti_2O_7$. *Phys. Rev. Lett.* **88**, 077204 (2002).

[17] MacLaughlin, D. E. *et al.* Muon spin rotation and relaxation in $Pr_{1-x}Nd_xOs_4Sb_{12}$: Magnetic and superconducting ground states. *Phys. Rev. B* **89**, 144419 (2014).

[18] Yaouanc, A. and Maisuradze, A. and Dalmas de Réotier, P. Influence of short-range spin correlations on the μSR polarization functions in the slow dynamic limit: Application to the quantum spin-liquid system $Yb_2Ti_2O_7$. *Phys. Rev. B* **87**, 134405 (2013).

[19] Uemura, Y. J. *et al.* Spin Fluctuations in Frustrated Kagomé Lattice System $SrCr_8Ga_4O_{19}$ Studied by Muon Spin Relaxation. *Phys. Rev. Lett.* **73**, 3306–3309 (1994).

[20] MacLaughlin, D. E. *et al.* Unconventional spin freezing and fluctuations in the frustrated antiferromagnet $NiGa_2S_4$. *Phys. Rev. B* **78**, 220403 (2008).

[21] Colman, R. H. *et al.* Spin dynamics in the $S = \frac{1}{2}$ quantum kagome compound vesignieite, $Cu_3Ba(VO_5H)_2$. *Phys. Rev. B* **83**, 180416 (2011).

[22] Zhao, S. *et al.* Magnetic transition, long-range order, and moment fluctuations in the pyrochlore iridate $Eu_2Ir_2O_7$. *Phys. Rev. B* **83**, 180402 (2011).

[23] Disseler, S. M. *et al.* Magnetic order in the pyrochlore iridates $A_2Ir_2O_7$ (A = Y, Yb). *Phys. Rev. B* **86**, 014428 (2012).

[24] Gardner, J. S. *et al.* Cooperative Paramagnetism in the Geometrically Frustrated Pyrochlore Antiferromagnet $Tb_2Ti_2O_7$. *Phys. Rev. Lett.* **82**, 1012–1015 (1999).

[25] Dalmas de Réotier, P. and Yaouanc, A. and Keller, L. and Cervellino, A. and Roessli, B. and Baines, C. and Forget, A. and Vaju, C. and Gubbens, P. C. M. and Amato, A. and King, P. J. C. Spin Dynamics and Magnetic Order in Magnetically Frustrated $Tb_2Sn_2O_7$. *Phys. Rev. Lett.* **96**, 127202 (2006).

Chapter 5

α-$NaMnO_2$ crystal growth

The work presented in this chapter is the result of collaborations and authorship is shared. R. Clément was integral in collecting and analyzing the NMR data for this work. Previous publication of this data and analysis can be found in the *Journal of Crystal Growth*:

> Dally, R., Clément, R. J., Chisnell, R., Taylor, S., Butala, M., Doan-Nguyen, V., Balasubramanian, M., Lynn, J. W., Grey, C. P. and Wilson, S. D. Floating zone growth of α-$Na_{0.90}MnO_2$ single crystals, *J. Cryst. Growth* **459**, 203-208 (2017).

5.1 Introduction

Two-dimensional layered transition metal oxides of the form ABO_2 (A=alkali metal, B=transition metal) have drawn the attention of scientists from a variety of backgrounds due to their wide array of novel electronic and functional properties. For instance, in the realm of novel cathode materials, α-Na_xMnO_2 (α-NMO) with the monoclinic $NaNiO_2$ structure type is widely studied as a potential Na-based cathode platform due to its superior cycling performance and operating potential [1, 2]. At the same time, α-NMO also holds interest for researchers in the area of fundamental condensed matter physics due to its underlying anisotropic triangular lattice of Mn^{3+} moments and its rich electronic phase diagram accessible via deintercalation [3]. While small volume crystals of the α-NMO system have been produced via hydrothermal and sealed crucible techniques [4, 5], high purity floating zone (FZ) growth of large volume crystals has remained elusive. This is primarily due to the challenge of dual Na and Mn volatility during growth as well as two competing polymorphic forms for NMO, namely α-NMO and β-$NaMnO_2$ (β-NMO), with very close energetics [6, 7, 8, 9]. The successful synthesis of large volume FZ grown crystals of the form ABO_2, such as Na_xCoO_2 [10, 11, 12, 13], have historically provided access to deeper experimental insights. The current absence of high purity, large volume FZ crystals of α-NMO presents an impasse to the community's understanding of this system's rich phase behavior, where recent studies have been limited to polycrystalline specimens [3, 7, 14, 15, 16, 17].

α-NMO is composed of alternating layers of two-dimensional manganese oxide and sodium sheets as shown in Fig. 5.1. It crystallizes in the monoclinic $C2/m$ spacegroup

with an $O3$ layering sequence where Na ions occupy octahedrally coordinated sites between the MnO_6 layers. MnO_6 octahedra within these layers form an edge sharing triangular lattice where the Mn^{3+} cations undergo a large, cooperative Jahn-Teller distortion [14]. This results in an anisotropic triangular lattice of manganese cations in the high-spin $S = 2$ state and a (d^4, $t_{2g}^3 e_g^1$) electronic configuration. In contrast, the β polymorph is made up of alternating zigzag-like layers of Na and MO_2 sheets and has orthorhombic symmetry ($Pnmn$ space group). The removal of Na from the α polymorph provides a means of hole doping, which introduces Mn^{4+} cations and locally relaxes the Jahn-Teller distortion in the manganese oxide planes. This can lead to a rich interplay between Na ion/vacancy ordering, charge ordering, magnetic correlations, and Jahn-Teller lattice distortions as the Na-site occupancy is tuned [3]. While studies of this interplay in α-NMO are just beginning, detailed investigations of single crystal specimens are notably lacking. Successful FZ crystal growth was previously harnessed to explore and gain considerable physical insight into the structurally related Na_xCoO_2 system [18], suggesting a similar approach for the crystal growth of α-NMO.

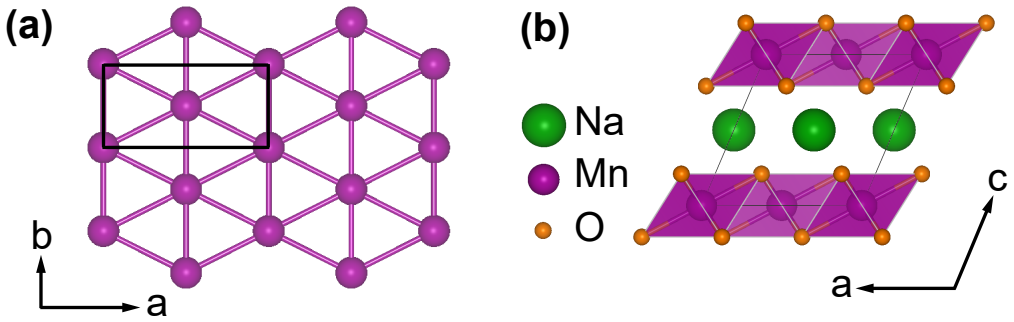

Figure 5.1: The structure of monoclinic α-$NaMnO_2$ is illustrated via projections of the (a) ab-plane and the (b) ac-plane, with the unit cell outlined in black for both figures. Panel (a) shows just a single plane of the manganese cations and panel (b) shows the MnO_6 polyhedra as shaded purple regions, oxygen atoms as orange spheres, and Na atoms as green spheres.

Here we report the FZ growth of single crystals of α-NMO with $x = 0.90$. While α-NMO is prone to disorder from stacking faults (SF) and intergrowths of the competing polymorph β-NMO—both of which originate from the tendency of the structure to twin [6, 7, 8]—by tailoring the crystal growth speed we were able to mitigate this intergrowth contamination. Specifically, ^{23}Na nuclear magnetic resonance (NMR) measurements characterizing the degree of structural faulting demonstrate that the growth rate correlates to the relative phase fractions of α- and β- polymorphs and the number

of stacking faults within the resulting crystals. This fact, along with neutron powder and single crystal diffraction data, show that the optimized, large volume α-NMO crystals are free of both local and long-range β-phase intergrowths with a good quality mosaic. Combined x-ray absorption near edge spectroscopy (XANES), x-ray photoelectron spectroscopy (XPS), and inductively coupled plasma atomic emission spectroscopy (ICP-AES) data determine the stoichiometry of crystals grown under optimal conditions to be $Na_{0.90}MnO_2$. Our work opens the α-NMO system to new avenues of investigation via single crystal studies harnessing a variety of experimental techniques, such as neutron scattering where large volume single crystals are required.

5.2 Experimental Details

5.2.1 Powder Synthesis and Crystal Growth

Starting powders were prepared from Na_2CO_3 and $MnCO_3$ powders (Alfa Aesar, Puratronic 99.997% and 99.985%, respectively). The powders were mixed with a 1:1 molar ratio, plus 10% weight excess of Na_2CO_3 to account for sodium loss during synthesis. The mixed powder was sintered in an alumina crucible at 350 °C for 15 hours, reground and then sintered at 750 °C for 15 hours. The powder was then reground, formed into a rod with a diameter of 5 mm, and pressed at 50,000 psi in an isostatic press. The pressed rod was then sintered in a vertical furnace at 1000 °C for 15 hours and then quenched in air. At this point in the synthesis process, the polycrystalline rod is comprised of a majority of β-NMO. We note here that quenching was used as a preventative measure to avoid decomposition of the rod into mixed phases, and the effect of alternatively slow cooling the sintered feed rod is not explored here. The polycrystalline sintered β-rod was then cut and used as both the feed rod and as a polycrystalline seed for floating zone growth in a four mirror optical floating zone furnace with 500 W halogen lamps (Crystal Systems Corp. Model FZ-T-10000-H-VI-VPO-I-HR-PC). A 4:1 ratio of Ar:O_2 was used to pressurize the chamber to 0.15 MPa in order to help mitigate Na volatility, and gases were flowed through the growth chamber at rates of 80 SCCM and 20 SCCM for Ar and O_2, respectively. Once grown and cooled, crystals were immediately transferred to an Ar-filled glovebox for storage and further analysis.

5.2.2 Inductively coupled plasma atomic emission spectroscopy (ICP-AES)

To determine sodium and manganese concentrations in α-NMO crystals and polycrystalline samples, ICP-AES measurements were performed in a Thermo iCap 6300. Samples for analysis were prepared by first massing the starting materials on a 0.01 mg resolution balance and then dissolving the crystals in concentrated trace metals grade hydrochloric acid (High-Purity Standards). Heat was applied via a hot water bath over a hotplate to the samples in a closed container containing HCl until no particulates could be seen and the solution became clear. This reduced the room temperature dissolution time in HCl from 4-10 days to only 1-3 hours. Upon cooling, the dissolved sodium manganese oxide was diluted with deionized water to obtain a 5% HCl matrix. Instrument calibrations for Na and Mn were done using blank, low, and high PPM solutions within a 5% HCl matrix, which were prepared using standard analysis grade solutions of Na (1000 μg/mL in 1% HCl) and Mn (1000 μg/mL in 2% HCl) from High-Purity Standards.

5.2.3 ^{23}Na solid-state NMR (ssNMR)

^{23}Na ssNMR spectra were acquired at room temperature on a Bruker Advance III 200 wide-bore spectrometer (4.7 T external magnetic field) at a Larmor frequency of -53.0 MHz. All NMR experiments were performed under 60 kHz magic angle spinning (MAS) using a 1.3 mm double-resonance HX probe and a recycle delay of 30 ms. ^{23}Na NMR data were acquired on finely ground samples of single crystal NMO. ^{23}Na NMR chemical shifts were referenced against solid ^{23}NaCl at 7.21 ppm. ^{23}Na spin echo NMR spectra were acquired using a 90° radiofrequency (RF) pulse of 1.03 μs and a 180° RF pulse of 2.06 μs at 25.04 W. Transverse (T_2') relaxation times were obtained from an exponential fit of the decay of the signal intensity obtained as the echo delay was increased in an NMR spin echo pulse sequence.

5.2.4 X-Ray Absorption Near Edge Spectroscopy (XANES)

XANES data were taken at beamline 20-BM-B at the Advanced Photon Source at Argonne National Laboratory with an incident energy tuned to the Mn K-edge. Single crystals of NMO were finely ground and a thin, uniform layer of powder was sealed be-

tween pieces of kapton tape under an inert environment. The standards used, $LiMn_2O_4$ and Mn_2O_3, were prepared in a similar manner. Data were deglitched, calibrated, and normalized using the software Athena [19]. Mn foil was used as a reference, and a simultaneous spectrum of the foil was collected in transmission mode during each run of the sample and standards. Calibrations to each data set were made by matching the absorption edge of the Mn foil to 6539 eV and then shifting the data set by that amount [20].

5.2.5 X-ray photoelectron spectroscopy (XPS)

Data were taken using a Kratos Axis Ultra X-ray Photoelectron Spectroscopy system with a pass energy of 40 eV and step size of 0.1 eV. Data were analyzed using the splitting of the Mn 3s peak, which is a result of the exchange coupling between 3s holes and 3d electrons. The NMO spectrum was corrected using a Shirley background and peaks were fit to a Gaussian-Lorentzian line shape.

5.2.6 Neutron diffraction measurements

Neutron powder diffraction data were collected using the BT-1 neutron powder diffractometer at the NIST Center for Neutron Research (NCNR). A Cu(311) monochromator with a 90° take-off angle, $\lambda = 1.5397(2)$ Å, and in-pile collimation of 60′ were used. Data were collected over the 2θ range of 3-168° with a step size of 0.05°. About 3 g of crystal from a single growth run was ground and sealed in a vanadium container of length 50 mm and diameter 9.2 mm inside a dry He-filled glovebox. A fit to the data was calculated using the Le Bail refinement [21] option in FullProf [22].

The triple-axis instrument BT-7 [23] at NCNR was used to demonstrate the mosaic of the typical crystals using a vertically focused PG(002) monochromator and an incident energy of 14.7 meV. A single crystal of ∼0.5 g was aligned in the HK0 plane using open–25′–25′–120′ collimators placed before the monochromator, before the sample, after the sample, and before the detector, respectively. Uncertainties where indicated represent one standard deviation.

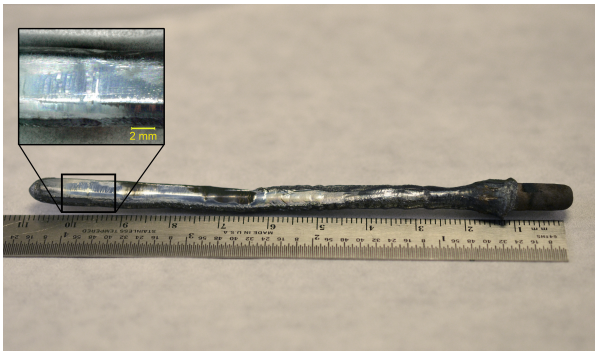

Figure 5.2: As grown α-$Na_{0.90}MnO_2$ crystal. Stable crystal growth begins after ≈4 cm of translation, where there is a visible change in shape. The inset shows a close-up of the flat (-101) facet that was formed during stable growth.

5.3 Results and Discussion

A number of varying growth speeds and translation rates were attempted with key results summarized in Table 5.1. The optimal growth conditions for phase pure α-NMO were found to be a 20 mm/hr mirror translation rate, 2 mm/hr feed rod translation rate, 30 rpm seed rod rotation, and 20 rpm feed rod rotation. Under these conditions, attempts to seed from a previously grown α-NMO crystal were unsuccessful, likely due to substantial decomposition (*i.e.* Na loss) of the seed crystal during the initial heating process. However, seeding from a polycrystalline rod was able to repeatedly nucleate a single grain crystal after ≈4 cm of growth. Facets form readily after the start of growth leading to the formation of a single domain within 4 cm, negating the need for a seed crystal. Specifically, a stable molten zone which leads to α-phase growth with minimal stacking faults (the determination of which is discussed later) was achieved by starting mirror translation at 50 mm/hr from the initial polycrystalline seed and then stepping it down gradually toward 20 mm/hr, where steady state growth was performed. We note that our attempts at seeding growth at this eventual lower growth rate failed to maintain a stable molten zone. This is illustrated in Fig. 5.2, where the boule's cross section becomes more elliptical in shape with flat facets forming perpendicular to the direction of seed translation at the point where a stable molten zone was achieved at 20 mm/hr. These perpendicular facets are oriented along the (-101) lattice plane, and the crystal growth direction is along the short b-axis. Substantial evaporation of both Na and Mn occurred during FZ growth, and depositions composed of a mixture of Na and Mn oxides built up on the inner quartz walls of the growth chamber. We found it

necessary to increase the power of the lamps slightly over the course of growth (≈1-2%) to compensate for the decreasing transparency of the tube.

ICP-AES analysis of samples grown at a rate of 20 mm/hr indicated a Na:Mn ratio of 0.90:1. We note here that the absolute values of the measured Na and Mn content in our samples also matched the reported ratios (*i.e.* the measured Mn content was stoichiometric within experimental error), and that various sections of the rod were tested to check for consistency. The portions of the crystals grown under the stepped down growth rates showed uniform Na content across each crystal. The results are summarized as Na:Mn ratios in Table 5.1 for a series of representative samples as well as the starting polycrystalline feed rod. As a further step, the relative fraction of Mn^{3+} versus Mn^{4+} was probed via XANES measurements, which when combined with ICP-AES results are capable of resolving substantial oxygen non-stoichiometry. XANES data (Fig. 5.3 (a)) on a 20 mm/hr grown crystal show the white-line peak position close to that of the Mn_2O_3 standard with an oxidation state of Mn^{3+}. There is, however, a resolvable shift of the NMO spectrum toward the $LiMn_2O_4$ standard with an average valence of $Mn^{3.5+}$, consistent with the known Na deficiency of the sample.

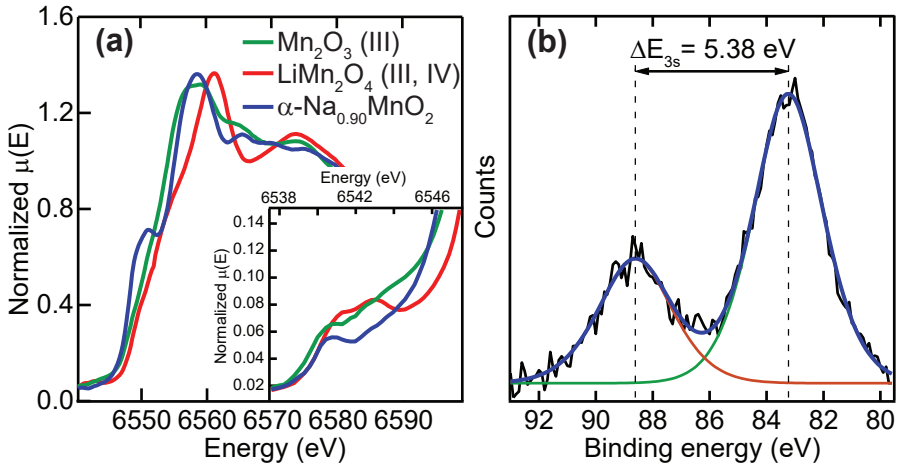

Figure 5.3: (a) XANES data show the spectra collected for a 20 mm/hr grown α-$Na_{0.90}MnO_2$ sample and standards at the Mn K-edge, and the inset details the pre-edge region of the spectra. (b) XPS data collected on a α-$Na_{0.90}MnO_2$ sample showing the multiplet splitting of the Mn 3s peak, which exhibits a $\Delta E = 5.38$ eV, corresponding to an average valence of $Mn^{3.07+}$.

The pre-edge region of the XANES spectra is associated with transitions from the 1s states to the split t_{2g} and e_g d-orbitals, resulting in varying peak shapes for Mn^{4+} and Mn^{3+} cations in varying local environments [24]. A double peak structure in this energy range is conventionally indicative of Mn^{4+}, and a single broad peak is associated

Sample	Na:Mn (molar ratio)	α/SF/β (%)	Growth Rate	Atmosphere	Pressure
starting powders	1:1 + 10 wt% excess Na_2CO_3	–	n/a	n/a	n/a
β-rod	1.04:1	6 / 37 / 57	n/a	ambient	ambient
crystal 1	0.90:1	96 / 4 / <1	20 mm/hr	4:1 Ar/O_2	0.15 MPa
crystal 2	0.94:1	15 / 19 / 66	50 mm/hr	4:1 Ar/O_2	0.15 MPa
crystal 3	0.75:1	–	20 mm/hr	1:1 Ar/O_2	0.15 MPa

Table 5.1: Summary of growth trials using varying crystal pull rates and growth environments. Compositional analyses of crystals grown under each condition as well as the polycrystalline feed material are also summarized.

with Jahn-Teller distorted MnO_6 octahedra [25, 26]. The double peak is resolvable in the $Mn^{3.5+}$ $LiMn_2O_4$ standard as shown in the inset of Fig. 5.3 (a), but is not in the α-NMO sample, again, indicating the majority of manganese in the sample is Mn^{3+}. We therefore performed XPS measurements in order to gain a more quantitative understanding of the manganese valence state. There exists a linear relationship between the manganese oxidation state and the exchange splitting of the Mn $3s$ peak, ΔE_{3s} where $V_{Mn} = 7.875 - 0.893\Delta E_{3s}$ [27, 28]. Using this relation to evaluate the Mn valence for a typical α-$Na_xMnO_{2\pm\delta}$ crystal grown at 20 mm/hr, the data shown Fig. 5.3 (b) reveal $\Delta E_{3s} = 5.38$ eV, which corresponds to an average Mn valence of $+3.07 \pm 0.04$. The combined XPS and ICP-AES analysis of optimal α-phase crystals determines the oxygen to be stoichiometric within error.

The lattice structure of α-NMO crystals was verified by cutting a crystal from the end of the growth boule, crushing the crystal into powder, and then performing neutron powder diffraction. Neutron powder data collected at 300 K are shown in Fig. 5.4 (a) and can be fully indexed to the reported α-NMO space group, $C2/m$, with Le Bail refined lattice parameters $a = 5.6672$ Å $\pm$ 0.0003 Å, $b = 2.8606$ Å $\pm$ 0.0001 Å, $c = 5.8007$ Å $\pm$ 0.0003 Å, and $\beta = 113.143° \pm 0.003°$. Separate single crystal neutron diffraction measurements on a crystal observed only a single grain with an observed full-with-at-half-maximum (FWHM) of $0.41° \pm 0.01°$ as plotted in Fig. 5.4 (b), which after correction for the instrumental resolution indicates a mosaic spread of 0.35°. Together these measurements establish the *long-range* ordered lattice structure of crystals grown under optimal conditions to phase pure α-NMO single crystals; however, they are not directly sensitive to *local* intergrowths of β-NMO which may arise as a series of stacking faults within the $O3$ layered structure.

To investigate the presence of local intergrowths of β-NMO and stacking faults within the lattice of α-NMO crystals, ^{23}Na solid-state NMR (ssNMR) data were collected with results plotted in Fig. 5.5. If a number of ^{23}Na resonant frequencies are resolved in the NMR spectra collected on crushed α-NMO crystals, it suggests the presence of multiple chemical environments reflective of the formation of stacking faults (twin planes) between nanodomains of the α and β polymorphs of NMO. While structural intergrowths and the formation of stacking faults between the α- and β-polymorphs

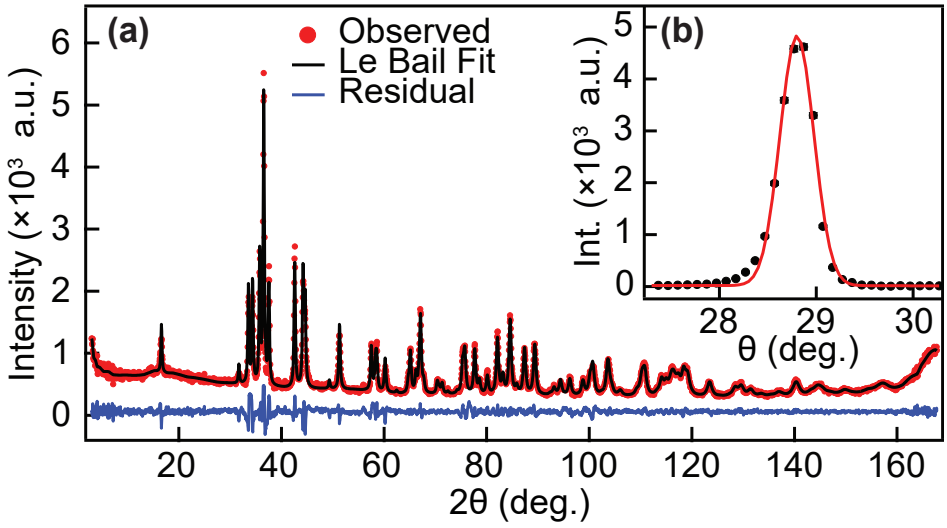

Figure 5.4: (a) Neutron powder diffraction data and corresponding Le Bail refinement for a crushed single crystal of α-$Na_{0.90}MnO_2$ (b) Bulk averaged mosaic of a crystal shown through the rocking curve collected at the (200) nuclear Bragg peak of a typical crystal of α-$Na_{0.90}MnO_2$. Solid line shows a Gaussian fit to the peak of the form $I \propto exp(-\frac{1}{2}(\frac{x-x_0}{w})^2)$ and where the $FWHM = 2w\sqrt{2ln(2)}$ defines the mosaic, which after taking into account the instrumental resolution defines the intrinsic mosaic spread of the crystal.

of NMO have been reported previously [6, 7, 8], quantifying their relative abundance across a macroscopic sample presents a challenge. Recently, a ^{23}Na NMR study of β-NMO identified three resonances with isotropic shifts of ca. 750, 530 and 320 ppm and assigned them to Na nuclei in α-NMO domains, in β-NMO domains, and Na atoms in the direct vicinity of localized stacking faults, respectively [8]. This assignment was confirmed by recent first principles calculations of Na NMR parameters in various NMO structures containing twin planes between α- and β-type structural domains [9]. In the present work, we use these assignments to quantify the proportion of Na nuclei in these three different regions within our FZ grown NMO crystals.

Relative fractions of Na site occupations were determined by integration of spin echo spectra shown in Fig. 5.5, and contributions from individual Na sites were scaled by a transverse relaxation factor accounting for the loss of NMR signal intensity over the signal acquisition time. Fig. 5.5 (b) was collected on a crystal grown at 20 mm/hr and indicates the dominance of a single Na crystallographic environment where ca. 96% of Na in the sample resides in an α-NMO environment with a small percentage (ca. 4%) of Na near stacking faults. A nearly negligible fraction ($< 1\%$) of Na in β-like environments indicates local β-NMO regions. This demonstrates that the lattice structure of crystals

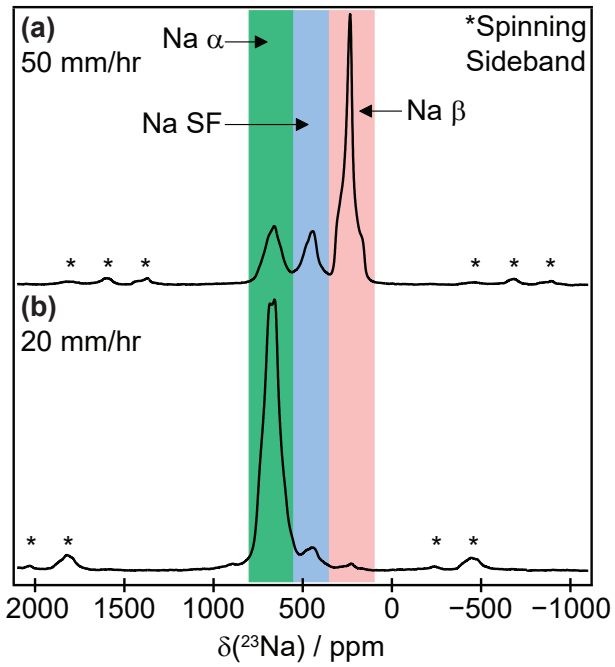

Figure 5.5: ^{23}Na ssNMR spectra obtained at room temperature at 4.7 T on two samples of single crystal NMO grown at different rates. The peaks corresponding to Na nuclei in α-NaMnO$_2$ domains (Na α), in β-NaMnO$_2$ domains (Na β), and in the vicinity of a stacking fault (Na SF), are shown on the figure. Spinning sidebands due to fast sample rotation are indicated by (*).

grown at the lowest rate of 20 mm/hr is largely free of faulting and that the local structure is consistent with the long-range α-NMO crystal structure determined via neutron diffraction. The fraction of Na^+ ions in an α-like environment can be further broken down into Na^+ ions close to a Mn^{4+} ion (ca. 6% of all Na) and into Na^+ ions surrounded by Mn^{3+} ions only (ca. 90% of all Na). The former environment is indicated by a Na resonance at 950 ppm (see small peak on the left of the alpha peak in Fig. 5.5 (b)) which determines the proportion of Mn^{4+} ions/Na vacancies to be in relatively good agreement with the total Na content obtained with XPS/ICP-AES. At this time, control over the sodium content is limited to $x = 0.90$ for quality, phase-pure samples.

Having established that phase pure α-NMO single crystals can be grown via FZ, one further question explored was the degree through which the NMO polymorphs can be selected via the crystal growth rate. While the β-phase of NMO is nominally the higher temperature structure [1, 2, 29], β-NMO is known to persist at ambient conditions through quenching the system into a metastable state [1, 7, 8]. As a result, an increased crystal pull rate can potentially be harnessed to increase the relative phase fraction of β-NMO within Na_xMnO_2 crystals. To investigate this, crystals were grown under

identical conditions as the optimal α-$Na_{0.90}MnO_2$ crystals discussed previously with the exception of an increase in the sustained mirror translation rate to 50 mm/hr. The ^{23}Na ssNMR spectrum collected on crystals grown under this increased rate is plotted in Fig. 5.5 (a) and is dominated by the characteristic signal from Na ions in β-NMO type local environments; specifically, the majority phase fraction of the more rapidly grown sample is 66% β-NMO, which far exceeds the relative fractions of 15% α-NMO and 19% of Na near locally faulted regions. This demonstrates that the dominant growth mode has switched to the metastable β-NMO polymorph. We note that this local phase mixture between α-NMO, β-NMO, and faulted regions is consistent with the composition of powders whose long-range lattice structure is β-NMO—a lattice known to be highly defect prone [8, 9] and intermixed with regions of the competing α-phase. Due to the defect prone lattice of β-NMO, it is currently unclear whether even higher growth rates (>50 mm/hr) would result in more locally phase pure β-NMO crystals.

5.4 Conclusions

Floating zone crystal growth in an optical image furnace was utilized to produce large volume, single crystals of α-phase Na_xMnO_2 with minimal stacking faults. ICP-AES, XANES, and XPS measurements determined that crystals grown via the parameters reported here possess a 10% Na deficiency and a final stoichiometry of $Na_{0.90}MnO_2$. Further characterization of crystals grown at slower growth rates via combined neutron diffraction and ssNMR studies determined both the long-range and local structure of these crystals to be single-phase α-NMO. By varying the crystal growth rate (*i.e.* the mirror translation rate), the mixture of polymorphs present in $Na_{0.90}MnO_2$ crystals can be selected/tuned—a finding of potential interest for the creation of tailored cathode materials with a tunable intermixture of α- and β- phases. Furthermore, the large volume growth of high purity α-NMO crystals opens the compound to detailed exploration via a new array of probes such as single crystal neutron scattering and single crystal muon spin relaxation.

Acknowledgements

SDW gratefully acknowledges support from the Hellman Foundation, and SDW and RD acknowledge support from ARO Award W911NF-16-1-0361. VDN is supported by the University of California President's Postdoctoral Fellowship and the University of California, Santa Barbara California NanoSystems Institute Elings Prize Fellowship. This work was partially supported by the Assistant Secretary for Energy Efficiency and Renewable Energy, Office of Vehicle Technologies of the U.S. Department of Energy under Contract No. DE-AC02-05CH11231, under the Batteries for Advanced Transportation Technologies (BATT) Program subcontract No. 7057154 (RJC and CPG). CPG and RJC thank the EU ERC for an Advanced Fellowship for CPG. The MRL Shared Experimental Facilities are supported by the MRSEC Program of the NSF under Award No. DMR 1121053; a member of the NSF-funded Materials Research Facilities Network (www.mrfn.org). This research used resources of the Advanced Photon Source, a U.S. Department of Energy (DOE) Office of Science User Facility operated for the DOE Office of Science by Argonne National Laboratory under Contract No. DE-AC02-06CH11357. Sector 20 operations are supported by the US Department of Energy and the Canadian Light Source. The identification of any commercial product or trade name does not imply endorsement or recommendation by the National Institute of Standards and Technology.

References

[1] Ma, X., Chen, H. & Ceder, G. Electrochemical Properties of Monoclinic $NaMnO_2$. *Journal of The Electrochemical Society* **158**, A1307–A1312 (2011).

[2] Mendiboure, A., Delmas, C. & Hagenmuller, P. Electrochemical intercalation and deintercalation of Na_xMnO_2 bronzes. *Journal of Solid State Chemistry* **57**, 323 – 331 (1985).

[3] Li, X. *et al.* Direct visualization of the Jahn-Teller effect coupled to Na ordering in $Na_{5/8}MnO_2$. *Nature Materials* **13**, 586–92 (2014).

[4] Hirano, S.-I., Narita, R. & Naka, S. Hydrothermal synthesis and properties of Na_xMnO_2 crystals. *Journal of Crystal Growth* **54**, 595–599 (1981).

[5] Jansen, M. & Hoppe, R. Zur Kenntnis der NaCl-Strukturfamilie Die Kristallstruktur von $NaMnO_2$. *Zeitschrift für anorganische und allgemeine Chemie* **399**, 163–169 (1973).

[6] Clément, R. J., Bruce, P. G. & Grey, C. P. Review—Manganese-Based P2-Type Transition Metal Oxides as Sodium-Ion Battery Cathode Materials. *Journal of The Electrochemical Society* **162**, A2589–A2604 (2015).

[7] Abakumov, A. M., Tsirlin, A. A., Bakaimi, I., Tendeloo, G. V. & Lappas, A. Multiple Twinning As a Structure Directing Mechanism in Layered Rock-Salt-Type Oxides: $NaMnO_2$ Polymorphism, Redox Potentials, and Magnetism. *Chemistry of Materials* **26**, 3306–3315 (2014).

[8] Billaud, J. *et al.* β-$NaMnO_2$: A High-Performance Cathode for Sodium-Ion Batteries. *Journal of the American Chemical Society* **136**, 17243–17248 (2014). PMID: 25397400.

[9] Clément, R. J., Middlemiss, D. S., Seymour, I. D., Ilott, A. J. & Grey, C. P. Insights into the Nature and Evolution upon Electrochemical Cycling of Planar Defects in the β-$NaMnO_2$ Na-Ion Battery Cathode: An NMR and First-Principles Density Functional Theory Approach. *Chemistry of Materials* **28**, 8228–8239 (2016).

[10] Prabhakaran, D., Boothroyd, A., Coldea, R. & Charnley, N. Crystal growth of Na_xCoO_2 under different atmospheres. *Journal of Crystal Growth* **271(1-2)**, 74 – 80 (2004). Publisher: Elsevier Science.

[11] Chen, D. P. *et al.* Single-crystal growth and investigation of Na_xCoO_2 and $Na_xCoO_2{\cdot}yH_2O$. *Phys. Rev. B* **70**, 024506 (2004).

[12] C. Sekar and S. Paulraj and P. Kanchana and B. Schüpp-Niewa and R. Klingeler and G. Krabbes and B. Büchner. Effect of rotation of feed and seed rods on

the quality of $Na_{0.75}CoO_2$ single crystal grown by traveling solvent floating zone method. *Materials Research Bulletin* **46**, 675 – 681 (2011).

[13] Lin, C., Chen, D., Peng, J. & Zhang, P. Growth and characterization of high quality single crystals of Na_xCoO_2. *Physica C: Superconductivity and its Applications* **460-62, Part 1**, 471 – 472 (2007).

[14] Giot, M. *et al.* Magnetoelastic Coupling and Symmetry Breaking in the Frustrated Antiferromagnet α-$NaMnO_2$. *Phys. Rev. Lett.* **99**, 247211 (2007).

[15] Zorko, A. *et al.* Magnetic interactions in α-$NaMnO_2$: Quantum spin-2 system on a spatially anisotropic two-dimensional triangular lattice. *Physical Review B - Condensed Matter and Materials Physics* **77**, 1–7 (2008).

[16] Zorko, A., Adamopoulos, O., Komelj, M., Arčon, D. & Lappas, A. Frustration-induced nanometre-scale inhomogeneity in a triangular antiferromagnet. *Nature Communications* **5**, 3222 (2014).

[17] Stock, C. *et al.* One-Dimensional Magnetic Fluctuations in the Spin-2 Triangular Lattice α-$NaMnO_2$. *Phys. Rev. Lett.* **103**, 077202 (2009).

[18] Boothroyd, A. T. *et al.* Ferromagnetic In-Plane Spin Fluctuations in Na_xCoO_2 Observed by Neutron Inelastic Scattering. *Phys. Rev. Lett.* **92**, 197201 (2004).

[19] Ravel, B. & Newville, M. ATHENA, ARTEMIS, HEPHAESTUS: data analysis for X-ray absorption spectroscopy using IFEFFIT. *Journal of Synchrotron Radiation* **12**, 537–541 (2005).

[20] Kraft, S. and Stümpel, J. and Becker, P. and Kuetgens, U. High resolution x-ray absorption spectroscopy with absolute energy calibration for the determination of absorption edge energies. *Review of Scientific Instruments* **67**, 681–687 (1996).

[21] Bail, A. L., Duroy, H. & Fourquet, J. Ab-initio structure determination of $LiSbWO_6$ by X-ray powder diffraction. *Materials Research Bulletin* **23**, 447 – 452 (1988).

[22] Rodriguez-Carvajal, J. FullProf: A Program for Rietveld Refinement and Profile Matching Analysis of Complex Powder Diffraction Patterns (ILL, unpublished) .

[23] Lynn, J. *et al.* Double focusing thermal triple axis spectrometer at the NCNR. *J. Research of the National Institute of Standards and Technology* **117**, 61–79 (2012).

[24] Chalmin, E., Farges, F. & Brown, G. E. A pre-edge analysis of Mn K-edge XANES spectra to help determine the speciation of manganese in minerals and glasses. *Contributions to Mineralogy and Petrology* **157**, 111–126 (2009).

[25] Sassin, M. B. *et al.* Achieving electrochemical capacitor functionality from nanoscale $LiMn_2O_4$ coatings on 3-D carbon nanoarchitectures. *J. Mater. Chem. A* **1**, 2431–2440 (2013).

[26] Kwon, O.-S., Kim, M.-S. & Kim, K.-B. A study on the effect of lithium insertion-extraction on the local structure of lithium manganese oxides using X-ray absorption spectroscopy. *Journal of Power Sources* **81-82**, 510 – 516 (1999).

[27] Song, J. *et al.* A Sodium Manganese Oxide Cathode by Facile Reduction for Sodium Batteries. *Chemistry–An Asian Journal* **9**, 1550–1556 (2014).

[28] Li, J.-Y. *et al.* Romanechite-structured $Na_{0.31}MnO_{1.9}$ nanofibers as high-performance cathode material for a sodium-ion battery. *Chem. Commun.* **51**, 14848–14851 (2015).

[29] Velikokhatnyi, O. I., Chang, C.-C. & Kumta, P. N. Phase Stability and Electronic Structure of $NaMnO_2$. *Journal of The Electrochemical Society* **150**, A1262–A1266 (2003).

Chapter 6

Magnetic phases and the ground state in α-$NaMnO_2$

6.1 Introduction

Two-dimensional triangular lattice antiferromagnets are a classic example of geometrically frustrated spins, and by reducing the degeneracy of this model, one can reach the spatially anisotropic triangular lattice, which presents a different playground for exploring frustrated magnetism. The anisotropic triangular lattice can be viewed as interconnected isosceles triangles with two long legs, and one short leg, forming chains of nearest-neighbors. Each atom has four next-nearest neighbors, which frustrates antiferromagnetic ordering. The relative strength of exchange interactions between nearest neighbors (J_1) to that of next-nearest neighbors (J_2) (and any additional relevant exchange interactions) determines the dimensionality of the system or whether it will even order. In the $S = 1/2$ case, spin liquid [1], collinear antiferromagnetic and dimer orders [2] were all predicted depending on the extent of the anisotropy. The $S = 1$ case is intriguing because as $J_2 \to 0$, the system is driven closer to isolated antiferromagnetic spin chains where the ground state is a Haldane gap. For $0.7 \lesssim J_2/J_1 \lesssim 1$, the ground state remains that of the isotropic triangular lattice (120° spiral spin state) [3], and for lesser values of J_2/J_1, Néel and helical order were found to stabilize [4]. Parameters such as spin-orbit effects or Dzyaloshinskii-Moriya interactions can additionally tune the system into different regions of phase space.

In this chapter, time-of-flight neutron scattering, triple-axis neutron diffraction, and magnetic susceptibility using single crystals, along with neutron powder diffraction are employed to probe the different temperature regimes which are spanned by magnetic correlations in α-$NaMnO_2$. The data show that a simple transition from paramagnetism to collinear antiferromagnetic order in α-$NaMnO_2$ is complicated by the combination of geometric frustration, competing exchange interactions, single-ion anisotropy and strong spin-lattice coupling. In fact, three distinct regions of magnetic order are observed: (1) $T > T_{N1}$, where the magnetic anisotropy between intrachain versus interchain versus interplane correlations is first seen, (2) $T_{N2} < T < T_{N1}$, where the coexistance of short-range modulated and short-range collinear magnetic order is observed, and (3) $T < T_{N2}$, where the collinear, quasi long-range ordered ground state is established. As evidenced by the short correlation lengths, α-$NaMnO_2$ remains in the quasi-long range ordered state down to the lowest temperatures probed ($T = 5$ K).

6.2 Stacking faults, twinning, polymorphism and magnetic domains

The ABO_2 delafossite-like compound, α-$NaMnO_2$, crystallizes in the monoclinic $C2/m$ space group. Mn^{3+} atoms decorate a spatially anisotropic triangular lattice, where nearest neighbor Mn atoms form chains along the b-axis. The Mn atoms are octahedrally coordinated with oxygens, forming MnO_6 edge-sharing sheets within the ab-plane. The MnO_6 layers alternate with octahedrally coordinated Na layers along the c-axis, forming a distorted $O3$ ($O3'$) stacking structure. MnO_6 octahedra are coherently Jahn-Teller distorted along the $[-1, 0, 1]$ crystallographic direction, which is the reason for the deviation from an isotropic triangular arrangement of the B-site cation typical of delafossite compounds, which tend to crystallize in the $R\bar{3}m$ space group. Also due to the distortion, is the tendency for the structure to develop stacking faults, twinning, and intergrowth of the β-phase polymorph [5, 6, 7], with details in Appendix B. Oxygen atoms at twin and stacking fault boundaries–where the β-phase polymorph can be viewed as the densest possible arrangement of stacking faults–need not shift to accommodate the defect, consequently costing little energy.

The electron configuration of the octahedrally coordinated Mn^{3+} ions stabilizes the high-spin state, leading to $S = 2$ moments. The spin-orbit interaction is such that the energy minimized when the moment lies along the d_z^2 orbital, which is also aligned with the apical oxygens in the Jahn-Teller distorted octahedra. This single-ion anisotropy effect favors a collinear ground state in α-$NaMnO_2$, which, coupled with the antiferromagnetic exchange between the nearest neighbor and next-nearest neighbor Mn atoms within the ab-plane, leads to $\mathbf{k}_1 = (\frac{1}{2}, \frac{1}{2}, 0)$ ordering. There is a second vector of the star allowed via symmetry, leading to another k-domain, $\mathbf{k}_2 = (-\frac{1}{2}, \frac{1}{2}, 0)$; the two crystallographic twins and two magnetic domains lead to a four domain model, which needs to be noted when analyzing regions of reciprocal space [8]. The single crystals used throughout this study were synthesized using the floating zone method, with details of the procedure and characterization found in Ch. 5. The samples were shown, via NMR, to have a minimal amount of β-phase polymorph ($< 1\%$), a low percentage of stacking faults (4%), and $\approx 6\%$ of Na ions were in the vicinity of a Mn^{4+} cation.

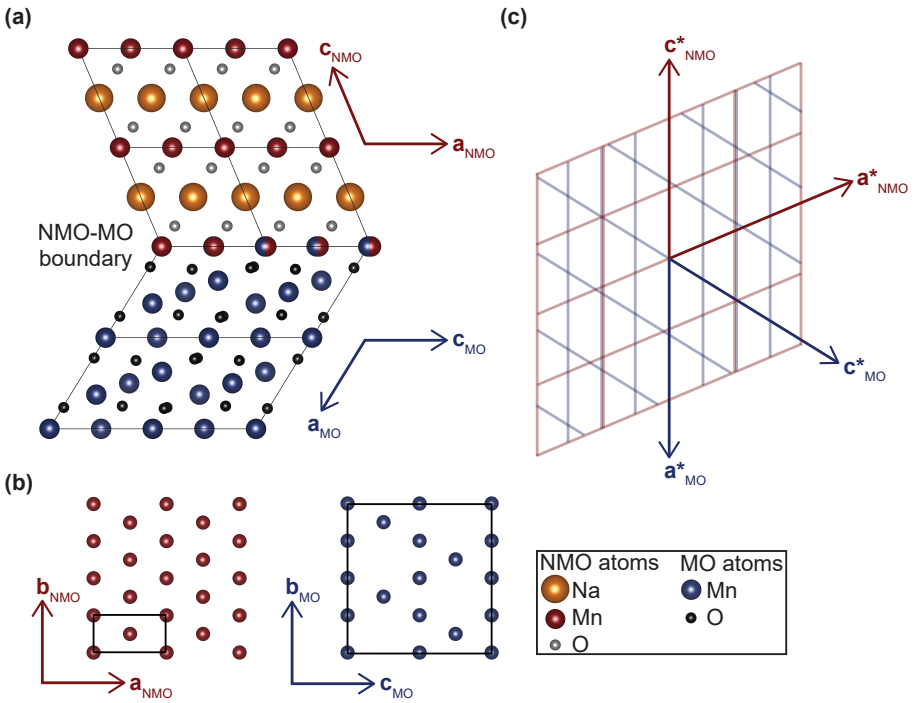

Figure 6.1: Schematic of the Mn_3O_4 (MO) intergrowth with α-$NaMnO_2$ (NMO). (a) The ac-plane of both phases shown meeting at the boundary of intergrowth. (b) Comparison of the ab-plane of α-$NaMnO_2$ with the bc-plane of Mn_3O_4. (c) The reciprocal space a^*c^*-plane for both Mn_3O_4 and α-$NaMnO_2$. The b^*-axis is going into the page for both phases. The reciprocal space vectors are oriented such that they reflect the intergrowth in direct space. The intersection of blue lines represents integer miller index positions for Mn_3O_4 and the intersection of red lines represents integer miller index positions for α-$NaMnO_2$.

6.3 Mn_3O_4 intergrowth

An additional minority phase was found intergrown with α-$NaMnO_2$. It is suspected that during floating zone growth, Na-deficient regions of the melt were able to form Mn_3O_4, as the conditions for this phase sans Na are ideal [9]. The boundary between regions of α-$NaMnO_2$ and Mn_3O_4 is reminiscent of the way in which twin boundaries and stacking faults are formed, as previously discussed. Fig. 6.1 (a) shows this boundary, and it can be seen that the elongated direction of the Jahn-Teller distortions in both the α-$NaMnO_2$ and Mn_3O_4 are continuous across the meeting point of the two structures, and the oxygen atoms do not have to move to accommodate the change in phase.[1] The discussion of Mn_3O_4 in this manuscript will be focused on it's magnetic contributions, thus the magnetic unit cell with monoclinic space group $P2_1/c$ is being used to also describe the room temperature structure.

[1]It should be noted that in the time-of-flight experiments, the orientation of Mn_3O_4 intergrowth was confirmed by being able to index all nuclear and magnetic Bragg peaks that were not coming from α-$NaMnO_2$ or the very small phase fraction of β-$NaMnO_2$.

Analysis of bulk magnetization measurements was used to approximate the amount of Mn_3O_4 intergrowth in a typical sample. The collinear antiferromagnetic ground state of α-$NaMnO_2$ should not exhibit any magnetic hysteresis or coercivity as was confirmed in previous studies [10, 11], and any observation of such can be assumed to come from Mn_3O_4. Magnetization measurements were taken using a Quantum Design PPMS Vibrating Sample Magnetometer (VSM). Two orientations of the crystal with respect to the field were used in data collection. The first, $\mathbf{H} \parallel [0,1,0]$ of α-$NaMnO_2$, used a 21.47 mg crystal and the second, $\mathbf{H} \parallel [\bar{1},0,1]$ of α-$NaMnO_2$, used 7.61 mg from the same sample. Data were not normalized to emu mol^{-1} or μ_B Mn^{-1}, as is usually the case, due to the presence of Mn_3O_4. The spontaneous magnetization in Mn_3O_4 single crystals in the ground state was shown to be 1.89 μ_B per Mn_3O_4 from neutron diffraction experiments [12]. However, magnetization measurements show a reduced spontaneous magnetization, with varying reports on the values [13, 14, 15]. Ref. [16] studied the Mn_3O_4 magnetization of single crystals with the field parallel to the easy-axis (the [1, 1, 0] direction in their report, and the [0, 1, 0] direction here), which is an orientation we can study, so we choose to use their value of 1.7 μ_B per Mn_3O_4 at $H = 5$ T. We note that in our data, we are able to reach fields of 9 T, and that other studies have shown the spontaneous magnetization to reach higher values in even higher fields [14, 15]. By using 1.7 μ_B, the analysis described is potentially underestimating the spontaneous magnetization, which may slightly overestimate the amount of Mn_3O_4 intergrown. Thus, we are putting an upper limit on the amount of intergrowth in our samples. Fig. 6.2 shows data taken in the configuration where $\mathbf{H} \parallel [0,1,0]$. This is both along the b-axis of Mn_3O_4 and α-$NaMnO_2$, and is the easy-axis for Mn_3O_4. At $H = 9$ T, the contribution from the Mn_3O_4 should be almost constant, and that from the α-$NaMnO_2$ should be a sloped line. A line was fit (shown as the dashed orange line in Fig. 6.2) between $H = 8.5$ T and $H = 9$ T. The fitted slope was used to subtract a line with an m-axis intercept of zero as expected for a collinear antiferromagnet. The resulting value of m at $H = 9$ T was taken to be the contribution from the Mn_3O_4 and the mass percentage of the intergrowth was determined to be $\approx$6%.

Careful consideration of the Mn_3O_4 intergrowth's contribution to scattering had to be made during triple-axis neutron experiments. First, to ensure we knew where in

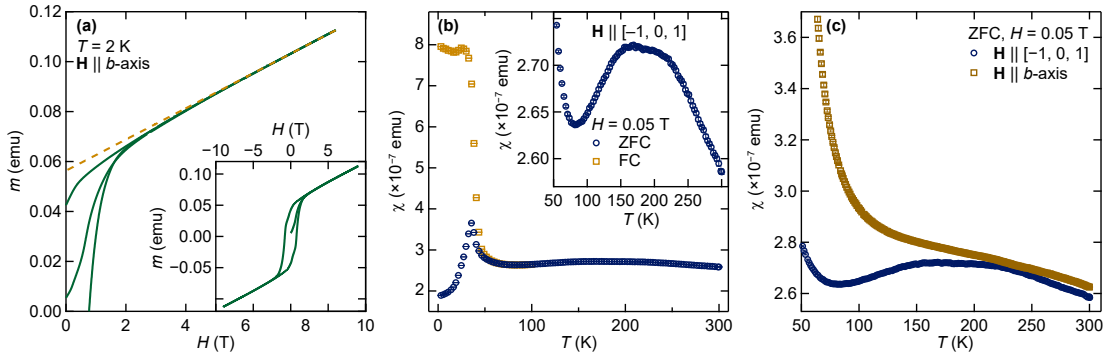

Figure 6.2: Bulk magnetization measurements taken on single crystals of α-NaMnO$_2$. Panel (a) shows $T = 2$ K magnetic field sweeps with $\mathbf{H} \parallel b$-axis of α-NaMnO$_2$ and Mn$_3$O$_4$. The dashed orange line is a fit to the high field data between $8.5 < H(\mathrm{T}) < 9$ used for extracting the mass percentage of Mn$_3$O$_4$ intergrowth in the sample as described in the text. Panel (b) shows zero-field cooled (ZFC) and field cooled (FC) magnetic susceptibility data with $H = 0.05$ T and $\mathbf{H} \parallel [-1, 0, 1]$-axis of α-NaMnO$_2$. The inset highlights the high temperature region where characteristics of low dimensional magnetism can be seen. Panel (c) shows the comparison of the broad feature at high temperatures between the two orientations.

momentum space the Mn$_3$O$_4$ magnetic scattering was, we had to know that it behaved like the bulk. The onset of hysteresis at the reported $T_\mathrm{C} = 43$ K in susceptibility measurements indicates as much, but additional evidence lies in the order parameter of the Mn$_3$O$_4$ (0, 4, 0) Bragg peak. There should be no nuclear or magnetic contribution from the α-NaMnO$_2$ at this momentum (corresponding to the (0, 1, 0) of α-NaMnO$_2$), and the integrated intensity from H and K scans are shown in Fig. 6.3. Both the onset

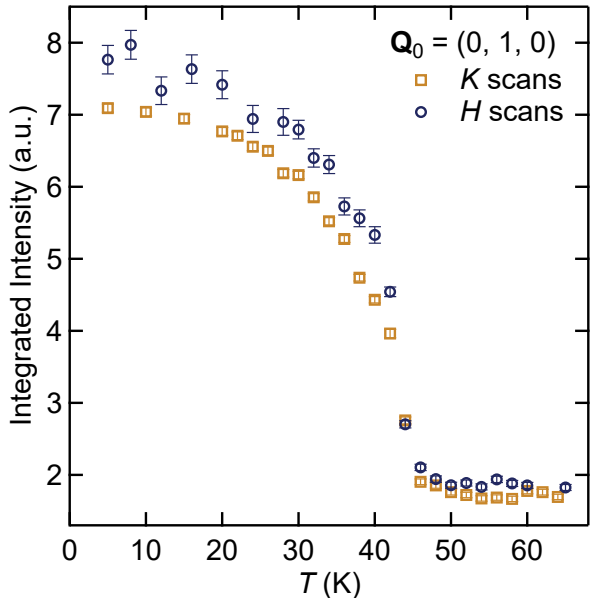

Figure 6.3: Triple-axis neutron data of H and K scans centered at $\mathbf{Q}_0 = (0, 1, 0)$. This momentum corresponds to the Mn$_3$O$_4$ (0, 4, 0) Bragg peak position.

of long range order at $T_C = 43$ K and the second-order transition behavior characteristic of Mn_3O_4 are observed.

6.4 Results

6.4.1 High temperature short-range correlations: $T > T_{N1}$

Short range magnetic correlations begin to develop in α-$NaMnO_2$ well above any observed ordering. Zero-field cooled susceptibility data in the inset of Fig. 6.2 (b) show a broad hump centered around 200 K, characteristic of magnetic correlations in low-dimensional materials. Above $T = 43$ K, Mn_3O_4 is paramagnetic and follows Curie's law, and thus, the feature is not coming from the intergrowth. Additionally, this feature was seen in polyscrystalline samples in Refs. [10, 11]. This feature is enhanced in the $\mathbf{H}||[-1,0,1]$ configuration (i.e. $\mathbf{H}$ is along the direction of the moments' easy-axis) when compared to the $\mathbf{H}||[0,1,0]$ configuration as shown in Fig. 6.2 (c). The magnitude of χ for the $\mathbf{H}||[0,1,0]$ was scaled for Fig. 6.2 (c) by the ratio of the sample masses for each configuration $\left(\frac{\text{mass of } \mathbf{H}||[-1,0,1] \text{ sample}}{\text{mass of } \mathbf{H}||[0,1,0] \text{ sample}}\right)$. The anisotropy between the two orientations is most likely due to the large tail coming from the onset of magnetic order in Mn_3O_4 for the $\mathbf{H}||[0,1,0]$ orientation, because $\mathbf{H}$ is along the ferromagnetic easy-axis of the Mn^{2+} moments.

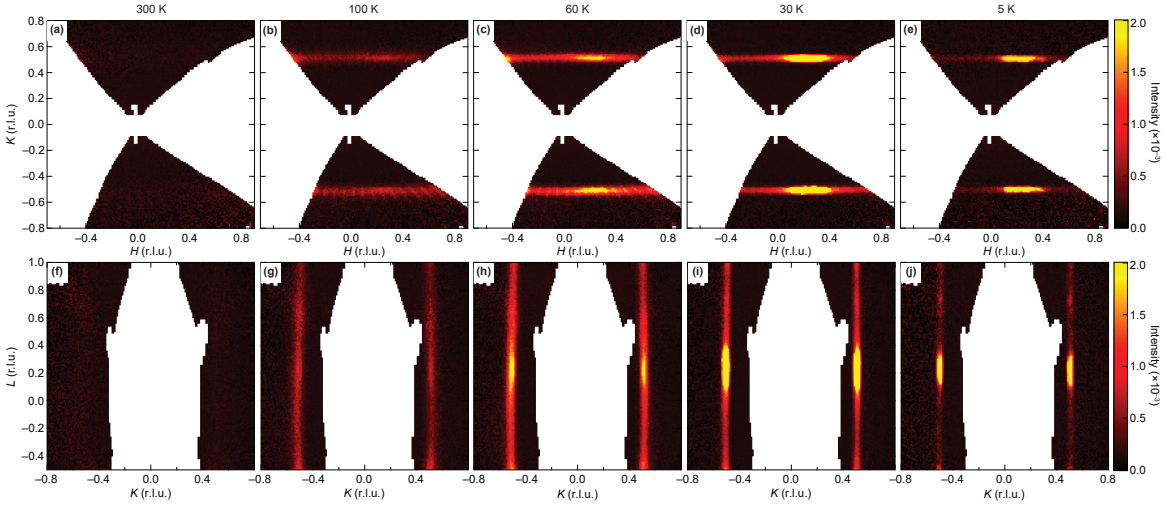

Figure 6.4: Slices of scattering planes from the time-of-flight neutron spectrometer, CORELLI, at different temperatures. Panels (a)-(e) show slices of the (H, K, 0.25) plane with $0.15 < L$ (r.l.u.) < 0.35. Panels (f)-(j) show slices of the (0.25, K, L) plane with $0.15 < L$ (r.l.u.) < 0.35. Maxima along the diffuse scattering rods correspond to a different set of diffuse scattering rods, which cut through the planes at these points.

The correlations at high temperature were confirmed from neutron time-of-flight data on a single crystal. Neutron time-of-flight measurements were taken at the Spallation Neutron Source at Oak Ridge National Laboratory using the instrument, CORELLI [17]. The ≈0.5 g single crystal was mounted on a thin aluminum plate and sealed in an aluminum can under an inert environment, which was then placed in a CCR cryostat. The CORELLI beam is modulated by a statistical chopper, and using a cross-correlation method, the elastic signal can be reconstructed. The energy discrimination makes it an ideal instrument to study frustrated and low-dimensional magnetic materials. Figs. 6.4 (a)-(e) are 2D slices of the (H, K, 0.25) plane with L integrated from 0.15 to 0.35. By choosing L away from the 3D ordered zone-center, we are assured that any signal seen is coming from diffuse scattering. Panel (a) shows data collected at 300 K and (b) and (c) show the same set of scans taken at 100 K and 60 K, respectively. Starting at 100 K, scattering centered around $K = \pm 0.5$ r.l.u. can be seen stretching across an entire zone along H, confirming short range correlations along H and the magnetic anisotropy leading to the quasi-1D behavior along K, where the J_1 exchange interaction dominates. The diffuse signal continues to get stronger as the temperature is decreased to 60 K. Similar behavior is observed along L in slices of the (0.25, K, L) plane shown in Figs. 6.4 (f)-(j), where 300 K, 100 K and 60 K are panels (f), (g) and (h), respectively. Each panel taken below 300 K in Fig. 6.4 reveals maxima located along the diffuse scattering rods. The maxima are due to an additional set of diffuse scattering rods, which are structural in nature, cutting through the slices at the maxima positions (these rods are also seen in electron diffraction measurements of polycrystalline samples from Ref. [5].) These rods of diffuse scattering arise when the periodic condition for the crystal becomes broken by stacking faults. In α-$NaMnO_2$, the periodicity along the $[\bar{1}, 0, 1]$ direction becomes interrupted. Consequently, the periodicity of the magnetic order, once correlations are turned on, becomes broken along the $[\bar{1}, 0, 1]$ direction, which is the reason the maxima are not seen at 300 K. The maxima interfered with efforts to fit the data and extract correlation lengths, however, the data qualitatively demonstrate the quasi-1D behavior along the chain direction at high temperatures.

6.4.2 Magnetic ground state: $T < T_{N2}$

The magnetic ground state was probed using the cold triple-axis neutron diffraction instrument, SPINS, at the NIST Center for Neutron Research, with a flat analyzer and fixed incident and final energies of 5 meV. All data were analyzed with fits to Voigt functions, in which the Gaussian width was fixed to be the spectrometer resolution determined by using the program, ResLib [18]. Unless otherwise specified, the collimation used was open$-40'-40'-$open (denoting the collimations before the monochromator, sample, analyzer, and detector, respectively). The ordering wavevector was confirmed by the observations of spectral weight buildup about $\mathbf{G}_{HKL} \pm \mathbf{k}_1$ and $\mathbf{k}_2$ positions (where $\mathbf{G}_{HKL}$ are allowed nuclear Bragg positions), which could be fit and analyzed to extract correlation lengths starting at $\approx$ 60 K in the $(HK0)$ scattering plane (the two other domains stemming from the crystallographic twin as discussed in Section II A were also observed). Figs. 6.5 (a) and (b) show the integrated intensity and correlation lengths,

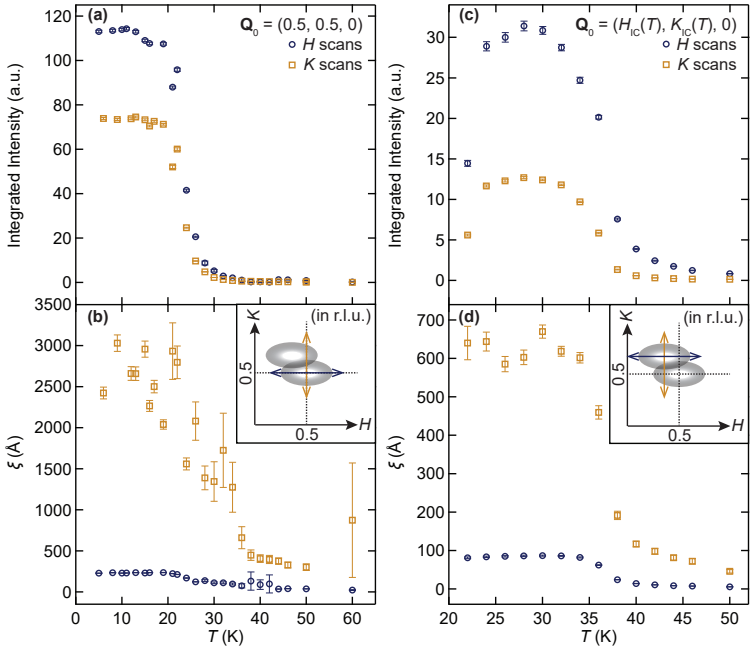

Figure 6.5: Temperature dependent parameters extracted from peak fitting analysis. For all panels, data from H scans are represented by blue circles, and data from K scans are represented by orange squares. Panels (a) and (c) are scans centered about the commensurate position $(1/2, 1/2, 0)$. Panels (b) and (d) are centered about the incommensurate peak, where the center changes with temperature. The area of the commensurate peak along H and K as a function of temperature can be seen in panel (a). The same information for the incommensurate peak can be seen in panel (b). Correlation lengths along H and K for the commensurate peak as a function of temperature are in panel (c), and correlation lengths along H and K for the incommensurate peak are in panel (d).

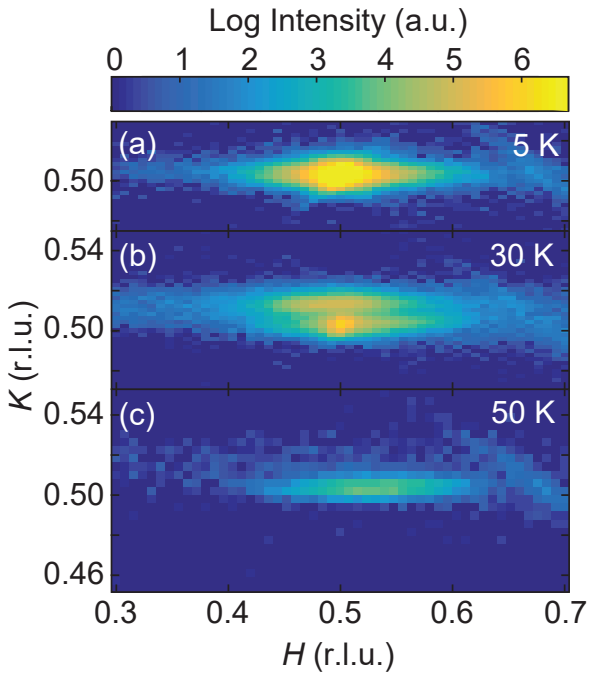

Figure 6.6: Temperature dependence of the scattering in the $(HK0)$ plane about the magnetic ordering wavevector. Panels (a), (b), and (c) were taken at 5 K, 30 K, and 50 K, respectively.

respectively, resulting from H and K scans centered about $\mathbf{Q}_0 = (0.5, 0.5, 0)$. Below $T_{\mathrm{N2}} = 22$ K, a single peak could be fit to the data, which exhibited a constant intensity along both H and K. The base temperature measurements reveal a quasi-long range ordered state with correlation lengths along $K \approx 2600$ Å and along $H \approx 230$ Å, where the anisotropy can be clearly seen in the mesh scan of Fig. 6.6 (a). The sharp onset of integrated intensity at T_{N2} implies the transition is not second-order in nature. An experimental geometry in the (H, H, L) scattering plane was also probed to study the behavior of correlations at the commensurate zone center between the layers of Mn ions. The order parameter of the integrated intensity shows the same behavior as both the H and K scans, and the correlation length at base temperature is ≈300 Å. The commensurate peak along L was extracted through L-scans in a separate experiment probing the (H, H, L) scattering plane. This data is in Fig. 6.7.

Neutron powder diffraction data were taken in order to refine the magnitude and direction of of the α-NaMnO$_2$ moments. The measurements were collected using the BT-1 32 detector neutron powder diffractometer at the NIST Center for Neutron Research. A Cu(311) monochromator with a 90° take-off angle, $\lambda = 1.5397(2)$ Å, and in-pile collimation of 60 minutes of arc were used. Data were collected over the range of

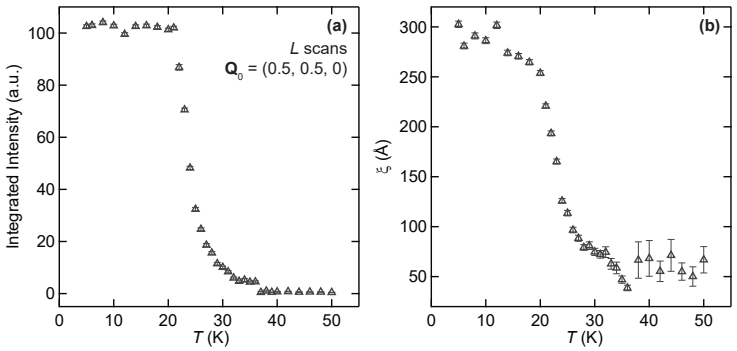

Figure 6.7: Temperature dependent parameters extracted from peak fitting analysis of L-scans centered about $\mathbf{Q}_0 = (0.5, 0.5, 0)$. Panel (a) shows the integrated intensity of these scans as a function of temperature and panel (b) shows the interplane correlation lengths.

$2\theta = 3 - 168°$, with a step size of 0.05°. About 3 g of crystal from a single growth run was ground and sealed in a vanadium container of length 50 mm and diameter 9.2 mm inside a dry He-filled glovebox, which was then placed in a CCR cryostat. Data were analyzed using FullProf [19] for Rietveld refinement and SARAh [20] for magnetic representational analysis. First, room temperature data were analyzed using a two phase model: Mn_3O_4 nuclear and α-$NaMnO_2$ nuclear. This model was taken to be the structural contribution to the low temperature data. The structural fit is vastly improved if a refinement accounting for the stacking faults and twin boundaries is performed. This type of refinement cannot yet be used for quantitative phase analysis or magnetic refinements, so for purposes of approximating the moment direction, the Rietveld method in conjunction with irreducible representation analysis was used. The details of the structural calculation resulting from refinement of the faulted structural model, can be found in Appendix B.

The $T = 5$ K data are shown in Fig. 6.8. The refinement include two additional phases to the structural model: Mn_3O_4 magnetic and α-$NaMnO_2$ magnetic. It should be noted that both the room temperature and base temperature lattice parameter refinements indicate the Mn_3O_4 phase is slightly strained from it's bulk tetragonal structure, which, is not surprising if the Mn_3O_4–α-$NaMnO_2$ phase boundary is to be nearly lattice-matched. The Mn_3O_4 magnetic phase was not refined, and the moments' magnitudes and directions were fixed to be reported values [21]. It was necessary to include the magnetic phase of the Mn_3O_4 in order to refine the moment direction and magnitude for α-$NaMnO_2$ because of a partial overlap of the most intense magnetic Bragg peaks from

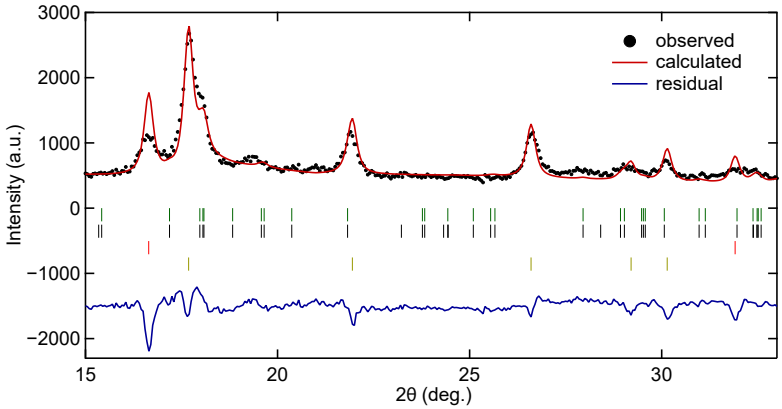

Figure 6.8: Neutron powder diffraction profile of a crushed α-NaMnO$_2$ single crystal with calculated magnetic Rietveld refinement at $T = 5$ K. Tick marks represent Bragg positions for the following phases, starting from the set on the top row: Mn_3O_4 nuclear (green), Mn_3O_4 magnetic (black), α-NaMnO$_2$ nuclear (red), and α-NaMnO$_2$ magnetic (yellow).

each phase near $2\theta \approx 18°$ as shown in Fig. 6.8. The refined base temperature lattice parameters for α-NaMnO$_2$ using the $C2/m$ space group are $a = 5.6336(3)$, $b = 2.8589(2)$, $c = 5.7715(3)$, and $\beta = 112.863(4)$. The Mn moments from α-NaMnO$_2$ were refined using irreducible representational analysis with the basis vectors presented in Table 6.1.

Only basis vectors $\boldsymbol{\psi}_1$ and $\boldsymbol{\psi}_3$, with coefficients of opposite sign, were needed to capture the magnetic peak intensities, and attempts to refine $\boldsymbol{\psi}_2$, which represents a projection of the moment along the b-axis, yielded zero within error, so the coefficient for $\boldsymbol{\psi}_2$ was fixed to be null. The Mn moments refined to a direction of 38(2)° out of the ab-plane (and perpendicular to the b-axis), with the projections along the a and c axes $m(a) = -1.29(7)$ μ_B and $m(c) = 1.61(7)$ μ_B, respectively. The total saturated moment of 2.42(7) μ_B/Mn^{3+} is significantly reduced from the theoretical value of 4 μ_B/Mn^{3+}. Two effects are most likely at play: firstly, the fault defects are going to modify the magnetic peak shapes in much the same way they do the structural peaks. It is clear from the inset in Fig. 6.8 that the magnetic refinement does not produce a very satisfactory fit, and this could be the reason that the saturated moment is smaller than that reported ([10]). Secondly, that reported value is already quite reduced from the theoretical value at 2.92 μ_B/Mn^{3+}, which is undoubtedly due to the quasi long-range nature of the magnetic order and that much of the magnetic spectral weight is shoveled into the inelastic channel due to coherent fluctuations of both the order parameter's phase and amplitude [8, 22].

IR	BV	Atom	BV components					
			$m_{\|a}$	$m_{\|b}$	$m_{\|c}$	$im_{\|a}$	$im_{\|b}$	$im_{\|c}$
Γ_1	$\boldsymbol{\psi}_1$	1	2	0	0	0	0	0
	$\boldsymbol{\psi}_2$	1	0	2	0	0	0	0
	$\boldsymbol{\psi}_3$	1	0	0	2	0	0	0

Table 6.1: Basis vectors for the space group $C2/m$ with $\mathbf{k}_4 = (.5,\ .5,\ 0)$. The decomposition of the magnetic representation for the Mn site $(0,\ 0,\ 0)$ is $\Gamma_{Mag} = 3\Gamma_1^1 + 0\Gamma_2^1$. The atom of the primitive basis is defined according to 1: $(0,\ 0,\ 0)$. Table output was created using SARAh [20].

6.4.3 Incommensurate critical scattering: $T_{\mathrm{N2}} < T < T_{\mathrm{N1}}$

Preceding the quasi-long-range ordered state, an incommensurate peak coexisting alongside the commensurate peak is observed, with a representative image at $T = 30$ K shown in Fig. 6.6 (b). The transition temperature of this incommensurate phase is determined to be $T_{\mathrm{N1}} = 36$ K, from the order parameter-like trend of the integrated intensities extracted from H and K scans about the peak shown in Fig. 6.5 (c), however, the peak can be seen starting at ≈ 50 K. Mn_3O_4 undergoes multiple phase transition starting from $T_{\mathrm{C}} = 43$ K [12], and we were able to ensure that the incommensurate peak was not coming from one of those phases because the growth orientation with respect to α-$NaMnO_2$ is known. In fact, near the α-$NaMnO_2$ zone center, there are no structural or magnetic Mn_3O_4 peaks close enough to interfere with data collection. The incommensurate peak is diffuse and indicative of short-range phase behavior, and, like the commensurate peak, always has a longer correlation length along K than H (see Fig. 6.5 (d)). The center position of the incommensurate peak, $(H_{\mathrm{IC}}(T), K_{\mathrm{IC}}(T), 0)$, is a function of temperature, where $H_{\mathrm{IC}}(T) = 0.5 + \delta_H(T)$ r.l.u. and $K_{\mathrm{IC}}(T) = 0.5 + \delta_K(T)$ r.l.u., as shown in Fig. 6.9.

The displacement, $\delta_K(T)$, trends steadily towards the commensurate position with decreasing temperature after a maximal displacement of 0.015 r.l.u. at $T = 46$ K. At T_{N2}, within resolution, δ_K jumps to zero. This also corresponds with a collapse in intensity as shown in Fig. 6.5 (c). The two peaks are well-resolved for most of the temperature range in which they coexist because of the longer correlation lengths along this direction when compared to along H. The displacement, $\delta_H(T)$, behaves opposite that of $\delta_K(T)$: the maximal displacement is right above T_{N2} at ≈ -0.020 r.l.u. and moves closer to the commensurate position with increasing temperature. However, like $\delta_K(T)$, the displacement is unresolvable from the commensurate position at T_{N2} after a sudden drop in intensity. Both the H and K scans about the incommensurate $\mathbf{Q}$

have maximal integrated intensities at $T = 28$ K. The buildup in intensity, and sudden decrease, is suggestive of critical scattering, although no sharp divergence in the correlation lengths along H and K are observed (although a sudden increase at T_{N1} is seen). The same intensity effect, although without the resolution to resolve the commensurate and incommensurate peaks, can be seen in the neutron time-of-flight data in Figs. 6.4 (c)-(e) and (h)-(j), where the diffuse scattering across the H and L zones reaches a maximum in intensity above T_{N2} before decreasing below T_{N2}. To further explore this effect, zone boundary K scans were taken away from the from both the incommensurate and commensurate peaks at $H = 0.25$ r.l.u. as shown in Fig. 6.10 (these data were taken with open$-80'-80'-$open collimation). The center position in K of the zone-boundary scattering matches that of the K-scan data in Fig. 6.9 (a). Additionally, the integrated intensity of zone-boundary scattering shows the same behavior, seen in Fig. 6.10 (b). The same panel also displays the correlation length, which reaches a maximum at the same temperature as the intensity maxima before steadying. These data further imply that the critical-like scattering observed is originating from the incommensurate phase, where long-range order is destabilized by the commensurate phase at T_{N2}.

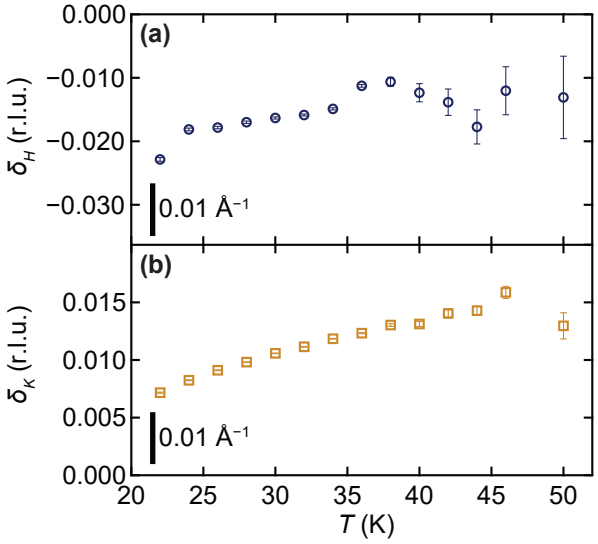

Figure 6.9: Tracking of the incommensurate scattering as a function of temperature. Panel (a) displays the center position of the incommensurate peak, with respect to the commensurate position, along H. Each data point has a different fixed K, which is the center of the incommensurate peak along K. The open orange squares in panel (b) are the center positions of the incommensurate peak, with respect to the commensurate position, along K, where each data point has a different fixed H, which is the center of the incommensurate peak along H.

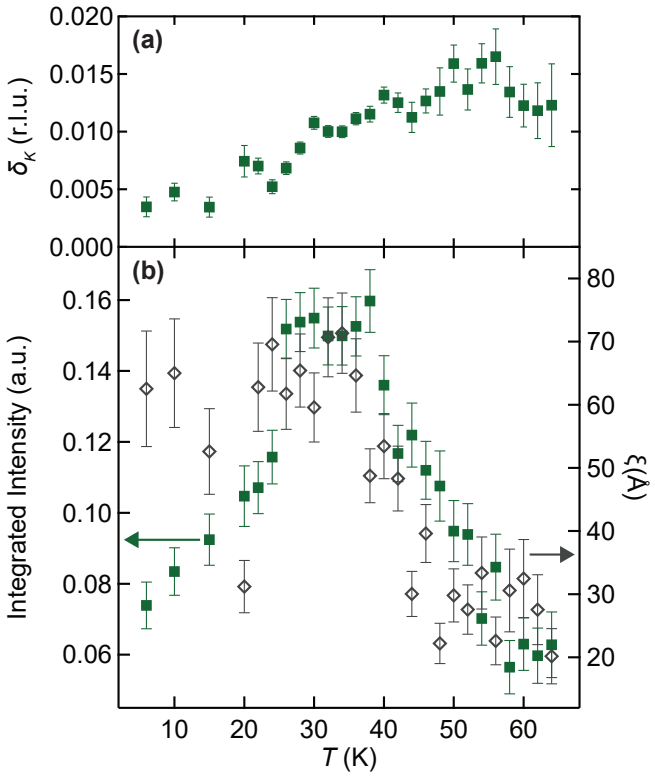

Figure 6.10: Tracking of the diffuse critical scattering at the zone boundary. The filled green squares in panel (a) represent the peak of the diffuse scattering along K at the zone boundary (ZB), where H= 0.25 (r.l.u.). The filled green squares in panel (b) show the integrated area of the diffuse scattering peak at the ZB and the open gray diamonds represent the correlation length of the diffuse scattering at the ZB.

6.5 Discussion

α-NaMnO$_2$ is a structurally complex material to synthesize and the intergrowth of Mn$_3$O$_4$, twinning, stacking faults, and β-phase polymorph have been well characterized and their respective contributions to the scattering planes mapped to ensure the data collected near the antiferromagnetic zone center of α-NaMnO$_2$ are not contaminated with any extraneous signals.

The broad maxima in the magnetic susceptibility of α-NaMnO$_2$ is characteristic of spatially anisotropic triangular lattices (and other low-dimensional, frustrated antiferromagnets) [23], and signifies the onset of antiferromagnetic correlations, which slowly drive the susceptibility down, as opposed to a sharp decrease at the Néel temperature of a 3D ordered antiferromagnet. The susceptibility implies that the correlations are beginning to develop at temperatures as high as T = 200 K. Time-of-flight neutron scattering data add to the quasi-1D picture of α-NaMnO$_2$ by demonstrating that cor-

relations along K, the intrachain direction, are longer than interchain and interplane correlations for the entirety of the temperature range probed below $T \leq 100$ K.

Between $T_{N1} < T < T_{N2}$, the picture is much more complicated by the coexistence of two short-range ordered states. As T_{N1} is approached from T_{N2}, it is not clear whether the system will order incommensurately or commensurately. And it is not until T_{N1} that the incommensurate wavevector jumps to the commensurate position following a sudden decrease in integrated intensity. The single-ion anisotropy, at $D = 2.5$ K, favors a collinear antiferromagnetic state, but with $D/J_2 \approx 0.3$, there exists substantial interchain frustration, leading to competing magnetic orderings between $T_{N1} < T < T_{N2}$.

Many systems with the same magnetic lattice topology as α-$NaMnO_2$ have been shown to host sinusoidally modulated spin textures, which undergo an additional magnetic transition at lower temperatures to a collinear antiferromagnetic state. $Li_2NiW_2O_8$ [24], $CoNb_2O_6$ [25, 26], and Cs_2CuCl_4 [27, 28] and $CuFeO_2$ [29, 30, 31] are all examples of quasi-1D materials exhibiting this behavior. $CuFeO_2$ has a particularly interesting connection to α-$NaMnO_2$, as it is a member of the ABO_2 delafossite group (and the mineral is actually the origin of the group name). $CuFeO_2$ has the classic delafossite triangular lattice at room temperature, but goes through two spin-lattice mediated structural transitions. The higher temperature transition sees a lowering to $C2/m$ symmetry, which transforms the Cu^{2+} isotropic triangular lattice to anisotropic. It is here that a disordered, incommensurate, sinusoidally modulated spin configuration sets in with a temperature dependent wavevector. Collinear antiferromagnetism associated with another lowering of structural symmetry appears at a lower temperature with some phase coexistence indicating a first order transition. Neither magnetic phase was shown to be long-range. Typically, incommensurate wavevectors lead to satellite peaks on either side of a commensurate position. In α-$NaMnO_2$, the observation of a one-sided satellite (i.e. at $\mathbf{Q} = (\frac{1}{2}, \frac{1}{2}, 0) + (\delta_H, \delta_K, 0)$ versus $(\frac{1}{2}, \frac{1}{2}, 0) \pm (\delta_H, \delta_K, 0)$) is indicative of sinusoidally ordered moments. Ref. [27] has a thorough explanation of the magnetic form factor calculations and symmetry constraints which lead to this effect for the quasi-1D Cs_2CuCl_4 lattice. It should be noted that the $C2/m$ space group with the ordering wavevector, $(q_x, q_y, 0)$, has no irreducible representations which could lead to a sinusoidally modulated magnetic structure. However, several studies [32, 11, 10, 33] on α-$NaMnO_2$ have

evidence that strong spin-lattice coupling likely drives the structural symmetry lower as magnetic order sets in, although the resolution of the experiments presented here does not allow us to confirm or rule out this structural change. In the previous studies, the samples were polycrystalline, and those studies would not have had the resolution in NPD to see the small, and short-ranged, incommensurate state presented here.

With the assumption that there is probably a lowering of structural symmetry in α-$NaMnO_2$, which allows for sinusoidally modulated magnetic order, we can turn to two examples of quasi-1D magnets where the incommensurability of the wavevector was predicted on anisotropic triangular lattice models. Refs. [34, 26] studied Cs_2CuCl_4 and $CoNb_2O_6$, respectively. The intrachain, and weaker interchain interaction, were used to calculate the wavevector in the mean field approximation of the Ising model: $\delta_K = \frac{1}{\pi}\arcsin\left(\frac{J_2}{2J_1}\right)$. Both of these examples only saw modulated order along the intrachain direction, and taking α-$NaMnO_2$ in that limit, as the incommensurability is larger and longer range along that direction, we arrive at $\delta_K = 0.02$ r.l.u. which is satisfyingly close to the maximum displacement of $\delta_K(T = 45\text{ K}) = 0.015$ r.l.u.

A pointed difference between α-$NaMnO_2$ and the anisotropic triangular examples is that the temperature regime just above T_{N1} sees the coexistance of a still disordered phase, incommensurate short-range order, and commensurate short-range order. Additionally, the critical-like scattering behavior, temperature dependent-wavevector, and first-order transition between the incommensurate and commensurate phases suggest that the system is in the vicinity of a Lifshitz point, much like in UAs [35], where exchange anisotropy and geometric frustration lead to a competition between different magnetic orderings. In-depth reports [36, 37] on the structural inhomogeneity and magnetoelastic effects within α-$NaMnO_2$ found that the system does not undergo a bulk transition to a triclinic phase, but is phase separated into nanoscale regions. It is possible that the coexistence of phases is merely a reflection of the structural inhomogeneity, which does get fully relieved at T_{N2}. Ideally, single crystals with less structural complexity could provide answers to some of the ambiguity surrounding the indirect evidence for a structural transition accompanying the modulated order at T_{N1}. However, the availability of these crystals provided the first evidence for the system's proximity to an additional magnetic ordering, demonstrating the richness that the combination of geo-

metrical frustration and single-ion anisotropy can bring to the phase diagram. Magnetic field studies with the goal of tuning the system to a region of stabilized modulated order would certainly provide further insight into the phase.

6.6 Conclusions

α-NaMnO$_2$ is a quasi-1D magnet, with intrachain correlations developing at temperatures as high as 200 K. The magnetic Mn^{3+} ions on the spatially anisotropic triangular lattice host coexisting commensurate and incommensurate short-range order between $T_{\mathrm{N2}} < T <_{\mathrm{N1}}$. The incommensurate phase appears to be modulated with a temperature dependent wavevector, and below T_{N2}, the system remains still only quasi long-range. The phase diagram is an example of the rich phases which can come about via geometrical frustration coupled with the Hamiltonian-tuning effects of single-ion anisotropy and competing exchange interactions.

Acknowledgements

S.D.W. and R.L.D. gratefully acknowledge support from DOE, Office of Science, Basic Energy Sciences under Award DE-SC0017752. The research reported here made use of shared facilities of the UCSB MRSEC (NSF DMR 1720256), a member of the Materials Research Facilities Network (www.mrfn.org). A portion of this research used resources at the Spallation Neutron Source, a DOE Office of Science User Facility operated by the Oak Ridge National Laboratory. We acknowledge the support of the National Institute of Standards and Technology, U.S. Department of Commerce, in providing the neutron research facilities used in portions of this work.

References

[1] Yunoki, S. & Sorella, S. Two spin liquid phases in the spatially anisotropic triangular Heisenberg model. *Phys. Rev. B* **74**, 014408 (2006).

[2] Starykh, O. A. & Balents, L. Ordering in Spatially Anisotropic Triangular Antiferromagnets. *Phys. Rev. Lett.* **98**, 077205 (2007).

[3] Nakano, H., Todo, S. & Sakai, T. Long-Range Order of the Three-Sublattice Structure in the S=1 Heisenberg Antiferromagnet on a Spatially Anisotropic Triangular Lattice. *Journal of the Physical Society of Japan* **82**, 043715 (2013).

[4] Li, P. H. Y. & Bishop, R. F. Magnetic order in spin-1 and spin-3/2 interpolating square-triangle Heisenberg antiferromagnets. *The European Physical Journal B* **85**, 25 (2012).

[5] Abakumov, A. M., Tsirlin, A. A., Bakaimi, I., Van Tendeloo, G. & Lappas, A. Multiple Twinning As a Structure Directing Mechanism in Layered Rock-Salt-Type Oxides: $NaMnO_2$ Polymorphism, Redox Potentials, and Magnetism. *Chemistry of Materials* **26**, 3306–3315 (2014).

[6] Billaud, J. *et al.* β-$NaMnO_2$: A High-Performance Cathode for Sodium-Ion Batteries. *Journal of the American Chemical Society* **136**, 17243–17248 (2014). PMID: 25397400.

[7] Radin, M. D. & Van der Ven, A. Simulating Charge, Spin, and Orbital Ordering: Application to Jahn-Teller Distortions in Layered Transition-Metal Oxides. *Chemistry of Materials* **30**, 607–618 (2018).

[8] Dally, R. L. *et al.* Amplitude mode in the planar triangular antiferromagnet $Na_{0.9}MnO_2$. *Nature Communications* **9**, 2188 (2018).

[9] Ovsyannikov, S. V. *et al.* Perovskite-like Mn_2O_3: A Path to New Manganites. *Angewandte Chemie International Edition* **52**, 1494–1498.

[10] Giot, M. *et al.* Magnetoelastic Coupling and Symmetry Breaking in the Frustrated Antiferromagnet $\alpha-NaMnO_2$. *Phys. Rev. Lett.* **99**, 247211 (2007).

[11] Zorko, A. *et al.* Magnetic interactions in $\alpha-NaMnO_2$: Quantum spin-2 system on a spatially anisotropic two-dimensional triangular lattice. *Phys. Rev. B* **77**, 024412 (2008).

[12] Chardon, B. & Vigneron, F. Mn_3O_4 commensurate and incommensurate magnetic structures. *Journal of Magnetism and Magnetic Materials* **58**, 128 – 134 (1986).

[13] Kemei, M. C., Harada, J. K., Seshadri, R. & Suchomel, M. R. Structural change and phase coexistence upon magnetic ordering in the magnetodielectric spinel $\mathbf{Mn_3O_4}$. *Phys. Rev. B* **90**, 064418 (2014).

[14] Dwight, K. & Menyuk, N. Magnetic Properties of Mn_3O_4 and the Canted Spin Problem. *Phys. Rev.* **119**, 1470–1479 (1960).

[15] Nielsen, O. V. & Roeland, L. W. High-field magnetization for Mn_3O_4 single crystals. *Journal of Physics C: Solid State Physics* **9**, 1307 (1976).

[16] Suzuki, T. & Katsufuji, T. Magnetodielectric properties of spin-orbital coupled system Mn_3O_4. *Phys. Rev. B* **77**, 220402 (2008).

[17] Rosenkranz, S. & Osborn, R. Corelli: Efficient single crystal diffraction with elastic discrimination. *Pramana* **71**, 705–711 (2008).

[18] Zheludev, A. ResLib: 3-axis resolution library for MatLab (ETH Zürich, 2009).

[19] Rodríguez-Carvajal, J. Recent advances in magnetic structure determination by neutron powder diffraction. *Physica B: Condensed Matter* **192**, 55 – 69 (1993).

[20] Wills, A. A new protocol for the determination of magnetic structures using simulated annealing and representational analysis (sarah). *Physica B: Condensed Matter* **276-278**, 680 – 681 (2000).

[21] Jensen, G. B. & Nielsen, O. V. The magnetic structure of Mn_3O_4 Hausmannite between 4.7K and Neel point, 41K. *Journal of Physics C: Solid State Physics* **7**, 409 (1974).

[22] Stock, C. *et al.* One-Dimensional Magnetic Fluctuations in the Spin-2 Triangular Lattice $\alpha-NaMnO_2$. *Phys. Rev. Lett.* **103**, 077202 (2009).

[23] Zheng, W., Singh, R. R. P., McKenzie, R. H. & Coldea, R. Temperature dependence of the magnetic susceptibility for triangular-lattice antiferromagnets with spatially anisotropic exchange constants. *Phys. Rev. B* **71**, 134422 (2005).

[24] Ranjith, K. M. *et al.* Commensurate and incommensurate magnetic order in spin-1 chains stacked on the triangular lattice in $Li_2NiW_2O_8$. *Phys. Rev. B* **94**, 014415 (2016).

[25] Heid, C. *et al.* Magnetic phase diagram of $CoNb_2O_6$: A neutron diffraction study. *Journal of Magnetism and Magnetic Materials* **151**, 123 – 131 (1995).

[26] Kobayashi, S., Mitsuda, S., Ishikawa, M., Miyatani, K. & Kohn, K. Three-dimensional magnetic ordering in the quasi-one-dimensional Ising magnet $CoNb_2O_6$ with partially released geometrical frustration. *Phys. Rev. B* **60**, 3331–3345 (1999).

[27] Coldea, R. *et al.* Neutron scattering study of the magnetic structure of Cs_2CuCl_4. *Journal of Physics: Condensed Matter* **8**, 7473 (1996).

[28] Isakov, S. V., Senthil, T. & Kim, Y. B. Ordering in Cs_2CuCl_4: Possibility of a proximate spin liquid. *Phys. Rev. B* **72**, 174417 (2005).

[29] Mitsuda, S., Kasahara, N., Uno, T. & Mase, M. Partially Disordered Phase in Frustrated Triangular Lattice Antiferromagnet $CuFeO_2$. *Journal of the Physical Society of Japan* **67**, 4026–4029 (1998).

[30] Petrenko, O. A., Lees, M. R., Balakrishnan, G., de Brion, S. & Chouteau, G. Revised magnetic properties of $CuFeO_2$-a case of mistaken identity. *Journal of Physics: Condensed Matter* **17**, 2741 (2005).

[31] Ye, F. *et al.* Spontaneous spin-lattice coupling in the geometrically frustrated triangular lattice antiferromagnet $CuFeO_2$. *Phys. Rev. B* **73**, 220404 (2006).

[32] Ouyang, Z. W. & Wang, B. First-principles study of structural distortions in frustrated antiferromagnet α-$NaMnO_2$. *Phys. Rev. B* **82**, 064405 (2010).

[33] Jia, T. *et al.* Magnetic frustration in α-$NaMnO_2$ and $CuMnO_2$. *Journal of Applied Physics* **109**, 07E102 (2011).

[34] Dalidovich, D., Sknepnek, R., Berlinsky, A. J., Zhang, J. & Kallin, C. Spin structure factor of the frustrated quantum magnet Cs_2CuCl_4. *Phys. Rev. B* **73**, 184403 (2006).

[35] Sinha, S. K., Lander, G. H., Shapiro, S. M. & Vogt, O. Neutron scattering investigation of the phase transitions in uranium arsenide. *Phys. Rev. B* **23**, 4556–4566 (1981).

[36] Zorko, A., Kokalj, J., Komelj, M., Arčon, D. & Lappas, A. Frustration-induced nanometre-scale inhomogeneity in a triangular antiferromagnet. *Nature Communications* **5**, 3222 (2014).

[37] Zorko, A. *et al.* Magnetic inhomogeneity on a triangular lattice: the magnetic-exchange versus the elastic energy and the role of disorder. *Scientific Reports* **5**, 9272 (2015).

Chapter 7

Magnon dynamics in α-$NaMnO_2$

The work presented in this chapter is the result of collaborations and authorship is shared. The theoretical work on the spin dynamics was performed by L. Balents, and a detailed description of his findings can be found in the supplementary information of the publication. Previous publication of this data and analysis can be found in *Nature Communications*:

> Dally, R. L., Zhao, Y., Xu, Z., Chisnell, R., Stone, M. B., Lynn, J. W., Balents, L. Wilson, S. D. Amplitude mode in the planar triangular antiferromagnet $Na_{0.9}MnO_2$. *Nat. Commun.* **9**, 2188 (2018).

7.1 Introduction

Amplitude modes arising from symmetry breaking in materials are of broad interest in condensed matter physics. These modes reflect an oscillation in the amplitude of a complex order parameter, yet are typically unstable and decay into oscillations of the order parameter's phase. This renders stable amplitude modes rare, and exotic effects in quantum antiferromagnets have historically provided a realm for their detection. Here we report an alternate route to realizing amplitude modes in magnetic materials by demonstrating that an antiferromagnet on a two-dimensional anisotropic triangular lattice (α-$Na_{0.9}MnO_2$) exhibits a long-lived, coherent oscillation of its staggered magnetization field. Our results show that geometric frustration of Heisenberg spins with uniaxial single-ion anisotropy can renormalize the interactions of a dense two-dimensional network of moments into largely decoupled, one-dimensional chains that manifest a longitudinally polarized bound state. This bound state is driven by the Ising-like anisotropy inherent to the Mn^{3+} ions of this compound.

Many of the seminal observations of amplitude modes in magnetic materials arise from quantum effects in one-dimensional antiferromagnetic chain systems when interchain coupling drives the formation of long-range magnetic order [1]. For instance, bound states observed in the ordered phases of $S = 1$ Haldane systems [2, 3, 4] or in the spinon continua of $S = 1/2$ quantum spin chains [5, 6, 7, 8, 9] were shown to be longitudinally polarized and reflective of the crossover into an ordered spin state. While the chemical connectivity of magnetic ions in these systems is inherently one-dimensional, alternative geometries such as planar, anisotropic triangular lattices can also in princi-

ple stabilize predominantly one-dimensional interactions in antiferromagnets [10]. In the simplest case, geometric frustration in a lattice comprised of isosceles triangles promotes dominant magnetic exchange along the short-leg of the triangle while the remaining two equivalent legs frustrate antiferromagnetic coupling between the chains. The result is a closely spaced two-dimensional network of magnetic moments whose dimensionality of interaction is reduced to be quasi one-dimensional.

A promising example of such an anisotropic triangular lattice structure is realized in α-phase $NaMnO_2$. Layered sheets of edge-sharing MnO_6 octahedra are separated by layers of Na ions, and the orbital degeneracy of the octahedrally coordinated Mn^{3+} cations ($3d^4$, $t_{2g}^3 e_g^1$ valence) is lifted via a large, coherent Jahn-Teller distortion [11]. This distorts the triangular lattice such that the leg along the in-plane b-axis is contracted 10% relative to the remaining two legs. As a result, the $S = 2$ spins of the Mn^{3+} ions decorate a dimensionally frustrated lattice where one-dimensional intrachain coupling along b is favored and interchain coupling is highly frustrated. This spin lattice eventually freezes into a long-range ordered state below $T_N = 45$ K [11]; however, previous studies of powder samples have suggested an inherently one-dimensional character to the underlying spin dynamics [12]. Such a scenario suggests an intriguing material platform for the stabilization of an amplitude mode in a conventional spin system (i.e. one with diminished local moment fluctuations and a quenched Haldane state [13]) as the ordered state is approached, and a static, staggered mean field is established.

In this chapter, single crystal neutron scattering data are presented which show that the planar antiferromagnet α-$Na_{0.9}MnO_2$ exhibits quasi one-dimensional spin fluctuations that persist into the AF ordered state. Additionally, the data reveal that an anomalous, dispersive spin mode appears as AF order sets in, and that this new mode is longitudinally polarized with an inherent lifetime limited by the resolution of the measurement. This longitudinally polarized bound state demonstrates the emergence of a magnetic amplitude mode in a spin system where geometric frustration lowers the dimensionality of magnetic interactions and amplifies fluctuation effects. Intriguingly, this occurs in a compound where strong quantum fluctuations inherent to $S = 1/2$ systems and singlet formation effects inherent to integer spin Haldane systems—both typical settings for longitudinal bound state formation—are absent. To explain the sta-

bilization of this amplitude mode, we present a model that captures the excitation as a two-magnon bound state whose binding energy derives from an easy-axis single-ion anisotropy inherent to the orbitally quenched Mn^{3+} ions. This anisotropy orients the moments along a preferred axis and renders them Ising-like. Our work establishes α-Na_xMnO_2 and related lattice geometries as platforms for realizing unconventional spin dynamics in a dense network of one-dimensional antiferromagnetic spin chains [14, 15].

7.2 Results

7.2.1 Crystal and spin structures of α-$Na_{0.9}MnO_2$

To demonstrate the emergence of an amplitude mode in α-$Na_{0.9}MnO_2$, careful descriptions of the lattice and spin structures are first necessary. We note here that units for wave vectors throughout the manuscript are given in reciprocal lattice units (H, K, L) where $\mathbf{Q}[\text{Å}^{-1}] = (\frac{2\pi}{a\sin\beta}H, \frac{2\pi}{b}K, \frac{2\pi}{c\sin\beta}L)$ and a, b, c, and β are the lattice parameters of the unit cell. Fig. 7.1 (a) shows the projection of the low temperature, ordered spin lattice of α-$NaMnO_2$ onto the ab-plane where one spin domain with propagation vector $\mathbf{q}_1 = (0.5, 0.5, 0)$ is illustrated. The antiferromagnetic chain direction is shaded in grey. Due to the degeneracy of the frustrated interchain coupling, a second spin domain with propagation vector $\mathbf{q}_2 = (-0.5, 0.5, 0)$ also stabilizes, and the moments in both domains are oriented approximately along the $[-1, 0, 1]$ apical oxygen bond direction due to an inherent uniaxial single-ion anisotropy [11]. The large Jahn-Teller distortion renders the lattice structure prone to crystallographic twinning [16] and the relative orientations of the moments in the two resulting crystallographic twins, twin 1 (t_1) and twin 2 (t_2) are depicted in Fig. 7.1 (b). This results in four allowed domains: t_1-$\mathbf{q}_1$, t_1-$\mathbf{q}_2$, t_2-$\mathbf{q}_1$, and t_2-$\mathbf{q}_2$. Crucially, the moments in both crystallographic and magnetic twin domains are nearly parallel to a common $[-1, 0, 1]$ axis. This is verified via polarized elastic neutron scattering measurements in the AF state at $T = 2.5$ K shown in Fig. 7.1 (c). These data demonstrate that in a single domain, t_1-$\mathbf{q}_1$, probed at $\mathbf{Q} = (0.5, 0.5, 0)$ the moments are rotated approximately 7° away from the $[-1, 0, 1]$ axis within the ac-plane. We note here that previous studies of stoichiometric $NaMnO_2$ have reported an extremely subtle distortion into a lower triclinic symmetry below the antiferromagnetic

transition [11]. Our neutron diffraction measurements fail to detect this distortion in the average structure of $Na_{0.9}MnO_2$ crystals, and we therefore analyze data using the higher symmetry monoclinic structure. A recent report suggests that the triclinic phase occurs only as an inhomogeneous local distortion [17]; hence our inability to observe the reported triclinic distortion may arise from its absence in the average structure, its suppression due to the Na vacancies in our samples, or due to the resolution threshold of our measurements. Despite this ambiguity, the reported triclinic distortion in $NaMnO_2$ is subtle and would generate roughly a 0.12% difference between next-nearest neighbor (interchain) exchange pathways, which can be neglected for the purposes of the present study.

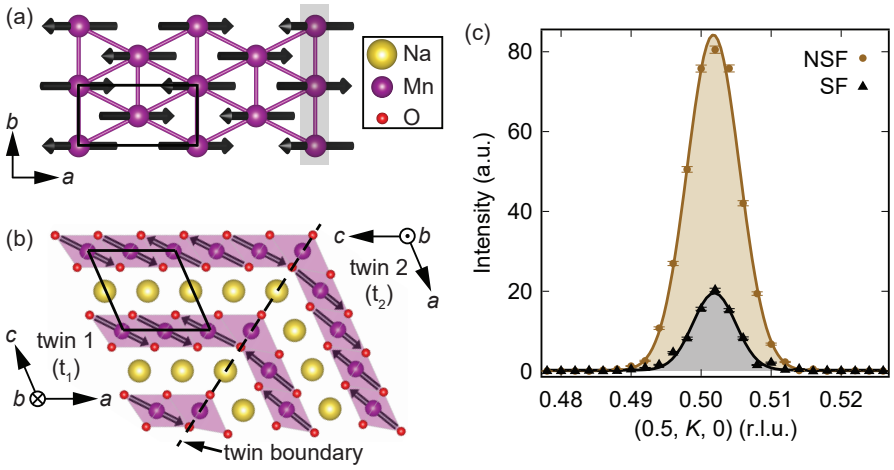

Figure 7.1: Summary of the crystal and magnetic structures of α-$NaMnO_2$. Panel (a) shows the projection of the 3D magnetically ordered state onto the *ab*-plane. The black rectangle denotes the chemical unit cell. The grey shaded region highlights the chain direction between nearest neighbor Mn atoms. Panel (b) shows the moments in the *ac*-plane, as well as the intergrowth of two twin domains. The black rhombus again denotes the chemical unit cell. Polarized elastic neutron data at the antiferromagnetic zone center in (c) confirm the orientation of the magnetic moments within the ordered state ($T = 2.5$ K) as previously reported. The shaded regions are the Gaussian fits of the non spin-flip (NSF) and spin-flip (SF) channels, which were used to determine the moment orientation. The neutron polarization $\mathbf{P}$ is perpendicular to the scattering vector and parallel to the *c*-axis in this configuration. Error bars represent one standard deviation.

7.2.2 Spin Hamiltonian of α-$Na_{0.9}MnO_2$

In order to understand the interactions underlying the AF ground state of this system, inelastic neutron scattering measurements were performed. Spin excitations measured within the ordered state about the AF zone centers, $\mathbf{Q} = (1.5, \pm 0.5, 0)$, are shown in Fig. 7.2. Inspection of the momentum distribution of the spectral weight reveals

that the magnetic fluctuations underpinning the AF state at $T = 2.5$ K are quasi one-dimensional. Fig. 7.2 (a) demonstrates that the magnetic excitations along the in-plane K-axis, parallel to the short leg of the triangular lattice, show an anisotropy gap at the zone center and a well-defined dispersion; however, the magnon dispersion in directions orthogonal to this axis are diffuse. Specifically, the spin waves dispersing between the MnO_6 planes (along L) are dispersionless (see Fig. 7.3) as expected for the planar structure of α-$Na_{0.9}MnO_2$, and Fig. 7.2 (b) shows that spin wave energies dispersing perpendicular to the AF chain direction in the plane (along H) are only weakly momentum dependent. This demonstrates that the spin fluctuations exist as quasi-one-dimensional planes of scattering in ($\mathbf{Q}$, E) space, driven by the strong interchain frustration inherent to the lattice and consistent with the large magnetic frustration parameter of this compound [18].

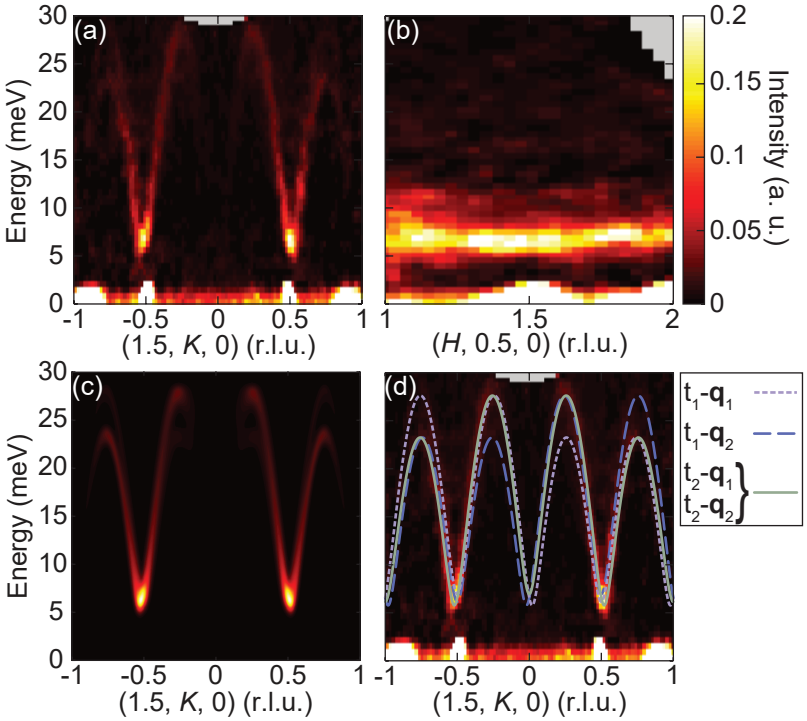

Figure 7.2: Magnon spectra at $T = 2.5$ K collected via time-of-flight neutron scattering measurements. Panel (a) shows the dispersion of magnons along the chain axis (K-direction) across the full bandwidth of excitations. Data was integrated across -0.1 to 0.1 along L and from 1.4 to 1.6 along H. Panel (b) shows the dispersion along the interchain axis (H-direction) with data integrated from -0.1 to 0.1 along L and from 0.48 to 0.52 along K. Panel (c) shows the simulated scattering intensities using the model fit to the data described in the main text and integrated over the same values as panel (a). Panel (d) shows the fit transverse modes from the four allowed domains generating the spectral weight in panel (c) and then overplotted with the raw data from panel (a).

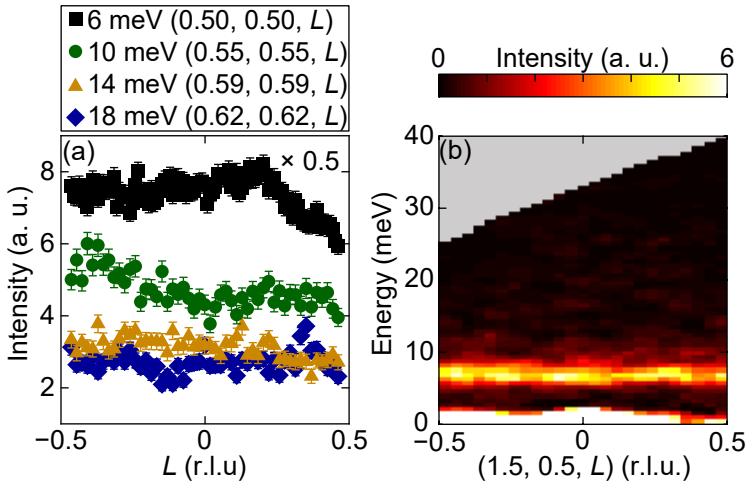

Figure 7.3: Dispersion of spin waves along the L-axis. (a) Momentum scans collected via triple-axis measurements at select energies at 2.5 K. Error bars represent one standard deviation. (b) L dependence of the zone center magnons measured via time-of-flight measurements at 4 K. Data has been integrated about the (1.5, 0.5, 0) magnetic zone center with widths H=[1.48, 1.52] and K=[0.48, 0.52].

As twin effects from both crystallographic and spin domains may obscure any subtle dispersion along H due to interchain interactions, inspection of zone boundary energies and analysis of the full bandwidth are necessary to quantify the weak interchain exchange terms. Therefore, in order to parameterize the dispersion measured in Fig. 7.2 (a), the high energy data were analyzed using a four-domain model (t_1-$\mathbf{q}_1$, t_1-$\mathbf{q}_2$, t_2-$\mathbf{q}_1$, t_2-$\mathbf{q}_2$) as well as by fitting lower energy triple-axis data shown in Fig. 7.4 and Fig. 7.5. The data were modeled using the single mode approximation and the spin Hamiltonian, $H = J_1 \sum_{nn} \mathbf{S}_i \cdot \mathbf{S}_j + J_2 \sum_{nnn} \mathbf{S}_i \cdot \mathbf{S}_j - D \sum_n (S_n^z)^2$, where J_1 is the twofold nearest-neighbor exchange coupling, J_2 is the fourfold next nearest neighbor coupling, and D is a uniaxial, Ising-like, single-ion anisotropy term. The dispersion relation generated from a linear spin wave analysis of this Hamiltonian is given by $E(\mathbf{Q}) = S\sqrt{\omega_\mathbf{Q}^2 - \lambda_\mathbf{Q}^2}$, where $\omega_\mathbf{Q} = 2(J_1 + D + J_2 \cos(\pi H + \pi K))$ and $\lambda_\mathbf{Q} = 2(J_1 \cos(2\pi K) + J_2 \cos(\pi H - \pi K))$ (see Supplementary Information in Ref. [19] for details on the derivation), and the results from fitting the data yielded a $J_1 = 6.16 \pm 0.01$ meV, $J_2 = 0.77 \pm 0.01$ meV, and $D = 0.215 \pm 0.001$ meV. These values are roughly consistent with earlier powder averaged measurements of spin dynamics in α-NaMnO$_2$, although these earlier measurements were not sensitive enough to resolve a J_2 term [12].

The magnon modes from the four-domain model are overplotted as lines with the raw time-of-flight data in Fig. 7.2 (d), and the total simulated intensities summed from

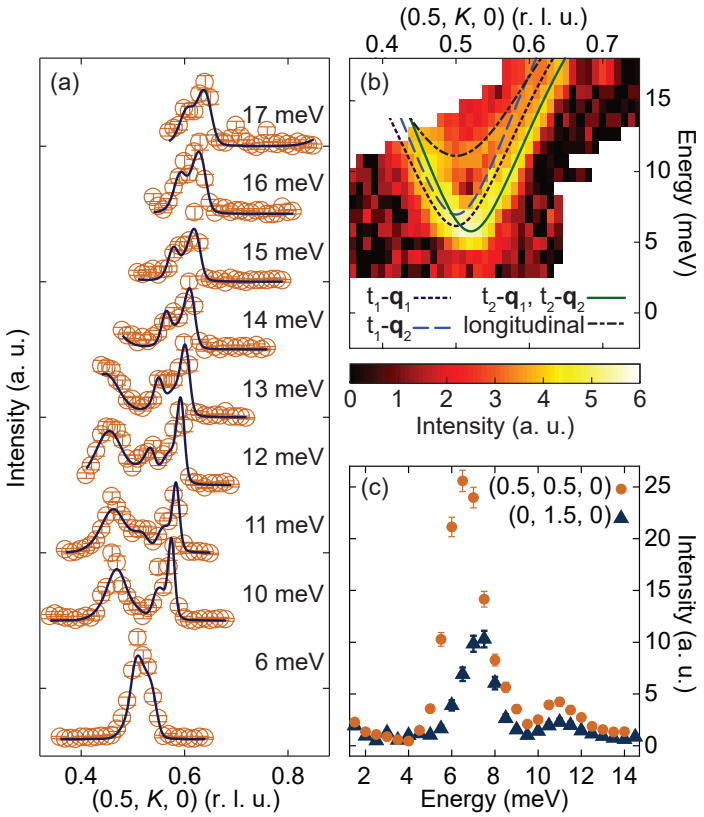

Figure 7.4: Inelastic neutron scattering data at $T = 2$ K revealing an additional zone center mode. Panel (a) shows momentum scans at various energies through $\mathbf{Q} = (0.5, 0.5, 0)$. Solid lines are resolution convolved fits to the data as described in the text. Panel (b) shows an intensity color map summarizing the scattering data from panel (a) along with dispersion of modes comprising the fits to the data in panel (a). Lines show fits to the expected transverse modes from the different crystallographic and magnetic domains within the sample: t_1-$\mathbf{q}_1$ (dashed purple), t_1-$\mathbf{q}_2$ (dashed blue), and t_2-$\mathbf{q}_1$ and t_2-$\mathbf{q}_2$ (solid green). The black dashed line represents the dispersion fit to the longitudinal mode in the spectrum as described in the text. Panel (c) shows constant energy scans at the three dimensional $(0.5, 0.5, 0)$ and quasi one-dimensional $(0, 0.5, 0)$ AF zone centers. Error bars in (a) and (c) represent one standard deviation.

all modes are shown in Fig. 7.2 (c). Good agreement is seen between the data in Fig. 7.2 (a) and the simulated intensities shown in Fig. 7.2 (c) and Fig. 7.6. To further illustrate this model at lower energies closer to the zone center gap value, data collected via a thermal triple-axis spectrometer are shown in Fig. 7.4. Momentum scans through the AF zone center are plotted in Fig. 7.4 (a) at energies from $\Delta E = 3$ meV to 18 meV with the resulting color map of intensities plotted in Fig. 7.4 (b). Magnon modes dispersing from the four domains in the system using the same J_1-J_2-D model described earlier and convolved with the instrument resolution function are plotted as solid lines fit to the data in Fig. 7.4 (a). Crucially, unlike the model presented in Fig. 7.2, describing this lower energy data also requires the introduction of one additional dispersive mode. This

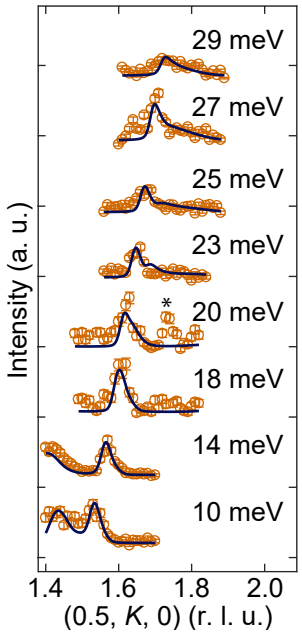

Figure 7.5: Higher energy triple-axis data collected about the (0.5, 1.5, 0) zone center at 4 K.. Data show momentum scans along the K-axis at various energies. Data at different energies are offset for clarity. Solid lines denote fits to the dispersion using the multidomain J_1-J_2-D model described in the main text. The star above the 20 meV data denotes a spurious background feature. Error bars represent one standard deviation.

mode is distinct from the transversely polarized magnons anticipated in this material, and it represents an unexpected longitudinally polarized bound state as described in the next section.

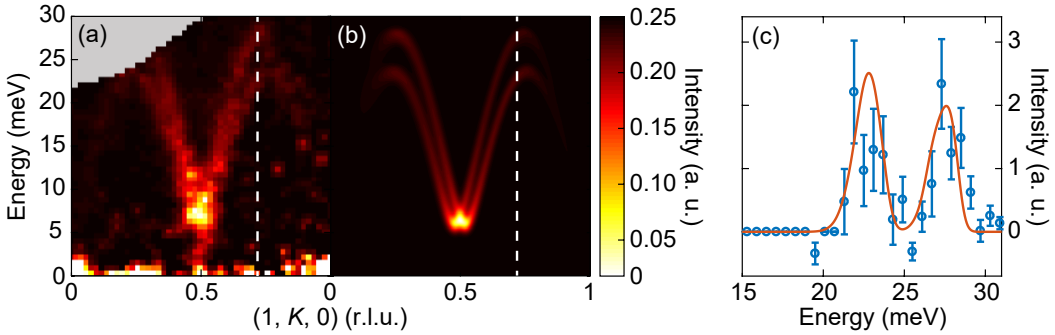

Figure 7.6: Spin wave spectra collected at 4 K via time-of-flight measurements compared with the J_1-J_2-D multidomain model. Panels (a), (b), and (c) show the map of scattering data about the zone center (1, 0.5, 0), modeled intensities, and a representative cut through the data and model respectively. The vertical dashed line denotes the position of the constant momentum cut through both the data and the multidomain model. In panels (a) and (b) intensities were integrated out of the plane through $0.9 < H < 1.1$ and $-0.1 < L < 0.1$. The cut in panel (c) was further integrated through $0.70 < K < 0.74$ The error bars in (c) represent one standard deviation.

7.2.3 Longitudinally polarized mode

To more clearly illustrate the appearance of an additional mode in the low energy spin dynamics, a magnetic zone center energy scan at $\mathbf{Q} = (0.5, 0.5, 0)$ is plotted in Fig. 7.4 (c). This scan shows the large buildup of spectral weight above the $\Delta E = 6.15 \pm 0.04$ meV zone center gap, consistent with the quasi one-dimensional magnon density of states, and above this gap a second zone center mode near 11 meV appears. This 11 meV mode is not accounted for by any of the expected transverse modes in this system, and it is also quasi one-dimensional in nature. Fig. 7.4 (c) demonstrates negligible interchain dispersion as $\mathbf{Q}$ is rotated from the three dimensional $\mathbf{Q} = (0.5, 0.5, 0)$ to one dimensional $\mathbf{Q} = (0, 0.5, 0)$ AF zone center, and the 11 meV mode's dispersion along the chain direction is plotted in Fig. 7.4 (b). While there is a limited bandwidth (ΔE = 11 meV to 15 meV) where this new mode remains resolvable inside of the dispersing transverse magnon branches, the narrow region of dispersion was empirically parameterized using a one dimensional J-D model with $H = J\sum_n \mathbf{S}_n \cdot \mathbf{S}_{n+1} - D\sum_n (S_n^z)^2$ and $E(\mathbf{Q}) = \sqrt{\Delta^2 + c^2 \sin^2(2\pi K)}$. The gap value from this parameterization was fit to be $\Delta E = 11.11 \pm 0.06$ meV and $c = 21.6 \pm 0.1$ meV. The dispersion fit to this higher energy mode along with the dispersions fit to the transverse magnon modes are overplotted with the data in Fig. 7.4 (b). We again note that this additional 11 meV dispersive mode was incorporated within the fits shown in Fig. 7.4 (a).

To further explore the origin of the anomalous 11 meV branch of excitations near the AF zone center, polarized neutron scattering measurements were performed using an experimental geometry that leveraged the quasi one-dimensional nature of the spin excitations. Specifically, magnetic excitations were measured about the one-dimensional zone center, $\mathbf{Q} = (0, 1.5, 0)$. As the magnetic moment $\boldsymbol{\mu}$ is oriented nearly parallel to the $[-1, 0, 1]$ crystallographic axis, two transversely polarized magnon modes along the $[1, 0, 1]$ and the [0, 1, 0] directions are expected in the ordered state, each carrying an oscillation of the orientation/phase of the staggered magnetization. The $(\mathbf{Q} \times \boldsymbol{\mu} \times \mathbf{Q})$ orientation factor in the neutron scattering cross section renders it only sensitive to the component of the moments' fluctuations perpendicular to $\mathbf{Q}$, and thus transverse spin waves observed at the $\mathbf{Q} = (0, 1.5, 0)$ are dominated by $[1, 0, 1]$ polarized modes. By further orienting the neutron's spin polarization, $\mathbf{P}$, parallel to $\mathbf{Q}$, all allowed magnetic

scattering is guaranteed to appear in the channel where the neutron's spin is flipped during the scattering process [20]. Fig. 7.7 (a) shows the results of energy scans collected at $\mathbf{Q} = (0, 1.5, 0)$ with data collected in both the spin-flip (SF) and non spin-flip (NSF) channels. As expected, peaks from the $\Delta E = 6.15$ and $\Delta E = 11.11$ meV zone center modes appear only in the SF cross sections (dashed lines indicate the transmission expected by the polarization efficiency of SF scattering into the NSF channel and vice versa).

Using the same scattering geometry but with the neutron polarization now rotated parallel to the $[-1, 0, 1]$ direction, the magnetic scattering processes polarized along the $[1, 0, 1]$ axis (i.e. the resolvable transverse spin wave mode) should remain in the SF channel while scattering processes polarized parallel to the neutron polarization direction (i.e. nearly parallel to the ordered moment direction) will instead appear in the NSF channel. Fig. 7.7 (b) shows the results of energy scans with $\mathbf{P} \parallel [-1, 0, 1]$ where the 11 meV mode now appears only in the NSF channel and the 6 meV mode remains only in the SF channel. Again, the small amount of intensity around 6 meV in the NSF channel can be explained by the calculated contamination of scattering from the SF channel into the NSF channel. This demonstrates that the 11 meV mode and the associated upper branch of spin excitations are polarized longitudinally, reflecting an amplitude mode of the staggered magnetization, while the 6 meV mode and the lower energy branch of excitations are polarized transverse to the moment direction. Keeping $\mathbf{P} \parallel [-1, 0, 1]$, an identical energy scan collected at $T = 50$ K in the paramagnetic state shows that the coherent amplitude mode vanishes for $T > T_{\mathrm{AF}}$ and critical fluctuations driving the phase transition dominate the longitudinal spin response (Fig. 7.7 (c)). Conversely, the transverse modes remain well defined at high temperatures, reflective of the strong, inherently one-dimensional coupling and the single-ion anisotropy of the Mn moments.

7.3 Discussion

Earlier neutron measurements have demonstrated that the ordered moment of α-NaMnO$_2$ (2.92 μ_{B}) is significantly reduced from the classical expectation (4 μ_{B}) [11], suggesting substantial fluctuation effects in this material. Additionally, ESR experiments

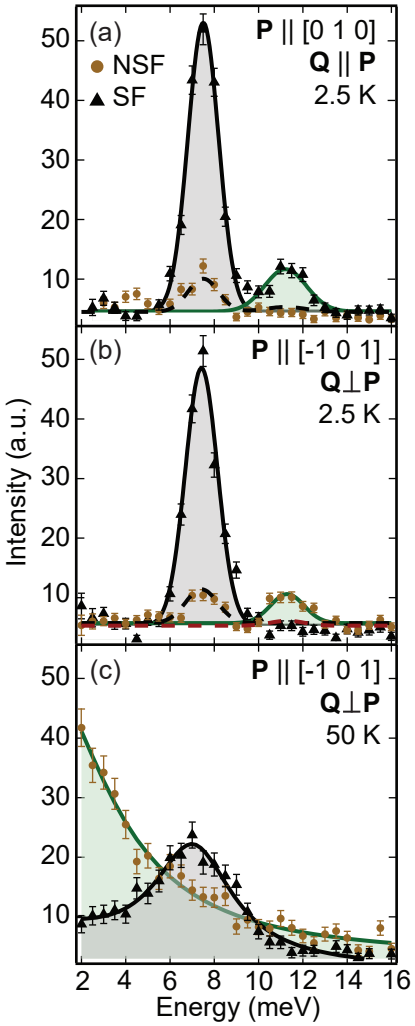

Figure 7.7: Polarized inelastic neutron scattering data about the quasi-1D zone center $\mathbf{Q} = (0, 1.5, 0)$. Panel (a) shows data collected with the neutron polarization $\mathbf{P}$ parallel to $\mathbf{Q}$. The two modes appear only in the spin-flip (SF) channel and so are both magnetic in origin. Panel (b) shows data collected with the neutron polarization $\mathbf{P}$ parallel to the $[-1, 0, 1]$ axis. Transverse spin fluctuations appear in the SF channel, and longitudinal fluctuations appear in the non spin-flip (NSF) channel. Data in both (a) and (b) were taken in the 3D ordered state at $T = 2.5$ K, and black dashed lines indicate the expected bleed through from the SF channel into the NSF channel due to imperfect neutron polarization. The red dashed line in (b) represents the expected bleed through from the NSF channel into the SF channel. Panel (c) shows the same configuration as (b) but above the antiferromagnetic transition temperature at $T = 50$ K. Solid lines in (a) and (b) are Gaussian fits parameterizing each mode. The solid line for the NSF channel in (c) is a Lorentzian fit centered at $\Delta E = 0$ meV and the solid line for the SF channel in (c) consists of two Lorentzian fits (one centered at $\Delta E = 0$ meV and one at the single magnon gap energy). Error bars represent one standard deviation.

find evidence of strong low temperature fluctuations in the ordered state [18]. The $\Delta S = S - \langle S_z \rangle = 0.54$ missing in the static ordered moment, however, can be accounted for when integrating the total inelastic spectral weight in earlier powder inelastic neutron measurements [12]. Neutron scattering sum rules therefore imply that the ratio of

the momentum and energy integrated weights of the longitudinal and transverse spin fluctuations should be $\frac{\Delta S(\Delta S+1)}{(S-\Delta S)(2\Delta S+1)} = 0.27$ [21], which is greater than the ratio of the intensities of the zone center modes $I_{\text{long}}/I_{\text{tran}} = 0.19$. This rough comparison suggests that, while the amplitude mode observed in our measurements is relatively intense, it remains within the bounds of the allowed spectral weight for longitudinal fluctuations.

Relative to stoichiometric α-NaMnO$_2$ powder samples, Na vacancies in the α-Na$_{0.9}$MnO$_2$ crystal studied here are unlikely to generate this long-lived, dispersive amplitude mode. Each Na vacancy naively binds to a hole on the Mn-planes and creates an Mn^{4+} $S = 3/2$ magnetic impurity. The corresponding hole is bound to the impurity site due to strong polaron trapping. As this state remains localized within the lattice [22, 23], the role of vacancies can be viewed as introducing random static magnetic impurities within the MnO$_6$ planes. Neither this random, static disorder nor the high density of twin boundaries inherent to the lattice [24] are capable of directly generating a coherent spin mode; however, they may indirectly contribute to destabilizing the ordered Néel state, pushing α-Na$_{0.9}$MnO$_2$ closer to a disordered regime and enhancing fluctuation effects.

For an easy-axis antiferromagnetic chain at 0 K, two degenerate, gapped transverse magnon modes are expected as Néel order sets in; however the amplitude mode observed in the ordered state of α-Na$_{0.9}$MnO$_2$ is unexpected. Since this longitudinally polarized mode has a zone center lifetime that is constrained by the resolution of the spectrometer ($\Delta E_{\text{res}} = 2.25$ meV at $E = 11$ meV) without an observable high energy tail and with an energy below twice the transverse modes' gap values, it likely arises as a long-lived two magnon bound state [25, 26]. The finite binding energy of this state as determined by $E_{\text{bind}} = 2E_{\text{gap}} - E_{\text{long}} = 1.2 \pm 0.1$ meV at the zone center $\mathbf{Q} = (0.5, 0.5, 0)$ implies an attractive potential between magnons once Néel order is established. To demonstrate the differences in the excitation energy and shape between the observed mode and that of a two-magnon continuum (i.e. no attractive potential), which arises through the interaction of two one-magnon excitations, the two-magnon continuum spectra for a 1D Heisenberg antiferromagnet with single-ion anisotropy was derived. The details can be found in Appendix C, and it is clear that the lowering of energy from that which is expected for a two-magnon continuum implies that the longitudinally polarized mode arises from a bound process.

To explore this further, we theoretically consider the existence of a bound state within a one-dimensional model, neglecting J_2. We further consider only zero temperature for simplicity, and perform a semi-classical large S analysis based on anharmonically coupled spin waves around an antiferromagnetically ordered state. For $J_1 e^{-S} \ll D \ll J_1$, and $S \gg 1$, the one-dimensional chain is ordered at $T = 0$, which allows J_2 to be neglected without qualitative errors. As detailed in the Supplementary Information of Ref. [19], the resulting description applies: (1) the anisotropy induces a single magnon gap $\Delta = 2S\sqrt{2J_1 D}$ so that the magnon dispersion near the magnetic zone center is that of a relativistic massive particle with $E = \sqrt{v^2k^2 + \Delta^2}$ with magnon velocity $v = 2J_1 S$, and (2) the dominant interaction between opposite spin magnons with momentum $k \ll \sqrt{\frac{D}{J_1}}$ is an attractive delta-function of strength $U = -2J_1$. This problem has a bound state which is in the non-relativistic limit described by two one dimensional particles of mass $M = \frac{\Delta}{v^2}$, for which the textbook result for the binding energy is $E_{\text{bind}} = \frac{MU^2}{4}$. Using the values above, we obtain $\frac{E_{\text{bind}}}{\Delta} = \frac{1}{4S^2}$. This is the leading result for large S, and in the limit $D/J_1 \ll 1$. While this limit predicts a binding energy approximately 3 times smaller than that observed for α-$Na_{0.9}MnO_2$, moving away from this limit and incorporating the non-negligible D in the system can account for this discrepancy. We note that, while we performed calculations in the one-dimensional model for simplicity, this is only a matter of convenience rather than essential physics: the magnons and their dispersion and interactions evolve smoothly upon including J_2, which would be necessary to model the spectrum at $T > 0$.

The long-lived amplitude mode in the Néel state of α-$Na_{0.9}MnO_2$ is distinct from those observed in canonical 1D integer spin chain systems such as $CsNiCl_3$ [4], where the longitudinal mode emerges as the Haldane triplet state splits due to an internal staggered mean field. The Haldane state within the frustration-driven $S = 2$ spin chains in α-$Na_{0.9}MnO_2$ is easily quenched under small anisotropy [13, 27, 28], and α-$Na_{0.9}MnO_2$ is thought to be outside of the Haldane regime. Calculations predict that the phase boundary between the $S = 2$ Haldane state and antiferromagnetic order appears at $D/J = 0.0046$ (for easy-axis D) [28], far away from the experimentally measured $D/J = 0.035$ in α-$Na_{0.9}MnO_2$. While amplitude modes in other quantum spin systems close to singlet instabilities have also been recently reported in the quasi-

two-dimensional spin ladder compound $C_9H_{18}N_2CuBr_4$ [29] and the two-dimensional ruthenate Ca_2RuO_4 [30], the formation of a longitudinal bound state in α-$Na_{0.9}MnO_2$ is distinct from modes in these and other $S = 1/2$ spin chain systems possessing substantial zero-point fluctuations [8].

Instead, in α-$Na_{0.9}MnO_2$, the interplay of geometric frustration and the Jahn-Teller quenching of orbital degeneracy uniquely conspire to create a quasi-one-dimensional magnon spectrum that condenses due to the attractive potential provided by an Ising-like single-ion anisotropy. As a result, α-$Na_{0.9}MnO_2$ provides an intriguing route to realizing an intense, stable amplitude mode in a planar AF. The dimensionality reduction realized within its chemically two-dimensional lattice also suggests that other α-$NaFeO_2$ type transition metal oxides [31, 32], possessing coherent Jahn-Teller distortions may host similarly stable amplitude modes, depending on their inherent anisotropies. More broadly this class of materials presents an exciting platform for exploring unconventional bound states such as bound soliton modes [14] stabilized in a quasi-one-dimensional spin setting.

7.4 Methods

7.4.1 Crystal growth and characterization

Na_2CO_3 and $MnCO_3$ powders (1:1 ratio plus 10% weight excess of Na_2CO_3) were mixed and sintered in an alumina crucible at 350 °C for 15 hours, reground and sintered for an additional 15 hours at 750 °C. Dense polycrystalline rods were made by pressing the powder at 50,000 psi in an isostatic press. The rod was sintered in a vertical furnace at 1000 °C for 15 hours and then quenched in air, before being transferred to a four mirror optical floating zone furnace outfitted with 500 W halogen lamps. The crystals were grown at a rate of 20 mm hr^{-1} in a 4:1 Ar:O_2 environment under 0.15 MPa of pressure. Inductively coupled plasma atomic emission spectroscopy (ICP-AES) was used to determine the Na/Mn ratio and to check that the expected mass of Mn was present. The ratio of Mn^{3+}/Mn^{4+} was determined through X-ray absorption near edge spectroscopy (XANES), X-ray photoelectron spectroscopy (XPS), and ^{23}Na solid-state NMR (ssNMR). Detailed crystal growth and characterization can be found in Dally, R.

et al [24]. Samples were handled as air-sensitive and stored in an inert environment. Time outside of an inert environment was minimized (e.g. during crystal alignment for neutron scattering experiments). The crystal faces are flat, and no degradation of the surface was observed during alignment. The same ≈0.5 g crystal was used for both neutron TOF and triple-axis experiments.

7.4.2 Time-of-flight experimental setup

Neutron time-of-flight data in Fig. 7.2 and Figs. 7.3 (b) and Fig. 7.6 were taken at the Spallation Neutron Source at Oak Ridge National Laboratory using the instrument SEQUOIA. The sample was sealed in a He-gas environment, mounted in a cryostat, and aligned in the (H, K, 0) horizontal scattering plane. All data were taken at 4 K with an incident energy $E_\mathrm{i} = 60$ meV and the fine-resolution fermi chopper rotating at 420 Hz. For data collection, the sample was rotated through a range of 180° with 1° steps. A background scan was collected by removing the sample from the neutron beam and collecting the scattering from the empty can.

7.4.3 Time-of-flight data analysis

An aluminum only (empty can) background was subtracted from all data before plotting. SpinW [33], a Matlab library, was used to simulate the magnetic excitations for the TOF data. Given the spin Hamiltonian, magnetic structure and twinning mechanisms (structural and magnetic), SpinW uses linear spin wave theory to numerically calculate and display the dispersion. The simulation was convolved with the energy resolution function of the neutron spectrometer ($E_\mathrm{i} = 60$ meV, $F_\mathrm{chopper} = 420$ Hz). Simulations for Fig. 7.2 (c) were run over the same range that the data were binned for Fig. 7.2 (a) and (d) (i.e. $1.4 < H < 1.6$ and $-0.1 < L < 0.1$), and then averaged together.

7.4.4 Triple-axis experimental setup

Triple-axis neutron data were taken with the instrument, BT7 [34, 35], at NCNR with a PG(002) vertically focused monochromator and the horizontally flat focus mode of the PG analyzer system. PG filters before and after the sample were used during collection of elastic data ($E_\mathrm{i} = 14.7$ meV), and only a PG filter after the sample was used during

inelastic operation (fixed $E_f = 14.7$ meV). Unpolarized data from Fig. 7.4 and Fig. 7.5 were taken with open$-25' - 50' - 120'$ collimations (denoting the collimation before the monochromator, sample, analyzer, and detector, respectively), and the sample was aligned in the (H, K, 0) scattering plane. Fig. 7.3 (a) data were unpolarized and taken with open$-50' - 50' - 120'$ collimators in the (H, H, L) plane. Polarized data in Fig. 7.1 (c) were taken with open$-25' - 25' - 120'$ collimation in the (H, K, 0) scattering plane. Polarized data in Fig. 7.7 were taken in the (H, K, H) plane with open$-80' - 80' - 120'$ collimations.

7.4.5 Triple-axis polarization efficiency corrections

It was determined that only two (one NSF and one SF) of the available four neutron scattering cross sections were needed for polarization analysis. Flipping ratios were taken throughout the experiment at the (2, 0, 0) nuclear Bragg peak and at all temperatures probed. These flipping ratios were used to correct for the polarization efficiency.

7.4.6 Triple-axis data analysis

All data were normalized to the neutron monitor counts, M. Error bars represent one standard deviation of the data. For unpolarized data, this was calculated by the square root of the number of observations, $\sqrt{N}$, where N is the number of observations. The lower monitor counts in polarized data were considered by propagating the error in the monitor counts, $\sqrt{M}$, such that $\sigma^2 = \frac{N}{M^2}(1 + \frac{N}{M})$. The determination of the moment angle utilized the polarized elastic data shown in Fig. 7.1 (c). After correcting for the polarization efficiency, the integrated intensities of the NSF and SF peaks were found by fitting the data to Gaussian functions. These intensities were used to find the moment angle following the technique in Moon, R. W. et al [20].

Fits to the constant energy scans (unpolarized inelastic neutron scattering data) in Fig. 7.2 (d), Fig. 7.4 (a), (b) and Fig. 7.5 used the Cooper-Nathans approximation [36] in ResLib [37], a program that calculates the convolution of the spectrometer resolution function with a user supplied cross section. The cross section used for the transverse excitation was the single-mode approximation of a two-dimensional spin lattice with single-ion anisotropy. Cross-sections for t_1-$\mathbf{q}_1$, t_1-$\mathbf{q}_2$, t_2-$\mathbf{q}_1$ and t_2-

$\mathbf{q}_2$ were all included during the fitting routine using the relation between the first moment sum rule and the dynamical structure factor, $\int_{-\infty}^{\infty}(\hbar\omega)S^{\alpha\alpha}(\mathbf{q},\hbar\omega)d(\hbar\omega) = -\sum_{n,\beta} J_n[1-\cos(\mathbf{q}\cdot\mathbf{a}_n)](1-\delta_{\alpha\beta})\left\langle\left\langle S^{\beta}_{\mathbf{R}_j}, S^{\beta}_{\mathbf{R}_j+\mathbf{a}_n}\right\rangle\right\rangle$. The contribution to the scaling factor from the single-ion term is small [38], and therefore, was not included. The longitudinal excitation was empirically fit using the single mode approximation for a one-dimensional chain, given its unresolvable dispersion along *H*. The longitudinal mode gap was determined by fitting the data in the range where it was resolvable (below 18 meV). This gap value was fixed and the fitting routine was run again, allowing all other parameters to vary. A single intrinsic HWHM for all excitations was refined during fitting and refined to be negligibly small. Additionally, a scaling prefactor was also refined for each crystallographic twin, where the two magnetic domains within a crystallographic twin were assumed to have the same weight (i.e. t_1-$\mathbf{q}_1$ and t_1-$\mathbf{q}_2$ had the same prefactor).

Polarized inelastic neutron data in Fig. 7.7 are plotted as raw data, uncorrected for polarization efficiency. The dashed lines representing the expected bleed through from the SF channel into the NSF channel in (a) and (b) were determined from the measured flipping ratio.

Acknowledgments

S.D.W. and R.L.D. gratefully acknowledge support from DOE, Office of Science, Basic Energy Sciences under Award DE-SC0017752. Work by L.B. was supported by the DOE, Office of Science, Basic Energy Sciences under Award No. DE-FG02-08ER46524.

References

[1] Pekker, D. & Varma, C. M. Amplitude/higgs modes in condensed matter physics. *Annu. Rev. Conden. Mater. Phys.* **6** (2015).

[2] Morra, R. M., Buyers, W. J. L., Armstrong, R. L. & Hirakawa, K. Spin dynamics and the Haldane gap in the spin-1 quasi-one-dimensional antiferromagnet $CsNiCl_3$. *Phys. Rev. B* **38** (1988).

[3] Raymond, S. Polarized-neutron observation of longitudinal haldane-gap excitations in Nd_2BaNiO_5. *Phys. Rev. Lett.* **82** (1999).

[4] Enderle, M., Tun, Z., Buyers, W. J. L. & Steiner, M. Longitudinal spin fluctuations of coupled integer-spin chains: haldane triplet dynamics in the ordered phase of $CsNiCl_3$. *Phys. Rev. B* **59** (1999).

[5] Grenier, B. Longitudinal and transverse Zeeman ladders in the Ising-like chain antiferromagnet $BaCo_2V_2O_8$. *Phys. Rev. Lett.* **114** (2015).

[6] Rüegg, C. h. Quantum magnets under pressure: controlling elementary excitations in $TlCuCl_3$. *Phys. Rev. Lett.* **100** (2008).

[7] Merchant, P. Quantum and classical criticality in a dimerized quantum antiferromagnet. *Nat. Phys.* **10** (2014).

[8] Lake, B., Tennant, D. A. & Nagler, S. E. Novel longitudinal mode in the coupled quantum chain compound $KCuF_3$. *Phys. Rev. Lett.* **85** (2000).

[9] Zheludev, A., Kakurai, K., Masuda, T., Uchinokura, K. & Nakajima, K. Dominance of the excitation continuum in the longitudinal spectrum of weakly coupled heisenberg s=1/2 chains. *Phys. Rev. Lett.* **89** (2002).

[10] Coldea, R., Tennant, D. A., Tsvelik, A. M. & Tylczynski, Z. Experimental realization of a 2d fractional quantum spin liquid. *Phys. Rev. Lett.* **86** (2001).

[11] Giot, M. Magnetoelastic coupling and symmetry breaking in the frustrated antiferromagnet α-$NaMnO_2$. *Phys. Rev. Lett.* **99** (2007).

[12] Stock, C. One-dimensional magnetic fluctuations in the Spin-2 triangular lattice α-$NaMnO_2$. *Phys. Rev. Lett.* **103** (2009).

[13] Schollwöck, U. and Jolicoeur, T. Haldane gap and hidden order in the S=2 antiferromagnetic quantum spin chain. *Europhys. Lett.* **30** (1995).

[14] Haldane, F. D. M. Continuum dynamics of the 1-D Heisenberg antiferromagnet: identification with the O(3) nonlinear sigma model. *Phys. Lett. A* **93** (1983).

[15] Haldane, F. D. M. Nonlinear field theory of large-spin heisenberg antiferromagnets: semiclassically quantized solitons of the one-dimensional easy-Axis Néel state. *Phys. Rev. Lett.* **50** (1983).

[16] Abakumov, A. M., Tsirlin, A. A., Bakaimi, I., Tendeloo, G. & Lappas, A. Multiple twinning as a structure directing mechanism in layered rock-salt-type oxides: $NaMnO_2$ polymorphism, redox potentials, and magnetism. *Chem. Mater.* **26** (2014).

[17] Zorko, A., Adamopoulos, O., Komelj, M., Arcon, D. & Lappas, A. Frustration-induced nanometre-scale inhomogeneity in a triangular antiferromagnet. *Nat. Commun.* **5** (2014).

[18] Zorko, A. Magnetic interactions in α-$NaMnO_2$: quantum spin-2 system on a spatially anisotropic two-dimensional triangular lattice. *Phys. Rev. B* **77** (2008).

[19] Dally, R. L. *et al.* Amplitude mode in the planar triangular antiferromagnet $Na_{0.9}MnO_2$. *Nat. Commun.* **9**, 2188 (2018).

[20] Moon, R. M., Riste, T. & Koehler, W. C. Polarization analysis of thermal-neutron scattering. *Phys. Rev.* **181** (1969).

[21] Huberman, T. Two-magnon excitations observed by neutron scattering in the two-dimensional spin-5/2 Heisenberg antiferromagnet Rb_2MnF_4. *Phys. Rev. B* **72** (2005).

[22] Ma, X., Chen, H. & Ceder, G. Electrochemical properties of monoclinic $NaMnO_2$. *J. Electrochem. Soc.* **158** (2011).

[23] Jia, T. Magnetic frustration in α-$NaMnO_2$ and $CuMnO_2$. *J. Appl. Phys.* **109** (2011).

[24] Dally, R. Floating zone growth of α-$Na_{0.90}MnO_2$ single crystals. *J. Cryst. Growth* **459** (2017).

[25] Xian, Y. Longitudinal excitations in quantum antiferromagnets. *J. Phys. Condens. Mat.* **23** (2011).

[26] Heilmann, I. U. One- and two-magnon excitations in a one-dimensional antiferromagnet in a magnetic field. *Phys. Rev. B* **24** (1981).

[27] Schollwöck, U. and Golinelli, O. and Jolicoeur, T. S=2 antiferromagnetic quantum spin chain. *Phys. Rev. B* **54** (1996).

[28] Kjäll, J. A. and Zaletel, M. P. and Mong, R. S. K. and Bardarson, J. H. and Pollmann, F. Phase diagram of the anisotropic spin-2 xxz model: Infinite-system density matrix renormalization group study. *Phys. Rev. B* **87** (2013).

[29] Hong, T. Higgs amplitude mode in a two-dimensional quantum antiferromagnet near the quantum critical point. *Nat. Phys.* **13** (2017).

[30] Jain, A. Higgs mode and its decay in a two-dimensional antiferromagnet. *Nat. Phys.* **13** (2017).

[31] Mostovoy, M. V. & Khomskii, D. I. Orbital ordering in frustrated Jahn-Teller systems with 90° exchange. *Phys. Rev. Lett.* **89** (2002).

[32] McQueen, T. Magnetic structure and properties of the S=5/2 triangular antiferromagnet α-$NaFeO_2$. *Phys. Rev. B* **76** (2007).

[33] Toth, S. & Lake, B. Linear spin wave theory for single-q incommensurate magnetic structures. (2015).

[34] Lynn, J. W. Double focusing thermal triple axis spectrometer at the ncnr. *J. Res. Natl Inst. Stan.* **117** (2012).

[35] Chen, W. C. ^{3}He neutron spin filters for a thermal neutron triple axis spectrometer. *Phys. B* **397** (2007).

[36] Cooper, M. J. & Nathans, R. The resolution function in neutron diffractometry. i. the resolution function of a neutron diffractometer and its application to phonon measurements. *Acta Crystallogr.* **23** (1967).

[37] Zheludev, A. Reslib (eth zürich) (2009).

[38] Zaliznyak, I. & Lee, S.-H. *Modern Techniques for Characterizing Magnetic Materials* (Springer, Heidelberg, 2005). Edited by Y. Zhu.

Appendix A

Basics of muon spin relaxation (μSR)

μSR is short for muon spin rotation, relaxation or resonance, each denoting a different technique that involves implanting muons into a material in order to probe information about the local magnetism. The discussion here will focus on muon spin relaxation as this was the method used in Ch. 4 for $Na_4Ir_3O_8$. The muon is often referred to as a heavy electron: it is an elementary particle with spin-1/2 and charge $\pm 1e$, but with a mass of $207m_e$. The positive muon, μ^+, is more commonly used for probing condensed matter physics, and the superscript will be dropped from here on out [1].

The production of muons at the Swiss Muon Source (SμS) at the Paul Scherrer Institut starts with a proton accelerator and uses spallation to provide a continuous beam of muons to the instruments (as opposed to a pulsed source). Protons are guided to carbon targets where the collision with the carbon nuclei produces pions, which collect on the target (due to energy/momentum conservation of the collision). The pions decay after 26 ns into a muon and a neutrino, which fly apart in opposite directions. Muons produced in this manner have the property that their spins will point opposite of their momentum, and because the muons are all leaving with the same momentum, they are all polarized in the same direction [2]. The muon polarization can be preserved on its path to the sample via guide fields, much like in polarized neutron scattering. Unlike neutron scattering, μSR is not a scattering technique. Muons are easily stopped, and when directed towards a sample, they implant at interstitial sites. While in the sample, the muon is sensitive to the local magnetic field around it; for example, they may depolarize uniformly to precess about a static net field, like in a ferromagnet, or they may depolarize due to magnetic fluctuations. The average lifetime of a muon is 2.2 μs, at which point it decays into a positron and two neutrinos (which don't interact with the sample). The positron has a high enough energy to be ejected from the sample and is emitted preferentially in the direction of the muons' spin at the time of its decay, and it is the positron that gets detected in a μSR experiment. Detectors surround the sample, so where the positron gets detected will give information about the momentum of the positron, and therefore the spin of the muon at the time of its decay. The emission of the positron along the muon spin direction is only preferential, and the angular distribution of the positron intensity is,

$$P(\theta) = 1 + a\cos\theta. \tag{A.1}$$

Positrons with different energies yield different values of the asymmetry parameter, a, in Eq. A.1. The highest energy positrons give a value of $a = 1$, but averaged over all positrons, the value of $a = 1/3$. The spatial distribution can be visualized in Fig. A.1. Eq. A.1 can be thought of as the probability that a positron emitted from a muon will be along some direction defined by an angle, θ, with respect to the muon spin.

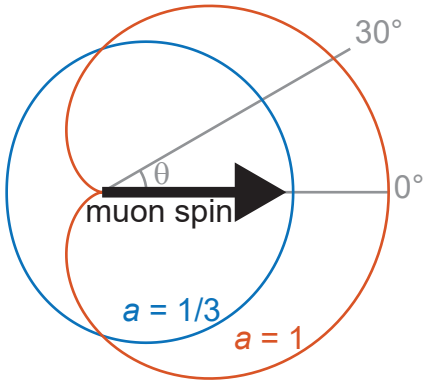

Figure A.1: The probability distribution of the direction for positron emission, $P(\theta)$, from muon decay, following the relation $P(\theta) = 1 + a\cos\theta$.

The muon precesses in the presence of a magnetic field at an angular frequency of $\omega_\mu = \gamma_\mu B$, where $\gamma_\mu = \frac{ge}{2m_\mu}$ is the muon gyromagnetic ratio. Because of the distribution of muon lifetimes, not all muons are able to make full rotations around a net field within a sample. This is the basis for another asymmetry parameter, $A(t)$, not to be confused with the positron asymmetry, a, which is determined using detectors which are positioned on opposite sides of the sample. On GPS, the instrument used for Ch. 4, there are six detectors: forward, backward, top, bottom, left, and right. A schematic of the zero-field experimental setup showing just the forward and backward detectors is shown in Fig. A.2, which was recreated from Ref. [1].

When a muon first implants in a sample, it may decay so quickly that it does not have time to be depolarized from its local field, and it will hit the backward detector. If the muon doesn't decay right away, it may depolarize and precess enough around its local field so that its spin is pointed towards the forward detector. If this is when the

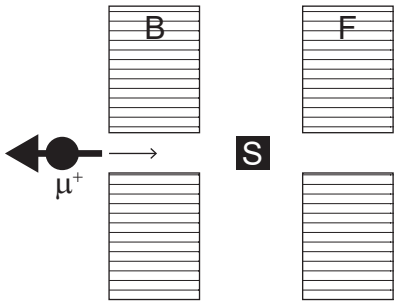

Figure A.2: Zero-field μSR geometry with the forward and backward detectors labeled B and F, respectively. The sample is denoted by the black square labeled S.

muon decays, then the positron will be detected at the forward detector. The number of positrons hitting the backward detector with respect to time is some function, $N_B(t)$, and the number of positrons hitting the forward detector is some function $N_F(t)$. Clearly, a sophisticated timing system must be in place to determine the time from which the muon is implanted in the sample to the time it hits the detector. At a continuous muon source, only one muon at a time can be processed. A timer starts when the muon gets to the sample, and is clocked when it reaches the detector. If in that time, another muon has entered the sample, both muons must be disregarded. The normalized difference between $N_B(t)$ and $N_F(t)$ tells the experimenter about the time evolution of the muon polarization and defines the asymmetry,

$$A(t) = \frac{N_B(t) - N_F(t)}{N_B(t) + N_F(t)} = a_0 P_\alpha(t), \tag{A.2}$$

where $P(t)$ is the muon depolarization function, which is dependent on the magnetism in the sample and theoretically, $a_0 = a = 1/3$ (in reality, a_0 ends up being ≈ 0.25, and is determined for an instrument at the beginning of an experiment and typically held constant throughout analysis). At $t = 0$, $P(0) \approx 1$ because the beam is fully polarized. We can define another function, $G(t)$, which is the normalized muon spin autocorrelation function, $G(t) = P(t)/P(0)$, commonly referred to as the muon depolarization function. The goal of an experiment is to find the function, $G(t)$, because the form of the function indicates the magnetic phenomena inside the sample. First, one collects data to find the asymmetry function, Eq. A.2. The depolarization function can be calculated from more than just the set of forward and backward detectors, and

in fact, should be written as $P_\alpha(t)$, where α are the Cartesian x, y, and z coordinates, where z is taken to be along the external field. For a transverse field setup, $P_x(t)$ and $P_y(t)$ are the functions of interest, and for a zero-field or longitudinal field setup (where the external field is along the muon polarization direction), $P_z(t)$ is of interest. The concept of μSR is based on what happens when a polarized muons implant in a sample with a static field (no external field). All the muons will precess about the the static field, which is oriented at an angle θ from the muon polarization. The muons will decay at different points during the precession process, and the time-dependent evolution of the muon depolarization will be,

$$P_\alpha(t) = \cos^2\theta + \sin^2\theta\cos\left(\omega_\mu t\right). \tag{A.3}$$

For this experimental geometry, $P_z(t)$ is the function of interest, and for a polycrystalline sample, a spatial average of Eq. A.3 is taken, which yields,

$$P_z(t) = \frac{1}{3} + \frac{2}{3}\cos\left(\omega_\mu t\right). \tag{A.4}$$

The oscillating component in Eq. A.4 reflects the long-range magnetic order in the sample. If the magnetic order is disordered, the local field will not be uniform throughout the sample, and the oscillations will be damped. If a magnetic phase transition lacks long-range order, there will be no oscillating component. In the case of densely packed static nuclear moments, with no net polarization (like atoms in a lattice), the zero-field depolarization function is the Gaussian Kubo-Toyabe from Eq. 4.1 in Ch. 4. The presence of static short-range magnetic order can lead to much more complicated depolarization functions. The Gaussian-broadened Gaussian (GbG) function, Eq. 4.3 in Ch. 4, is an example of this, and describes disordered static moments with short-range correlations.

As discussed, the muon depolarization seen in a zero-field experiment can be due to the static distribution of internal fields, but it can also come from fluctuating magnetic moments. The form of the depolarization from fast fluctuating moments takes on the

form of an exponential,

$$G(t) = e^{-\lambda t}, \tag{A.5}$$

where λ is proportional to the characteristic fluctuation time. This is characteristic of paramagnents like $Na_3Ir_3O_8$. The modified GbG function for $Na_4Ir_3O_8$ also has an exponential, but the physics is due to slow fluctuations. Long time-scale fluctuations take on the form of a Lorentzian Kubo-Toyabe [3], however, and when slow on the time scale of the muon probe, the function cannot be distinguished from an exponential.

In a zero-field experiment, one cannot be absolutely sure of the mechanism of muon depolarization, and longitudinal field experiments are utilized to fully characterize quasi-static processes [4]. In a longitudinal field experiment, an applied external field along the muon polarization direction can be strong enough to overwhelm any static local fields, and the field at which this occurs can be used to determine the mean field strength. The applied field can then decouple the muon from the those internal fields, because for dynamic internal fields, the depolarization function is nearly field independent. This is why the lifting of the "1/3" tail in Ch. 4 under an applied field, and subsequent changes to the depolarization function with higher fields indicates the sample is mostly static (quasi-static) except for the slow timescale fluctuations.

References

[1] Blundell, S. J. Spin-polarized muons in condensed matter physics. *Contemporary Physics* **40**, 175–192 (1999).

[2] Cox, S. F. J. Implanted muon studies in condensed matter science. *Journal of Physics C: Solid State Physics* **20**, 3187 (1987).

[3] Kubo, R. A stochastic theory of spin relaxation. *Hyperfine Interactions* **8**, 731–738 (1981).

[4] de Réotier, P. D. & Yaouanc, A. Muon spin rotation and relaxation in magnetic materials. *Journal of Physics: Condensed Matter* **9**, 9113 (1997).

Appendix B

Stacking faults in α-$NaMnO_2$: FAULTS simulations

B.1 Understanding the effects of α-NaMnO$_2$ fault defects in neutron data

The discussion leading to Eq. 2.6 in Ch. 2 had assumed a perfect crystal with the only displacements from equilibrium being due to the Debye-Waller factor. The Debye-Waller factor quantifies displacements from the thermal motion of atoms about their equilibrium positions, but can also take into account very small displacements from natural crystalline disorder. It is worth mentioning that greater disorder within a crystalline structure, such as the presence of twin boundaries and stacking faults, requires modification to the model. α-NaMnO$_2$ has a faulted structure, and the nuclear scattering structure factors do not match up well with those calculated for a pristine crystal. Crystals with stacking faults have long-range periodicity in two-dimensions, with disorder along the third.

Ref. [1] created a mathematical model to simulate the diffracted intensities of faulted structures. Instead of using an atomic density operator which describes the electron density at any given point in three-dimensions, they used a summation of two-dimensional electron density operators, which are offset along the stacking direction. For each unique layer, $i, j, k, l, ...$, the density can be described about an arbitrary origin, $\mathbf{r}$, and the vector connecting two local layer origins is $\mathbf{R}_{ij}$. The probability of one layer following another layer is α_{ij}. The total potential for N layers can be written as,

$$V(\mathbf{r})^{(N)}_{ijkl...} = \rho_i(\mathbf{r}) + \rho_j(\mathbf{r}-\mathbf{R}_{ij}) + \rho_k(\mathbf{r}-\mathbf{R}_{ij}-\mathbf{R}_{jk}) + \rho_l(\mathbf{r}-\mathbf{R}_{ij}-\mathbf{R}_{jk}-\mathbf{R}_{kl}) + ..., \quad \text{(B.1)}$$

The scattering amplitude, $\phi^{(N)}_{ijkl}(\mathbf{Q})$, is the Fourier transform of Eq. B.1,

$$\phi^{(N)}_{ijkl}(\mathbf{Q}) = F_i(\mathbf{Q}) + F_j(\mathbf{Q})e^{-i\mathbf{Q}\cdot\mathbf{R_{ij}}} + F_k(\mathbf{Q})e^{-i\mathbf{Q}\cdot(\mathbf{R_{ij}}+\mathbf{R_{jk}})} + F_l(\mathbf{Q})e^{-i\mathbf{Q}\cdot(\mathbf{R_{ij}}+\mathbf{R_{jk}}+\mathbf{R_{kl}})} + ..., \quad \text{(B.2)}$$

where $F_i(\mathbf{Q})$ is the form factor for the specified layer, i. One can see that for N layers, all of type i, the form factor for the three-dimensionally ordered lattice is

recovered. From here, the reader is referred to Ref. [1] for more details. We can see that this new density operator describes how the deviation from perfect layering will affect and redistribute the intensities in a diffraction pattern to give incoherent contributions because the nuclear potential is no longer a delta function. Additionally, twin boundaries can cause broadening about a Bragg position, and deformations can cause shifting of peak off from the integer hkl positions [2]. Treacy et al. used these calculations to create the simulation program DIFFaX, which is now implemented into a refinement program, FAULTS [3]. This program was used to understand how the fault defects in α-NaMnO$_2$ change neutron diffraction patterns from the ideal. For α-NaMnO$_2$, the disordered direction is $[-1, 0, 1]$, and the ordered plane is defined by the $[0, 1, 0]$ and $[1, 0, 1]$ directions. Fig. B.1 (a) shows a default-free unit cell oriented such that the $[-1, 0, 1]$ is vertical and aligned with a Cartesian z-axis as defined in the figure.

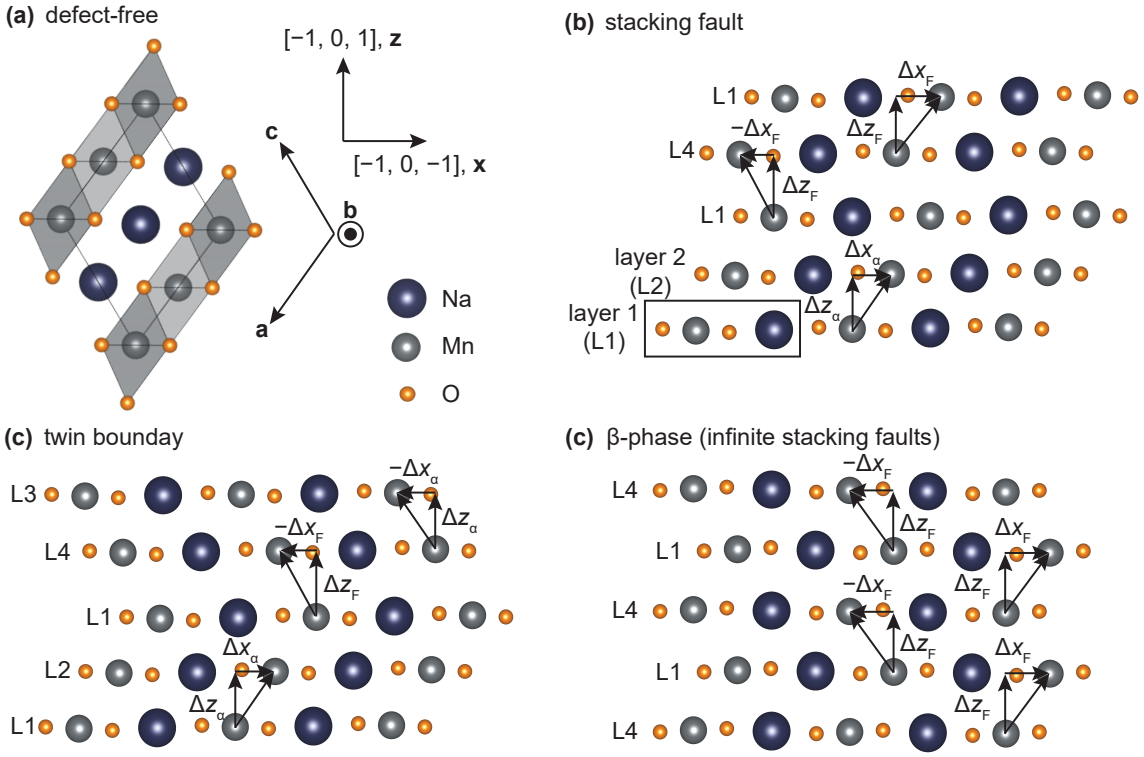

Figure B.1: (a) The defect-free α-NaMnO$_2$ crystal with the relationship between the standard unit cell and the Cartesian coordinate system used in the other panels. (b) Stacking fault defect, where the repeating unit which defines the layers is outlined in black. (c) Twin boundary defect. (d) Infinite density of stacking fault defects, which recreates the beta-phase crystal structure.

Fig. B.1 (b) defines four layer types, each based on the four-atom unit outlined in black. This unit repeats infinitely along the x- and y-axes. Layer 2 (L2) is offset from Layer 1 (L1) along the b-axis by $\frac{1}{2}\mathbf{b}$, so that in going from L1 to L2 only translations along

x and z are needed. The ideal crystal alternates between L1 and L2 with a translation of $\Delta x_\alpha \hat{\mathbf{x}} + \Delta z_\alpha \hat{\mathbf{z}}$ between each layer. Layer 3 (L3) = L1 and Layer 4 (L4) = L2, and only transitions between layers with an offset along the b-axis are allowed (i.e. L1 to L2 or L4, L3 to L2 or L4, etc.). L3 and L4 are reserved for when a layer shifts in the negative x-direction (where the total translation is $-\Delta x_F \hat{\mathbf{x}} + \Delta z_F \hat{\mathbf{z}}$). Alternating between L3 and L4 continuously represents the ideal structure for the twin if $|\Delta x_F| = |\Delta x_\alpha|$ and $\Delta z_F = \Delta z_\alpha$. The defect pattern in Fig. B.1 (b) is of the stacking fault variety, because after the initial fault in the negative x-direction (L1 to L4), the structure faults back to the ideal structure. Fig. B.1 (c) shows a twin boundary defect, where after an initial fault (L1 to L4), the structure continues stacking with translations in the negative x-direction. Lastly, Fig. B.1 (d) represents an infinite density of faults (which could also be represented by alternating L2 and L3 layers), which matches the layering pattern of the β-phase $NaMnO_2$ polymorph. The different possible layer transitions are summarized in Fig. B.2. The transition probabilities, α_{ij} (where i and j can be 1, 2, 3, or 4), from refinement of neutron powder diffraction data are included and are discussed in the next section.

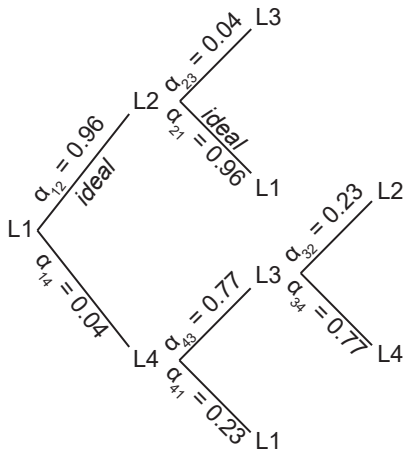

Figure B.2: Decision tree for layer-to-layer transitions with the probabilities, α_{ij}, from refined data.

Simulations of neutron powder diffraction data with varying percentages of fault defects are shown in Fig. B.3 (a). The 0% fault simulation represents alternating L1 to L2 transitions (pristine α-phase), and the 100% stacking faults simulation represents alternating L1 to L4 transitions (β-phase stacking). The percentage indicates the probability that if on an L1 or L2 layer, that the next layer will have a fault defect. Once

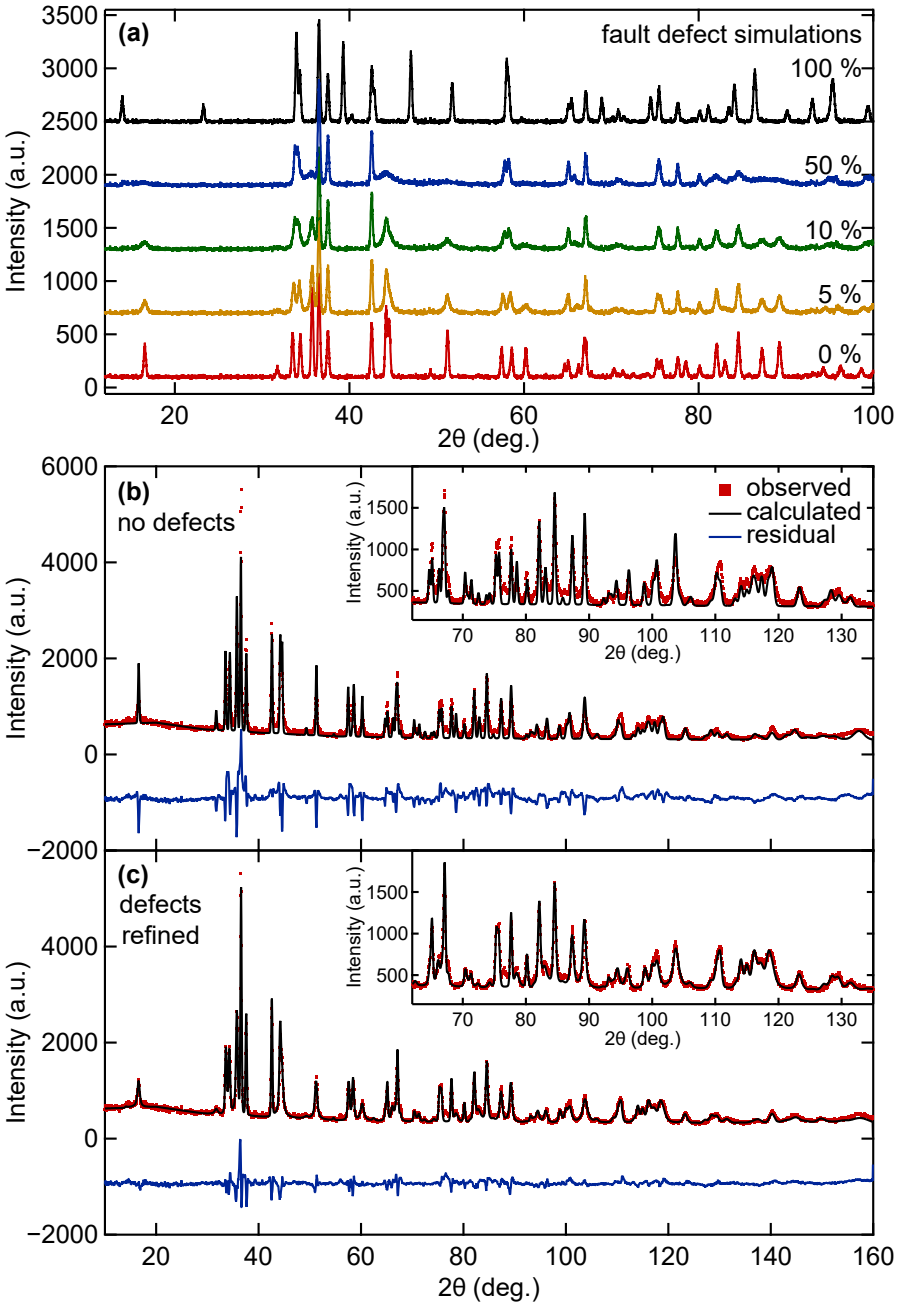

Figure B.3: Panel (a) shows a series of α-NaMnO$_2$ simulations with varying percentages of fault defects as described in the text. Refinement of the 0% defect model with data is shown in panel (b), and refinement which includes letting the probability of fault defects float is shown in panel (c).

faulted, the direction that the next layer translates will either define the defect to be a stacking fault or a twin boundary. It was found from refinement that after an initial layer-to-layer fault, the defect was more likely to become a twin boundary than a stacking fault (77% compared to 23%), and these values were used for the 5%, 10% and 50% fault defect simulations in Fig. B.3 (a). Fig. B.3 (b) shows room temperature neutron

powder diffraction data on a ground, 8 g, single-crystal of α-$NaMnO_2$, refined with the defect-free model. The line shape used was a pseudo-Voigt, where the parameters were fixed to be those of the instrument resolution (data taken on BT1 at NCNR). Only the scale factor, cell parameters, non high-symmetry atom positions, zero-shift, and layer-to-layer $|\Delta x|$ translation were allowed to refine. The refinement results are listed in Table B.1. The calculation fails to capture the correct intensities for the majority of the peaks, the line shape misses the Lorentzian-like broadening about the peaks, and some peak centers are not aligned perfectly with the peaks in the data. Something to note, is that the amount of broadening about a given peak is not the same for all peaks, and there is seemingly no *hkl* dependent pattern to the broadening. Thus, refining the line shape parameters does not capture the peak shapes throughout the pattern. Fig. B.3 (c) shows the same data, with the same parameters allowed to refine as Fig. B.3 (b), but additionally, the transition probabilities between layers were allowed to float. The code for a neutron powder diffraction simulation using the refined parameters can be found in Appendix B. The refinement represents the simplest model, where the translation between all layers has the same magnitude along x and z. In theory, $|\Delta x_F|$ and $|\Delta z_F|$ (defined in Fig. B.1) do not have to be equal to $|\Delta x_\alpha|$ and $|\Delta z_\alpha|$, respectively. The refinement indicates that during ideal stacking, on any given layer, there is a 4% chance of a defect upon transition to the next layer. Once on the faulted layer, there is a 77% chance of a twin boundary defect versus a 23% chance of a stacking fault defect. Without having to refine the line shape parameters, the fit to the data is profoundly improved and the residual between the data and calculated profile even out to high 2θ is small (see inset of Fig. B.3 (c) versus the inset of Fig. B.3 (b)).

B.1.1 Single crystal neutron diffraction

The FAULTS program can also simulate certain scattering planes for single crystal data. Fig. B.4 (a) shows a simulation of the $(H, 0, L)$ scattering plane using the values from the neutron powder diffraction refinement in Fig. B.3 (c). Diffuse rods can be seen along the $[\bar{1}, 0, 1]$ direction, which is the disordered direction due to faulting defects. Fig. B.4 (b) shows an equivalent plane of single-crystal, room temperature, neutron time-of-flight data taken on CORELLI at ORNL (the $K = 0$ plane was very limited in momentum

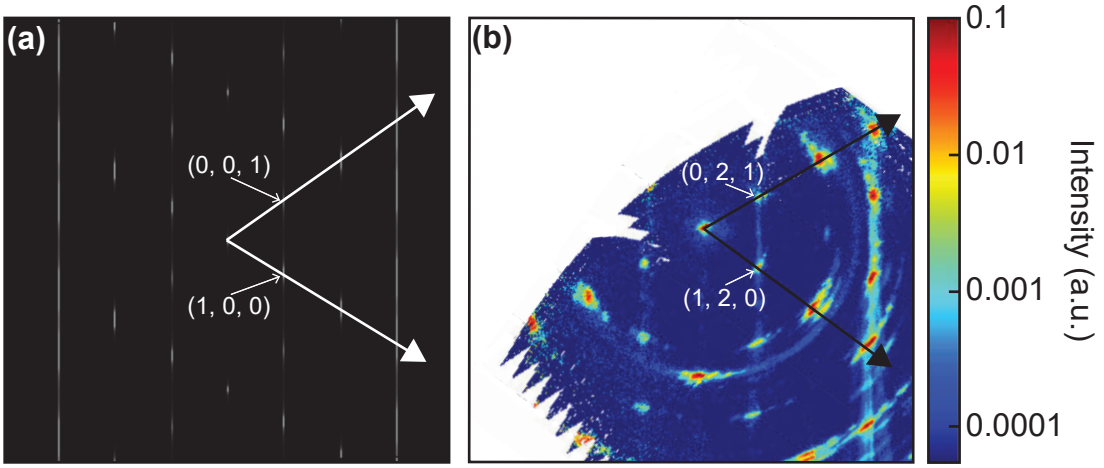

Figure B.4: Panel (a) shows a simulation of the $(H, 0, L)$ scattering plane for α-NaMnO$_2$ with fault defect percentages found from the refinement of neutron powder diffraction data. Panel (b) shows the $(H, 2, L)$ scattering plane of data taken on a single crystal in a neutron time-of-flight experiment.

space, so $K = 2$ was used). The simulation captures the relative intensities of the diffuse rods (i.e. some are more intense than others). It is also a helpful visualization for understanding how the diffuse rods can cut through other planes of scattering, which needs to be taken into account for triple-axis experiments.

B.2 FAULTS code

This section contains the FAULTS code used to simulate the neutron powder diffraction patterns in Fig. B.3 (a). The scale factor, non-high-symmetry atom positions, cell parameters, Δx translation, and transition probabilities are the refined values from Fig. B.3 (c). The relationship between the standard α-NaMnO$_2$ unit cell and that used in the FAULTS model is shown in Fig. B.5, and the refined values from Fig. B.3 (b) and (c) are listed in Table B.1.

FAULTS code begins below line.

```
TITLE
NMO_SF_simulation

INSTRUMENTAL AND SIZE BROADENING
!type of radiation
 Radiation        NEUTRON
!                 lambda1     lambda2     ratio
 Wavelength        1.5397      0.0000      0.0000
!instrumental aberrations        zero        sycos        sysin
```

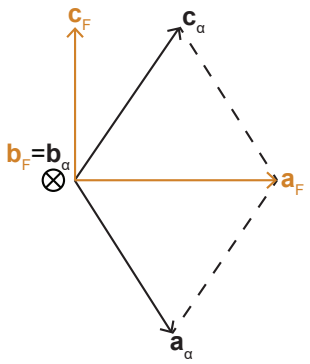

Figure B.5: The relationship between the α-NaMnO$_2$ (lattice vectors with α subscript) unit cell and FAULTS model (lattice vectors with F subscript).

Table B.1: caption

Parameter	defect free		refined defects	
	value	std. dev.	value	std. dev.
χ^2	17.3	n/a	4.4	n/a
R-Factor	13.6	n/a	6.7	n/a
scale factor	416.5	0.9	543	1
a (Å)	6.32115	0.00009	6.32081	0.00007
b (Å)	2.86221	0.00002	2.86224	0.00003
c (Å)	4.78417	0.00009	4.78424	0.00012
$\lvert\Delta x\rvert$ (layer-to-layer translation)	0.23968	0.00001	0.23964	0.00002
O1 x (same for all layers)	0.2012	0.0005	0.19424	0.0005
O1 z (same for all layers)	0.0276	0.0009	0.010	0.002
O2 x (same for all layers)	0.7782	0.0005	0.78277	0.0005
O2 z (same for all layers)	0.0227	0.0008	0.009	0.002
$\alpha_{12} = \alpha_{21}$	n/a	n/a	0.955	0.003
$\alpha_{14} = \alpha_{23} = 1 - \alpha_{12} = 1 - \alpha_{21}$	n/a	n/a	0.045	0.003
$\alpha_{41} = \alpha_{32}$	n/a	n/a	0.229	0.003
$\alpha_{43} = \alpha_{34} = 1 - \alpha_{41} = 1 - \alpha_{32}$	n/a	n/a	0.771	0.003

```
 Aberrations                              0.0000      0.0000      0.0000
                                          0.00        0.00        0.00
!instr.  broadening          u                v                w                x
Dg              Dl
 Pseudo-Voigt          0.200000      -0.150000       0.100000       0.010000
5000.00       5000.00 TRIM
                                0.00            0.00            0.00            0.00
0.00            0.00

 STRUCTURAL

!       FullProf Studio commands

FST_CMD  SEQ  10  1  2  1  2  3  4  3  4  1  2

!               a                  b                  c                gamma
```

```
 Cell        6.320812      2.862239      4.784235        90.00
                0.00          0.00          0.00          0.00
!Laue symmetry
 Symm  -1
!number of layer types
 NLAYERS    4
!layer width
 Lwidth   Infinite

 LAYER       1
!Layer symmetry
 LSYM     None

!Atom name     number     x           y           z           Biso        Occ
 Atom MN            1    0.00000     0.00000     0.00000     1.00000     1.00000
                            0.00        0.00        0.00        0.00
0.00
 Atom NA            1    0.50000     0.00000     0.00000     1.00000     1.00000
                            0.00        0.00        0.00        0.00
0.00
 Atom O             1    0.19424     0.50000     0.00985     1.00000     1.00000
                            0.00        0.00        0.00        0.00
0.00
 Atom O             2    0.78277     0.50000     0.00914     1.00000     1.00000
                            0.00        0.00        0.00        0.00
0.00

 LAYER       2
!Layer symmetry
 LSYM     None

!Atom name     number     x           y           z           Biso        Occ
 Atom MN            1    0.00000     0.50000     0.00000     1.00000     1.00000
                            0.00        0.00        0.00        0.00
0.00
 Atom NA            1    0.50000     0.50000     0.00000     1.00000     1.00000
                            0.00        0.00        0.00        0.00
0.00
 Atom O             1    0.19424     1.00000     0.00985     1.00000     1.00000
                            0.00        0.00        0.00        0.00
0.00
 Atom O             2    0.78277     1.00000     0.00914     1.00000     1.00000
                            0.00        0.00        0.00        0.00
0.00

 LAYER 3 = 1

 LAYER 4 = 2

 STACKING
```

```
!stacking type
 RECURSIVE
!number of layers
 INFINITE

 TRANSITIONS


!layer  1 to layer  1
LT      0.000000     0.000000     0.000000     0.000000
            0.00         0.00         0.00         0.00
FW      0.000000     0.000000     0.000000     0.000000     0.000000
0.000000
            0.00         0.00         0.00         0.00         0.00
0.00
!layer  1 to layer  2
LT      0.955408     0.239642     0.000000     0.500000
            0.00         0.00         0.00         0.00
FW      0.000000     0.000000     0.000000     0.000000     0.000000
0.000000
            0.00         0.00         0.00         0.00         0.00
0.00
!layer  1 to layer  3
LT      0.000000     0.000000     0.000000     0.000000
            0.00         0.00         0.00         0.00
FW      0.000000     0.000000     0.000000     0.000000     0.000000
0.000000
            0.00         0.00         0.00         0.00         0.00
0.00
!layer  1 to layer  4
LT      0.044592    -0.239642     0.000000     0.500000
            0.00         0.00         0.00         0.00
FW      0.000000     0.000000     0.000000     0.000000     0.000000
0.000000
            0.00         0.00         0.00         0.00         0.00
0.00


!layer  2 to layer  1
LT      0.955408     0.239642     0.000000     0.500000
            0.00         0.00         0.00         0.00
FW      0.000000     0.000000     0.000000     0.000000     0.000000
0.000000
            0.00         0.00         0.00         0.00         0.00
0.00
!layer  2 to layer  2
LT      0.000000     0.000000     0.000000     0.000000
            0.00         0.00         0.00         0.00
FW      0.000000     0.000000     0.000000     0.000000     0.000000
0.000000
```

```
            0.00          0.00          0.00          0.00          0.00
0.00
!layer  2 to layer  3
LT      0.044592     -0.239642     0.000000     0.500000
            0.00          0.00          0.00          0.00
FW      0.000000     0.000000     0.000000     0.000000     0.000000
0.000000
            0.00          0.00          0.00          0.00          0.00
0.00
!layer  2 to layer  4
LT      0.000000     0.000000     0.000000     0.000000
            0.00          0.00          0.00          0.00
FW      0.000000     0.000000     0.000000     0.000000     0.000000
0.000000
            0.00          0.00          0.00          0.00          0.00
0.00


!layer  3 to layer  1
LT      0.000000     0.000000     0.000000     0.000000
            0.00          0.00          0.00          0.00
FW      0.000000     0.000000     0.000000     0.000000     0.000000
0.000000
            0.00          0.00          0.00          0.00          0.00
0.00
!layer  3 to layer  2
LT      0.229286     0.239642     0.000000     0.500000
            0.00          0.00          0.00          0.00
FW      0.000000     0.000000     0.000000     0.000000     0.000000
0.000000
            0.00          0.00          0.00          0.00          0.00
0.00
!layer  3 to layer  3
LT      0.000000     0.000000     0.000000     0.000000
            0.00          0.00          0.00          0.00
FW      0.000000     0.000000     0.000000     0.000000     0.000000
0.000000
            0.00          0.00          0.00          0.00          0.00
0.00
!layer  3 to layer  4
LT      0.770714     -0.239642     0.000000     0.500000
            0.00          0.00          0.00          0.00
FW      0.000000     0.000000     0.000000     0.000000     0.000000
0.000000
            0.00          0.00          0.00          0.00          0.00
0.00


!layer  4 to layer  1
LT      0.229286     0.239642     0.000000     0.500000
```

```
                0.00          0.00          0.00          0.00
FW      0.000000      0.000000      0.000000      0.000000      0.000000
0.000000
                0.00          0.00          0.00          0.00          0.00
0.00
!layer  4 to layer  2
LT      0.000000      0.000000      0.000000      0.000000
                0.00          0.00          0.00          0.00
FW      0.000000      0.000000      0.000000      0.000000      0.000000
0.000000
                0.00          0.00          0.00          0.00          0.00
0.00
!layer  4 to layer  3
LT      0.770714     -0.239642      0.000000      0.500000
                0.00          0.00          0.00          0.00
FW      0.000000      0.000000      0.000000      0.000000      0.000000
0.000000
                0.00          0.00          0.00          0.00          0.00
0.00
!layer  4 to layer  4
LT      0.000000      0.000000      0.000000      0.000000
                0.00          0.00          0.00          0.00
FW      0.000000      0.000000      0.000000      0.000000      0.000000
0.000000
                0.00          0.00          0.00          0.00          0.00
0.00

 Calculation
 Simulation
 Powder 10.0 160.0 0.01   Scalef 543.326

 Replace_Files

!number of pattern backgrounds
 Bgrnum  0
```

References

[1] Treacy, M. M. J., Newsam, J. M. & Deem, M. W. A general recursion method for calculating diffracted intensities from crystals containing planar faults. *Proceedings of the Royal Society of London A: Mathematical, Physical and Engineering Sciences* **433**, 499–520 (1991).

[2] Berliner, R. & Werner, S. A. Effect of stacking faults on diffraction: The structure of lithium metal. *Phys. Rev. B* **34**, 3586–3603 (1986).

[3] Casas-Cabanas, M., Reynaud, M., Rikarte, J., Horbach, P. & Rodríguez-Carvajal, J. *FAULTS*: a program for refinement of structures with extended defects. *Journal of Applied Crystallography* **49**, 2259–2269 (2016).

Appendix C

Two-magnon continuum of a 1D antiferromagnet with single-ion anisotropy

This appendix derives the two-magnon excitation at the zone center for a 1D antiferromagnet with isotropic Heisenberg spins and easy-axis single-ion anisotropy. This calculation was done to show that the longitudinal mode observed in α-$NaMnO_2$ does not originate from a two-magnon excitation due to the discrepancies in energy (mainly, the peak excitation energy) and shape (there exists a continuum in the two-magnon excitation). This derivation closely follows the detailed method in Ref. [1] for the two-magnon excitation of a 1D anisotropic Heisenberg antiferromagnet in a magnetic field, and Ref. [2] for guidance on the linear spin-wave theory section.

The two-magnon excitation is longitudinally polarized, so our goal is to solve for the $T = 0$ longitudinal response function, $G_q^{xx}(\omega)$, at the zone-center, which is what inelastic neutron scattering can probe in an energy scan at $\mathbf{Q} = \left(\frac{1}{2}, \frac{1}{2}, 0\right)$ in α-$NaMnO_2$. In order to solve for the longitudinal response function, one first needs to solve for the correlation function, $\left\langle S_q^x(t) S_{-q}^x \right\rangle$, where x is the spin axis. This function contains the Bragg scattering, and only that, if higher order terms in linear spin-wave theory are tossed. By keeping the fourth order terms, you will get a term describing the correlation in the length fluctuations of spins, which is needed for $G_q^{xx}(\omega)$. Luckily, Ref. [1] has solved for $\left\langle S_q^x(t) S_{-q}^x \right\rangle$ to the fourth order already, and the longitudinal response function is (Eqn. 2.22 in Ref. [1]),

$$\begin{aligned} G_q^{xx}(\omega) &= \frac{1}{2\pi\hbar} \int_{-\infty}^{\infty} e^{i\omega t} \left\langle S_q^x(t) S_{-q}^x \right\rangle dt \\ &= \frac{1}{4\pi} \sum_i (\eta_{q\pm k_0+q_i} \rho_{q_i} + \rho_{q\pm k_0+q_i} \eta_{q_i})^2 \times \left| \frac{\partial}{\partial q'} (\omega_{q\pm k_0+q'} + \omega_{q'}) \right|^{-1} \end{aligned} \tag{C.1}$$

We need only find the term, $\frac{2\rho_q \eta_q}{\rho_q^2 + \eta_q^2}$, tailored to our Hamiltonian (the relation for the Hamiltonian in Ref. [1] is Eqn. 2.9), and can do so without the higher order terms in linear spin-wave theory.

We start with our Hamiltonian,

$$\begin{aligned} H &= J\sum_{\langle \mathrm{i\,j}\rangle} \mathbf{S}_\mathrm{i}\cdot\mathbf{S}_\mathrm{j} - D\sum_\mathrm{i}(S_\mathrm{i}^z)^2 - D\sum_\mathrm{j}(S_\mathrm{j}^z)^2 \\ &= J\sum_{\langle \mathrm{i\,j}\rangle}\left[S_\mathrm{i}^x S_\mathrm{j}^x + S_\mathrm{i}^y S_\mathrm{j}^y + S_\mathrm{i}^z S_\mathrm{j}^z\right] - D\sum_\mathrm{i}(S_\mathrm{i}^z)^2 - D\sum_\mathrm{j}(S_\mathrm{j}^z)^2 \end{aligned} \tag{C.2}$$

where $J>0$ is the isotropic exchange interaction, $D>0$ is the easy-axis single-ion anisotropy, the summation is over nearest neighbor pairs (of which there are two per atom), $\langle \mathrm{i\,j}\rangle$, and $S_\mathrm{i}^x = \frac{1}{2}\left(\hat{S}_\mathrm{i}^+ + \hat{S}_\mathrm{i}^-\right)$ and $S_\mathrm{i}^x = \frac{1}{2i}\left(\hat{S}_\mathrm{i}^+ - \hat{S}_\mathrm{i}^-\right)$. There are N atoms on each the A and B sublattices, corresponding to i and j sites, respectively. Atoms on the A sublattice have opposite spin as those on the B sublattice. Eqn. C.2 can now be rewritten using the following relations:

$$S_\mathrm{i}^x S_\mathrm{j}^x = \frac{1}{4}\left(\hat{S}_\mathrm{i}^+\hat{S}_\mathrm{j}^+ + \hat{S}_\mathrm{i}^-\hat{S}_\mathrm{j}^- + \hat{S}_\mathrm{i}^+\hat{S}_\mathrm{j}^- + \hat{S}_\mathrm{i}^-\hat{S}_\mathrm{j}^+\right) \tag{C.3}$$

$$S_\mathrm{i}^y S_\mathrm{j}^y = -\frac{1}{4}\left(\hat{S}_\mathrm{i}^+\hat{S}_\mathrm{j}^+ + \hat{S}_\mathrm{i}^-\hat{S}_\mathrm{j}^- - \hat{S}_\mathrm{i}^+\hat{S}_\mathrm{j}^- - \hat{S}_\mathrm{i}^-\hat{S}_\mathrm{j}^+\right) \tag{C.4}$$

$$S_\mathrm{i}^x S_\mathrm{j}^x + S_\mathrm{i}^y S_\mathrm{j}^y = \frac{1}{2}\left(\hat{S}_\mathrm{i}^+\hat{S}_\mathrm{j}^- + \hat{S}_\mathrm{i}^-\hat{S}_\mathrm{j}^+\right) \tag{C.5}$$

Such that,

$$H = J\sum_{\langle \mathrm{i\,j}\rangle}\left[\frac{1}{2}\left(\hat{S}_\mathrm{i}^+\hat{S}_\mathrm{j}^- + \hat{S}_\mathrm{i}^-\hat{S}_\mathrm{j}^+\right) + S_\mathrm{i}^z S_\mathrm{j}^z\right] - D\sum_\mathrm{i}(S_\mathrm{i}^z)^2 - D\sum_\mathrm{j}(S_\mathrm{j}^z)^2 \tag{C.6}$$

Next, we will use the Holstein–Primakoff transformation [3], which replaces the spin operators with boson creation and annihilation operators, and is also the "linear" part of linear spin wave theory. The spin operators have been expanded to order $1/\sqrt{S}$, which is a valid approximation at low temperature, where the fluctuations of the ordered moments are expected to be small. The relations are,

$$\begin{aligned} \hat{S}_\mathrm{i}^+ &= \sqrt{2S}\sqrt{1-\frac{a_\mathrm{i}^\dagger a_\mathrm{i}}{2S}}\,a_\mathrm{i}, \quad \hat{S}_\mathrm{j}^+ = \sqrt{2S}\,b_\mathrm{j}^\dagger\sqrt{1-\frac{b_\mathrm{j}^\dagger b_\mathrm{j}}{2S}}, \quad S_\mathrm{i}^z = S - a_\mathrm{i}^\dagger a_\mathrm{i} \\ \hat{S}_\mathrm{i}^- &= \sqrt{2S}\,a_\mathrm{i}^\dagger\sqrt{1-\frac{a_\mathrm{i}^\dagger a_\mathrm{i}}{2S}}, \quad \hat{S}_\mathrm{j}^- = \sqrt{2S}\sqrt{1-\frac{b_\mathrm{j}^\dagger b_\mathrm{j}}{2S}}\,b_\mathrm{j}, \quad S_\mathrm{j}^z = -S + b_\mathrm{j}^\dagger b_\mathrm{j}, \end{aligned} \tag{C.7}$$

and the operators a_{i} and b_{j} refer to operators for the the ith atom of sublattice a and the jth atom of sublattice b, respectively. By tossing higher order terms, the following products become,

$$\begin{aligned}
\hat{S}_{\mathrm{i}}^{+}\hat{S}_{\mathrm{j}}^{-} &= 2Sa_{\mathrm{i}}b_{\mathrm{j}} \\
\hat{S}_{\mathrm{i}}^{-}\hat{S}_{\mathrm{j}}^{+} &= 2Sa_{\mathrm{i}}^{\dagger}b_{\mathrm{j}}^{\dagger} \\
(S_{\mathrm{i}}^{z})^{2} &= S^{2} - 2Sa_{\mathrm{i}}^{\dagger}a_{\mathrm{i}} \\
(S_{\mathrm{j}}^{z})^{2} &= S^{2} - 2Sb_{\mathrm{j}}^{\dagger}b_{\mathrm{j}}
\end{aligned} \tag{C.8}$$

and we can once again rewrite the Hamiltonian,

$$\begin{aligned}
H &= JS\sum_{\langle \mathrm{i}\,\mathrm{j}\rangle}\left[a_{\mathrm{i}}b_{\mathrm{j}} + a_{\mathrm{i}}^{\dagger}b_{\mathrm{j}}^{\dagger} - S + b_{\mathrm{j}}^{\dagger}b_{\mathrm{j}} + a_{\mathrm{i}}^{\dagger}a_{\mathrm{i}}\right] \\
&\quad - DS\sum_{\mathrm{i}}\left(S - 2a_{\mathrm{i}}^{\dagger}a_{\mathrm{i}}\right) - DS\sum_{\mathrm{j}}\left(S - 2b_{\mathrm{j}}^{\dagger}b_{\mathrm{j}}\right) \\
&= -2JS^{2}N + JS\sum_{\langle \mathrm{i}\,\mathrm{j}\rangle}\left[a_{\mathrm{i}}b_{\mathrm{j}} + a_{\mathrm{i}}^{\dagger}b_{\mathrm{j}}^{\dagger} + b_{\mathrm{j}}^{\dagger}b_{\mathrm{j}} + a_{\mathrm{i}}^{\dagger}a_{\mathrm{i}}\right] \\
&\quad - 2DS^{2}N + 2DS\left(\sum_{\mathrm{i}}a_{\mathrm{i}}^{\dagger}a_{\mathrm{i}} + \sum_{\mathrm{j}}b_{\mathrm{j}}^{\dagger}b_{\mathrm{j}}\right)
\end{aligned} \tag{C.9}$$

The creation and annihilation operators written in terms of momentum space are:

$$\begin{aligned}
a_{\mathrm{i}}^{\dagger} &= \frac{1}{\sqrt{N}}\sum_{\mathbf{q}} e^{-i\mathbf{q}\cdot\mathbf{R}_{\mathrm{i}}}a_{\mathbf{q}}^{\dagger}, \quad b_{\mathrm{j}}^{\dagger} = \frac{1}{\sqrt{N}}\sum_{\mathbf{q}} e^{i\mathbf{q}\cdot\mathbf{R}_{\mathrm{j}}}b_{\mathbf{q}}^{\dagger} \\
a_{\mathrm{i}} &= \frac{1}{\sqrt{N}}\sum_{\mathbf{q}} e^{i\mathbf{q}\cdot\mathbf{R}_{\mathrm{i}}}a_{\mathbf{q}}, \qquad b_{\mathrm{j}} = \frac{1}{\sqrt{N}}\sum_{\mathbf{q}} e^{-i\mathbf{q}\cdot\mathbf{R}_{\mathrm{j}}}b_{\mathbf{q}}
\end{aligned} \tag{C.10}$$

Physically, these momentum space operators represent a magnon at momentum $\mathbf{q}$ being created ($a_{\mathbf{q}}^{\dagger}$ or $b_{\mathbf{q}}^{\dagger}$) and a magnon at at momentum $\mathbf{q}$ being destroyed ($a_{\mathbf{q}}$ or $b_{\mathbf{q}}$). Now, replace the direct-space operators in Eqn. C.9 with the relations in Eqn. C.10 to put the Hamiltonian in momentum space. Useful product relations are,

$$
\begin{aligned}
a_{\mathrm{i}}^{\dagger}a_{\mathrm{i}} &= \frac{1}{N}\sum_{\mathbf{q},\mathbf{q}'}\left[e^{-i(\mathbf{q}-\mathbf{q}')\cdot\mathbf{R}_{\mathrm{i}}}a_{\mathbf{q}}^{\dagger}a_{\mathbf{q}'}\right] \\
a_{\mathrm{i}}b_{\mathrm{j}} &= \frac{1}{N}\sum_{\mathbf{q},\mathbf{q}'}\left[e^{i(\mathbf{q}-\mathbf{q}')\cdot\mathbf{R}_{\mathrm{i}}}e^{-i\mathbf{q}'\cdot\Delta\mathbf{R}}a_{\mathbf{q}}b_{\mathbf{q}'}\right],
\end{aligned}
\tag{C.11}
$$

along with $a_{\mathrm{i}}^{\dagger}b_{\mathrm{j}}^{\dagger}$ and $b_{\mathrm{j}}^{\dagger}b_{\mathrm{j}}$. To minimize the number of variables, the relation between nearest neighbors $\Delta\mathbf{R} = \mathbf{R}_{\mathrm{j}} - \mathbf{R}_{\mathrm{i}}$ has been used. $\Delta\mathbf{R}$ is just the lattice spacing along the chain, which will be set to a magnitude of unity, such that $\mathbf{q}\cdot\Delta\mathbf{R} = q$. The Hamiltonian is now,

$$
\begin{aligned}
H = &-2JS^2N + \frac{2JS}{N}\sum_{\mathbf{q},\mathbf{q}'}\sum_{\mathrm{i}\in\mathrm{A}}\Big[e^{i(\mathbf{q}-\mathbf{q}')\cdot\mathbf{R}_{\mathrm{i}}}e^{-iq'}a_{\mathbf{q}}b_{\mathbf{q}'} + e^{-i(\mathbf{q}-\mathbf{q}')\cdot\mathbf{R}_{\mathrm{i}}}e^{iq'}a_{\mathbf{q}}^{\dagger}b_{\mathbf{q}'}^{\dagger} \\
&+ e^{i(\mathbf{q}-\mathbf{q}')\cdot\mathbf{R}_{\mathrm{i}}}e^{i(q-q')}b_{\mathbf{q}}^{\dagger}b_{\mathbf{q}'} + e^{-i(\mathbf{q}-\mathbf{q}')\cdot\mathbf{R}_{\mathrm{i}}}a_{\mathbf{q}}^{\dagger}a_{\mathbf{q}'}\Big] \\
&- 2DS^2N + \frac{2DS}{N}\sum_{\mathbf{q},\mathbf{q}'}\sum_{\mathrm{i}\in\mathrm{A}}\left[e^{-i(\mathbf{q}-\mathbf{q}')\cdot\mathbf{R}_{\mathrm{i}}}a_{\mathbf{q}}^{\dagger}a_{\mathbf{q}'} + e^{i(\mathbf{q}-\mathbf{q}')\cdot\mathbf{R}_{\mathrm{i}}}e^{i(q-q')}b_{\mathbf{q}}^{\dagger}b_{\mathbf{q}'}\right]
\end{aligned}
\tag{C.12}
$$

When summing over $\sum_{\mathbf{q},\mathbf{q}'}$, all terms with exponents having $\mathbf{q}-\mathbf{q}'$ will cancel out except for when $\mathbf{q} = \mathbf{q}'$, because for every $|\mathbf{q}| - |\mathbf{q}'|$ term, there is a $-|\mathbf{q}| - (-|\mathbf{q}'|)$ term. When $\mathbf{q} = \mathbf{q}'$, $\sum_{\mathbf{q},\mathbf{q}'}\sum_{\mathrm{i}\in\mathrm{A}} e^{i(\mathbf{q}-\mathbf{q}')\cdot\mathbf{R}_{\mathrm{i}}} = N$, because there are N i-sites in the A sublattice. The Hamiltonian is now,

$$
\begin{aligned}
H = &-2(J+D)S^2N + 2JS\sum_{\mathbf{q}}\left[e^{-iq}a_{\mathbf{q}}b_{\mathbf{q}} + e^{iq}a_{\mathbf{q}}^{\dagger}b_{\mathbf{q}}^{\dagger} + a_{\mathbf{q}}^{\dagger}a_{\mathbf{q}} + b_{\mathbf{q}}^{\dagger}b_{\mathbf{q}}\right] \\
&+ 2DS\sum_{\mathbf{q}}\left(a_{\mathbf{q}}^{\dagger}a_{\mathbf{q}} + b_{\mathbf{q}}^{\dagger}b_{\mathbf{q}}\right)
\end{aligned}
\tag{C.13}
$$

When summing over all $\mathbf{q}$, e^{-iq} terms will become just $\cos q$, as sin is an odd function and the total sum will be zero and,

$$
H = -2(J+D)S^2N + 2JS\sum_{\mathbf{q}}\left[\left(1+\frac{D}{J}\right)\left(a_{\mathbf{q}}^{\dagger}a_{\mathbf{q}} + b_{\mathbf{q}}^{\dagger}b_{\mathbf{q}}\right) + \gamma_q\left(a_{\mathbf{q}}b_{\mathbf{q}} + a_{\mathbf{q}}^{\dagger}b_{\mathbf{q}}^{\dagger}\right)\right] \tag{C.14}
$$

where $\gamma_q = \cos q$. In order to solve for the magnon eigenfrequencies, the Hamilto-

nian needs to be diagonalized. A new set of creation and annihilation operators that maintain the boson commutation relations can be found by referring to the Bogoliubov transformation, where:

$$\begin{aligned} a_{\mathbf{q}} &= \cosh\theta_{\mathbf{q}}\alpha_{\mathbf{q}} - \sinh\theta_{\mathbf{q}}\beta^{\dagger}_{\mathbf{q}} \\ a^{\dagger}_{\mathbf{q}} &= \cosh\theta_{\mathbf{q}}\alpha^{\dagger}_{\mathbf{q}} - \sinh\theta_{\mathbf{q}}\beta_{\mathbf{q}} \\ b_{\mathbf{q}} &= -\sinh\theta_{\mathbf{q}}\alpha^{\dagger}_{\mathbf{q}} + \cosh\theta_{\mathbf{q}}\beta_{\mathbf{q}} \\ b^{\dagger}_{\mathbf{q}} &= -\sinh\theta_{\mathbf{q}}\alpha_{\mathbf{q}} + \cosh\theta_{\mathbf{q}}\beta^{\dagger}_{\mathbf{q}} \end{aligned} \tag{C.15}$$

Defining $\cosh\theta_{\mathbf{q}} = \rho_q$ and $\sinh\theta_{\mathbf{q}} = \eta_q$ and using the commutation relations $\left[\alpha_{\mathbf{q}}, \alpha^{\dagger}_{\mathbf{q}}\right] = 1$, $\left[\beta_{\mathbf{q}}, \beta^{\dagger}_{\mathbf{q}}\right] = 1$, $[\alpha_{\mathbf{q}}, \beta_{\mathbf{q}}] = 0$ and $\left[\alpha^{\dagger}_{\mathbf{q}}, \beta^{\dagger}_{\mathbf{q}}\right] = 0$, the Hamiltonian becomes,

$$\begin{aligned} H = &-2(J+D)S^2N \\ &+ 2JS\sum_{\mathbf{q}}\Big[\left(\alpha^{\dagger}_{\mathbf{q}}\alpha_{\mathbf{q}} + \beta^{\dagger}_{\mathbf{q}}\beta_{\mathbf{q}}\right)\left[\left(1+\frac{D}{J}\right)\left(\rho_q^2+\eta_q^2\right) - 2\gamma_q\rho_q\eta_q\right] \\ &+ \left(\alpha_{\mathbf{q}}\beta_{\mathbf{q}} + \alpha^{\dagger}_{\mathbf{q}}\beta^{\dagger}_{\mathbf{q}}\right)\left[-2\rho_q\eta_q\left(1+\frac{D}{J}\right) + \gamma_q\left(\rho_q^2+\eta_q^2\right)\right] \\ &+ 2\eta_q^2\left(1+\frac{D}{J}\right) - 2\gamma\rho_q\eta_q\Big] \end{aligned} \tag{C.16}$$

Now, in order to diagonalize the Hamiltonian, we must get rid of the off-diagonal terms. To do this, we want coefficients such that all $\alpha_{\mathbf{q}}\beta_{\mathbf{q}}$ and $\alpha^{\dagger}_{\mathbf{q}}\beta^{\dagger}_{\mathbf{q}}$ terms sum to zero. Gather those terms and set them equal to zero, and one can solve for $\frac{2\rho_q\eta_q}{\rho_q^2+\eta_q^2}$, finding that,

$$\begin{aligned} \frac{2\rho_q\eta_q}{\rho_q^2+\eta_q^2} &= \frac{\cos q}{1+\frac{D}{J}} \\ &= \tanh 2\theta_{\mathbf{q}} \end{aligned} \tag{C.17}$$

We are now ready to use this solution in conjunction with the longitudinal response function to solve for the two-magnon excitation spectra at the zone-center. Before going back to Eqn. C.1, and for completion's sake, we can solve for the single-magnon dispersion. The diagonalized Hamiltonian is,

$$
\begin{aligned}
H &= -2(J+D)S^2N \\
&+ 2JS\sum_{\mathbf{q}}\Big[\left(\alpha^\dagger_{\mathbf{q}}\alpha_{\mathbf{q}}+\beta^\dagger_{\mathbf{q}}\beta_{\mathbf{q}}\right)\left[\left(1+\frac{D}{J}\right)\left(\rho_q^2+\eta_q^2\right)-2\gamma_q\rho_q\eta_q\right] \\
&+ 2\eta_q^2\left(1+\frac{D}{J}\right)-2\gamma\rho_q\eta_q\Big]
\end{aligned}
\tag{C.18}
$$

The zero-point energy is going to be in the form, $E_0 = \text{constant} + \sum_{\mathbf{q}}\omega_{\mathbf{q}}$. When Eqn. C.18 acts on the $T=0$ ground state of the system, we are left with,

$$
E_0 = -2(J+D)S^2N + 2JS\sum_{\mathbf{q}}\left[2\eta_q^2\left(1+\frac{D}{J}\right)-2\gamma\rho_q\eta_q\right] \tag{C.19}
$$

Using the result from Eqn. C.17, the hyperbolic function relations,

$$
\cosh 2\theta_{\mathbf{q}} = \left[1-\tanh^2 2\theta_{\mathbf{q}}\right]^{-1/2} = \left[1-\left(\frac{\cos q}{1+\frac{D}{J}}\right)^2\right]^{-1/2} \tag{C.20}
$$

$$
\rho_q\eta_q = \cosh\theta_{\mathbf{q}}\sinh\theta_{\mathbf{q}} = \frac{1}{2}\sinh 2\theta_{\mathbf{q}} = \frac{1}{2}\cosh 2\theta_{\mathbf{q}}\tanh 2\theta_{\mathbf{q}} \tag{C.21}
$$

$$
= \frac{1}{2}\left[1-\left(\frac{\cos q}{1+\frac{D}{J}}\right)^2\right]^{-1/2}\tanh 2\theta_{\mathbf{q}} \tag{C.22}
$$

$$
\eta_q^2 = \sinh^2\theta_{\mathbf{q}} = \frac{1}{2}\left(\cosh 2\theta_{\mathbf{q}}-1\right) \tag{C.23}
$$

$$
\frac{1}{2}\left(\left[1-\left(\frac{\cos q}{1+\frac{D}{J}}\right)^2\right]^{-1/2}-1\right) \tag{C.24}
$$

and some algebra, we end up with,

$$
\begin{aligned}
E_0 &= -2N(J+D)S(S+1) + 2S\sum_{\mathbf{q}}\sqrt{D^2+2DJ+J^2\sin^2 q} \\
&= -2N(J+D)S(S+1) + \sum_{\mathbf{q}}\omega_{\mathbf{q}}
\end{aligned}
\tag{C.25}
$$

We can see that the dispersion relation is $\omega_{\mathbf{q}} = 2S\sqrt{D^2+2DJ+J^2\sin^2 q}$. In fact, we can rewrite the Hamiltonian, Eqn. C.18, to be,

$$H = -2N(J+D)S(S+1) + \sum_{\mathbf{q}} \omega_{\mathbf{q}} \left(\alpha^{\dagger}_{\mathbf{q}} \alpha_{\mathbf{q}} + \beta^{\dagger}_{\mathbf{q}} \beta_{\mathbf{q}} + 1 \right) \tag{C.26}$$

The modes associated with $\alpha^{\dagger}_{\mathbf{q}}\alpha_{\mathbf{q}}$ and $\beta^{\dagger}_{\mathbf{q}}\beta_{\mathbf{q}}$ are degenerate, and there is only one dispersion curve, $\omega_{\mathbf{q}}$. Now, we can move on to finding the longitudinal response function, starting with Eqn. C.1.

$$G^{xx}_{q}(\omega) = \frac{1}{4\pi} \sum_{i} (\eta_{q \pm k_0 + q_i} \rho_{q_i} + \rho_{q \pm k_0 + q_i} \eta_{q_i})^2 \times \left| \frac{\partial}{\partial q'} (\omega_{q \pm k_0 + q'} + \omega_{q'}) \right|^{-1}$$

and at the zone center, $q = \pi = k_0$, $q_1 = -q_2$, and $\omega = 2\omega_{q_1}$

$$G^{xx}_{q=k_0}(\omega) = \frac{1}{4\pi} \sum_{i} (\eta_{q_i} \rho_{q_i} + \rho_{q_i} \eta_{q_i})^2 \times \left| \frac{\partial}{\partial q'} (2\omega_{q'}) \right|^{-1} \tag{C.27}$$

where $\eta_{q_i}\rho_{q_i} = \rho_{q_i}\eta_{q_i}$

$$\begin{aligned} G^{xx}_{q=k_0}(\omega) &= \frac{1}{4\pi} \sum_{i} (2\eta_{q_i} \rho_{q_i})^2 \times \left| \frac{\partial}{\partial q'} (2\omega_{q'}) \right|^{-1} \\ &= \frac{1}{4\pi} \left[(2\eta_{q_1} \rho_{q_1})^2 + (2\eta_{q_2} \rho_{q_2})^2 \right] \times \left| \frac{\partial}{\partial q'} (2\omega_{q'}) \right|^{-1} \\ &= \frac{1}{4\pi} (2\eta_{q_1} \rho_{q_1})^2 \times \left| \frac{\partial}{\partial q'} (\omega_{q'}) \right|^{-1} \end{aligned} \tag{C.28}$$

Using the dispersion relation we found in Eqn. C.25, we can solve the partial derivative,

$$\frac{\partial}{\partial q} \omega_q = \frac{(2JS)^2}{\omega_q} \cos q \sin q \tag{C.29}$$

$$\left| \frac{\partial}{\partial q} \omega_q \right|^{-1} = \left| \frac{\omega_q}{(2JS)^2 \cos q \sin q} \right| \tag{C.30}$$

Plugging the result of Eqn. C.30 into Eqn. C.28, we arrive at,

$$G^{xx}_{q=k_0}(\omega) = \frac{1}{4\pi}(2\eta_{q_1}\rho_{q_1})^2 \times \left| \frac{\omega_{q'}}{(2JS)^2 \cos q' \sin q'} \right| \tag{C.31}$$

Using the result obtained from Eqn. C.17,

$$2\rho_{q_1}\eta_{q_1} = \frac{\cos q}{1+\frac{D}{J}} \left(\rho_q^2 + \eta_q^2\right) \tag{C.32}$$

Some more relationships we will need are,

$$\sin^2 q = \frac{1}{(2JS)^2}\left[\omega_q^2 - (2DS)^2 - 8DJS^2\right] \tag{C.33}$$

$$\cos^2 q = 1 - \frac{1}{(2JS)^2}\left[\omega_q^2 - (2DS)^2 - 8DJS^2\right] \tag{C.34}$$

$$|\cos q \sin q| = \left[\frac{1}{(2JS)^2}\left[\omega_q^2 - (2DS)^2 - 8DJS^2\right]\right]^{1/2} \tag{C.35}$$

$$\times \left[1 - \frac{1}{(2JS)^2}\left[\omega_q^2 - (2DS)^2 - 8DJS^2\right]\right]^{1/2} \tag{C.36}$$

$$\begin{aligned}
\rho_q^2 + \eta_q^2 &= \cosh 2\theta_q \\
&= \frac{1}{\sqrt{\operatorname{sech}^2 2\theta_q}} \\
&= \frac{1}{\sqrt{1 - \tanh^2 2\theta_q}} \\
&= \frac{1}{\sqrt{1 - \frac{\cos^2 q}{\left(1+\frac{D}{J}\right)^2}}} \\
&= \frac{J\left(1+\frac{D}{J}\right)}{\sqrt{D^2 + 2DJ + J^2\sin^2 q}} \\
&= \frac{2JS\left(1+\frac{D}{J}\right)}{\omega_q}
\end{aligned} \tag{C.37}$$

$$\begin{aligned} 2\rho_q\eta_q &= \left[\frac{\cos q}{1+\frac{D}{J}}\right]\left[\frac{2JS\left(1+\frac{D}{J}\right)}{\omega_q}\right] \\ &= \frac{2JS\cos q}{\omega_q} \end{aligned} \tag{C.38}$$

$$\begin{aligned} G^{xx}_{q=k_0}(\omega) &= \frac{1}{4\pi}\frac{(2JS)^2\cos^2 q_1}{\omega_{q_1}^2}\times\left|\frac{\omega_{q'}}{(2JS)^2\cos q'\sin q'}\right| \\ &= \frac{1}{4\pi}\frac{1-\frac{1}{(2JS)^2}\left[\omega_{q_1}^2-(2DS)^2-8DJS^2\right]}{\omega_{q_1}^2}\times\left|\frac{\omega_{q'}}{\cos q'\sin q'}\right| \end{aligned} \tag{C.39}$$

Now, replace ω_{q_1} using the relation $\omega = 2\omega_{q_1}$

$$G^{xx}_{q=k_0}(\omega) = \frac{1}{\pi}\frac{1-\frac{1}{(2JS)^2}\left[\frac{\omega^2}{4}-(2DS)^2-8DJS^2\right]}{\omega^2}\times\left|\frac{\omega_{q'}}{\cos q'\sin q'}\right| \tag{C.40}$$

Also, $\omega = 2\omega_{q'}$

$$G^{xx}_{q=k_0}(\omega) = \frac{1}{2\pi\omega}\left[\frac{(2JS)^2-\left(\frac{\omega^2}{4}-(2DS)^2-8DJS^2\right)}{\frac{\omega^2}{4}-(2DS)^2-8DJS^2}\right]^{1/2} \tag{C.41}$$

Rearranging terms some more:

$$G^{xx}_{q=k_0}(\omega) = \frac{1}{2\pi\omega}\left[\frac{-\omega^2+16S^2\left(J^2+D^2+2DJ\right)}{\omega^2-16DS^2\left(D+2J\right)}\right]^{1/2} \tag{C.42}$$

There exists a singularity when $\omega^2 = 16DS^2\left(D+2J\right)$. Written another way, this is when $\omega = 4S\sqrt{D^2+2DJ}$, which is precisely twice the single-magnon gap energy at the zone center, which is where we are solving for $G^{xx}_{q=k_0}(\omega)$. Both the real and imaginary components of $G^{xx}_{q=k_0}(\omega)$ are plotted in Fig. C.1 (a). Also plotted is the real part of $G^{xx}_{q=k_0}(\omega)$, convolved with the energy resolution function of the triple-axis spectrometer, BT7, at $\mathbf{Q} = (0.5, 0.5, 0)$ and $T = 5$ K. The convolution does not take into account the momentum resolution (i.e. not a proper convolution), but for comparison, a typical

energy cut at $\mathbf{Q} = (0.5, 0.5, 0)$ on BT7 is shown in Fig. C.1 (b) with the convolved function.

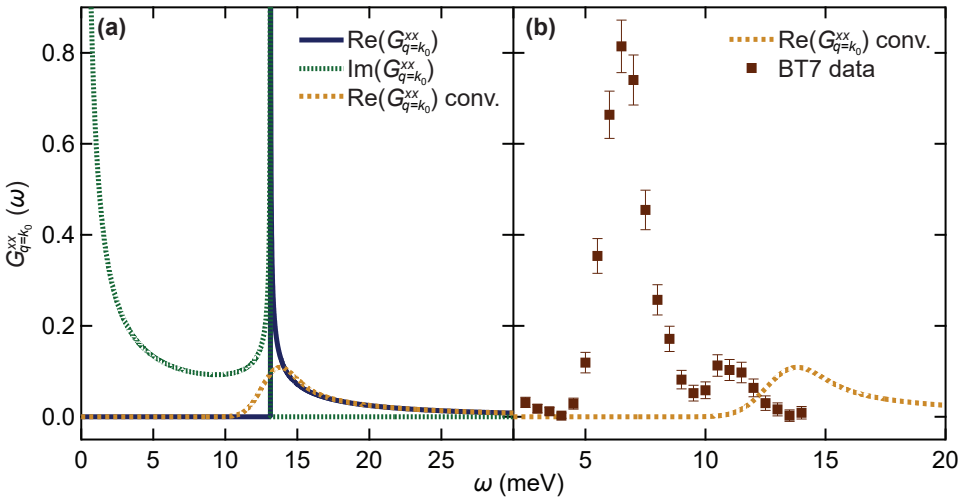

Figure C.1: The longitudinal response function for a 1D antiferromagnet with single-ion anisotropy. (a) Both the real and imaginary parts of the function are plotted. Additionally, the real part of the function convolved with the instrumental energy resolution is overlayed. (b) The energy convolved real part of the longitudinal response function with $T = 5$ K data taken from BT7 at $\mathbf{Q} = (0.5, 0.5, 0)$.

References

[1] Heilmann, I. U. *et al.* One- and two-magnon excitations in a one-dimensional antiferromagnet in a magnetic field. *Phys. Rev. B* **24**, 3939–3953 (1981).

[2] Kittel, C. *Quantum theory of solids.* (Wiley, New York, 1963).

[3] Holstein, T. & Primakoff, H. Field Dependence of the Intrinsic Domain Magnetization of a Ferromagnet. *Phys. Rev.* **58**, 1098–1113 (1940).